Mathematical methods for magnetic resonance based electric properties tomography

ScuDo
Scuola di Dottorato ~ Doctoral School
WHAT YOU ARE, TAKES YOU FAR

Doctoral Dissertation
Doctoral Program in Electrical, Electronics and Communications Eng. (30^{th}cycle)

Mathematical methods for magnetic resonance based electric properties tomography

By

Alessandro Arduino

******

Supervisor(s):
Prof. Mario Chiampi, Supervisor
Dr. Luca Zilberti, Co-Supervisor

Doctoral Examination Committee:
Prof. Piergiorgio Alotto, Università degli studi di Padova, Italy
Prof. Dr. Markus Bär, Physikalisch-technische Bundesanstalt (PTB), Germany
Dr. Bernd Ittermann, Physikalisch-technische Bundesanstalt (PTB), Germany
Dr. Gianluigi Tiberi, IRCCS Stella Maris Foundation, Italy
Prof. Giuseppe Vecchi, Politecnico di Torino, Italy

Politecnico di Torino
2018

Declaration

I hereby declare that, the contents and organization of this dissertation constitute my own original work and does not compromise in any way the rights of third parties, including those relating to the security of personal data.

Alessandro Arduino
2018

* This dissertation is presented in partial fulfillment of the requirements for **Ph.D. degree** in the Graduate School of Politecnico di Torino (ScuDo).

Acknowledgements

I would like to thank my supervisors, prof. Mario Chiampi (Politecnico di Torino) and dr. Luca Zilberti (INRiM), as well as dr. Oriano Bottauscio (INRiM), who acted as a third supervisor, for their invaluable support during the last three years. Besides introducing me the magnetic resonance imaging research field, they supported me incoparably, since they guided me without depriving me of the freedom necessary to explore and to grow both from the human and the scientific point of view.
I also want to thank dr. Francesca Romana Pennecchi (INRiM), who gave me valuable advices in statistics and introduced me to the GUM, the guide to the expression of uncertainty in measurement.
Furthermore, I need to acknowledge all the collegues of INRiM for welcoming me and providing me a friendly and stimulating environment.

Abstract

Magnetic resonance-based electric properties tomography (MREPT) is a recent quantitative imaging technique that could provide useful additional information to the results of magnetic resonance imaging (MRI) examinations. Precisely, MREPT is a collective name that gathers all the techniques that elaborate the radiofrequency (RF) magnetic field B_1 generated and measured by a MRI scanner in order to map the electric properties inside a human body. The range of uses of MREPT in clinical oncology, patient-specific treatment planning and MRI safety motivates the increasing scientific interest in its development. The main advantage of MREPT with respect to other techniques for electric properties imaging is the knowledge of the input field inside the examined body, which guarantees the possibility of achieving high-resolution. On the other hand, MREPT techniques rely on just the incomplete information that MRI scanners can measure of the RF magnetic field, typically limited to the transmit sensitivity B_1^+.

In this thesis, the state of art is described in detail by analysing the whole bibliography of MREPT, started few years ago but already rich of contents. With reference to the advantages and drawbacks of each technique proposed for MREPT, the particular implementation based on the contrast source inversion method is selected as the most promising approach for MRI safety applications and is denoted by the symbol csiEPT. Motivated by this observation, a substantial part of the thesis is devoted to a thoroughly study of csiEPT. Precisely, a generalised framework based on a functional point of view is proposed for its implementation. In this way, it is possible to adapt csiEPT to various physical situations. In particular, an original formulation, specifically developed to take into account the effects of the conductive shield always employed in RF coils, shows how an accurate modelling of the measurement system leads to more precise estimations of the electric properties. In addition, a preliminary study for the uncertainty assessment of csiEPT, an imperative requirement in order to make the method reliable for *in vivo*

applications, is performed. The uncertainty propagation through csiEPT is studied using the Monte Carlo method as prescribed by the Supplement 1 to GUM (Guide to the expression of Uncertainty in Measurement). The robustness of the method when measurements are performed by multi-channel TEM coils for parallel transmission confirms the eligibility of csiEPT for MRI safety applications.

Contents

Chapter 1

Introduction

In recent years, scientists and clinicians have exhibited a growing interest in quantitative imaging for medical applications because of the possibility of achieving an objective understanding of the physiological state of the examined patient. Most of the medical imaging techniques currently used acquire a qualitative image of the patient, whose contrast is a weight of some parameters of the biological tissues and of the scanning machine but do not bring any readable physical information. As a consequence, the interpretation of the results is subjective and diagnostic imaging can be afflicted by examiner bias. In addition, by weighting unspecified parameters, different machines may lead to images with different contrast for the same patient, making the results achieved by instrumentation of different vendors incomparable. Both the issues are overcome by quantitative imaging. In this case, since the contrast of the image measures a specific physical property, it is possible to objectively identify the physiological state of the tissues, as well as their spatial arrangement. Moreover, the contrast does not depend on the used instrumentation, but just on the investigated body, leading to a twofold advantage. On the one hand, it becomes possible to perform a rigorous metrological study on the uncertainty of the images and to compare results from different instrumentation. On the other hand, it allows the detection of imaging markers for some pathologies that do not change across sites, scanners, and even vendors [1, 2].

Recently, quantitative imaging has started to be used in clinical practice, as for the case of magnetic resonance elastography. Based on the same equipment as magnetic resonance imaging (MRI), this technique produces images whose contrast is pixel-

by-pixel proportional to the mechanical properties of the examined body—precisely, to the, possibly complex, elastic shear modulus [3, 4]. Mechanical properties have been considered across the centuries in a qualitative manner for the detection of many pathologies by distinguishing between soft and hard tissues through touch—clinical palpation. Nowadays, magnetic resonance elastography has proven its clinical usefulness in recognising early stage liver diseases, which present an increase in the degree of fibrosis and so in stiffness, in a less invasive and more objective way than palpation [3]. In addition, magnetic resonance elastography allows to study the mechanical properties of regions where palpation is physically impossible, as in deep tissues or in the brain [4]. In order to estimate the elastic shear modulus, first, a peculiar sequence of magnetic fields generated by a MRI scanner produces a map of the displacement induced by a vibrating support at a known frequency, and then the resulting displacement map is used as input for an inverse problem within the linear isotropic viscoelastic materials theory.

In addition, a quantitative imaging technique under development, called magnetic resonance fingerprinting, has been identified as a promising new approach by the European Society of Radiology [5]. Magnetic resonance fingerprinting aims at the simultaneous recovery of the many parameters involved in the MRI working principles—the spin-lattice relaxation time T_1, the spin-spin relaxation time T_2, the proton density, and so on—by elaborating pseudorandomised and undersampled MRI acquisitions with concepts from compressed sensing and pattern recognition [6]. The overall time required by the parameters estimation is comparable to a traditional MRI scan and, despite the physical properties mapped by this technique do not have a direct intuitive application as in the case of magnetic resonance elastography, they are metrologically more reliable than the usual qualitative MRI results as well as less sensitive to noise, patient motion, and other errors due to system imperfections [6]. Moreover, the investigation for complex biomarkers where a multi-parametric analysis is required can be introduced, thanks to the simultaneous estimation of many different properties.

In this dissertation, the quantitative imaging of the electric properties, both the relative permittivity ε_r and the electric conductivity σ, is investigated. This subject has been studied in biomedical research for many years because of its many applications, amongst which the most relevant are probably the ones related to breast cancer detection. Indeed, it has been shown that breast cancer may have a substantially higher electric conductivity than the corresponding healthy tissue [7–10], because

of the lower membrane potentials in cells that have an increased mitotic rate and the consequent higher attraction of positive ions, which are displaced and rotated by radiofrequency (RF) fields [7]. An investigation on the correlation between the electric conductivity and some clinicopathological factors suggests that *in vivo* images of the electric conductivity would help in predicting prognoses in breast cancer, especially for the mitotic state of the tumour cells, that is strongly correlated to poor prognosis, but usually underestimated in core biopsies [10]. Some considerations in this direction have been performed also on *exciso* malignant colorectal tissues [11]. Moreover, nowadays there exist many different medical therapies using electromagnetic fields that would benefit—for both efficacy and safety—from the patient-specific planning and dosimetry made possible by the estimation of the actual distribution of the electric properties. Just some examples of these therapies are:

Oncological hyperthermia. The beneficial effect of heating cancerous tissues has been known for thousands of years [12]. In the last years of the 19^{th} century, because of the observation of natural regression of tumours in patients with high fever, the possibility to inoculate bacterial toxins in order to induce the fever was taken into account as a medical treatment [13]. For the same reason as well as for the capability of moderately high temperature—around 39 °C to 45 °C—to increase the sensitivity of cells to radio and chemotherapy, hyperthermia is currently used as a therapy [12, 14, 15]. In order to increase the temperature until the optimal thermal dose is reached in the tumour without heating the healthy tissues, the Joule effect can be exploited by applying properly designed electromagnetic fields [12]. In the emerging case of nanoparticle mediated hyperthermia, magnetic nanoparticles are inoculated in the patient and targeted to the cancerous tissue, then the application of an alternating magnetic field generates heat in the nanomagnets by hysteresis loss or Néel relaxation loss [16]. Anyway, this technology still requires extensive studies about the long-term safety and sustainability of nanoparticles, for example in regard to bioaccumulation due to limited excretion [17].

Electroporation. When cells are exposed to sufficiently intense electric fields, they develop pores in the cell membrane that, if enough large and stable, increase rapidly and considerably their permeability along with their electric conductivity. Based on this phenomenon, called electroporation, many biotechnological [18] and medical [19] applications have been developed, such as elec-

trochemotherapy, non-thermal ablation (irreversible electroporation), and gene therapy, which expose the object of interest to time-varying pulsed electric fields—with an harmonic content up to some hundreds of kilohertz. In order to expose a selected tissue to a spatially homogeneous electric field with no interferences with the healthy tissues, a system of antennas must be carefully designed with the help of numerical simulations [20].

Pulsed electromagnetic fields. The exposure to time-varying pulsed electric fields with low energy can be of benefit in medicine, because it induces a substantial upregulation of some adenosine membrane receptors in human cells, and so increases their anti-inflammatory effect [21]. This kind of field could be useful both *in vitro*, for tissue engineering [21], and *in vivo*, for surgical implants treatment [21], bone and joint inflammatory disorders [22], and brain tumour treatment [23]. Also in this case, accurate dosimetry requires accurate numerical modelling of the system [24].

Transcranial magnetic stimulation. The possibility to inspect the integrity of the motor cortex of a patient by magnetically inducing a low frequency current in it has led to the introduction of transcranial magnetic stimulation as a diagnostic tool [25]. Subsequently, it has been discovered that application of a repetitive transcranial magnetic stimulation can be used therapeutically to treat many neurological and psychiatric disorders, like chronic pain, epilepsy, depression, and schizophrenia [26]. Dosimetrical studies on the actual induced currents require the adoption of numerical simulations [27].

Since, despite they are often referred to as dielectric constants, the electric properties of biological tissues are dispersive, *i.e.* they are strongly influenced by the frequency of the considered electromagnetic field [28–30], different imaging techniques have to be developed, each one effective in a particular frequency range. The dispersive behaviour of these parameters can be understood by investigating the time-varying microscopic—molecular and cellular—mechanisms averaged in the macroscopic electric properties definition. Precisely, biological tissues are mostly composed of electrolytes and proteins dissolved in intra- and extra-cellular water, which interact with cell membranes and react to the electromagnetic fields by displacing and polarizing themselves according to different relaxation times [7, 28–30].

At low frequencies—up to a few kilohertz—a main strategy for electric conductivity imaging is the electric impedance tomography (EIT) [31]. Assuming the validity of the quasi-stationary conduction approximation, the scalar electric potential inside an inspected body Ω, denoted by $\phi \in H^1(\Omega)$, can be modelled as the unique solution of the problem

$$\begin{cases} \nabla \cdot (\sigma \nabla \phi) = 0\,, \text{ in } \Omega \\ \phi = f\,, \text{ on } \partial\Omega \end{cases}$$

where $f \in H^{1/2}(\partial\Omega)$ is the known potential at the boundary. Here, the symbol $H^{\alpha}(A)$ denotes the Sobolev space of order α whose elements are defined in the domain A. In this context, the Dirichlet-to-Neumann map Λ_σ, parameterised by the electric conductivity distribution σ, is defined as the linear operator between fractional order Sobolev spaces [32] that assigns a current flowing out from the body to each voltage on the boundary,

$$\begin{array}{rccc} \Lambda_\sigma \;:\; H^{1/2}(\partial\Omega) & \longrightarrow & H^{-1/2}(\partial\Omega) \\ f & \longmapsto & \sigma\dfrac{\partial\phi}{\partial n}\,, \end{array}$$

with n the outward unit normal to $\partial\Omega$. Thus, EIT can be stated as the problem of finding the essentially bounded non-negative electric conductivity distribution $\sigma \in L^{\infty}(\overline{\Omega})$, being $\overline{\Omega} = \Omega \cup \partial\Omega$ the closure of Ω, given the Dirichlet-to-Neumann map Λ_σ [31, 33]. Usually, the voltage at the boundary is measured, by virtue of energetic considerations, when a certain known current is injected in the body by electrodes applied on the skin, leading in practice to the approximate knowledge of the Neumann-to-Dirichlet map Λ_σ^{-1} [31]. Current injection in the body is a delicate procedure, which can be painful and even burn the patient if the design of the electrodes is not optimised [34, 35]. Because of its unusual as well as elegant mathematical formulation, EIT is actively studied, other than physicists and engineers, by mathematicians, which often refers to it as *Calderón's problem* [33], because of Calderón's pioneering contribution in EIT formalisation [36]. Despite the efforts made from many sides by the scientific community on EIT development, the images obtained by this method are inherently affected by low resolution, especially in regions far from the electrodes—as in case of deep organs when the electrodes are applied on the skin of the patient—, making it unfeasible in biomedical applications that require high resolution imaging [31, 35, 37].

In order to achieve high resolution images of the electric conductivity at low frequency, the knowledge of some quantity internal to Ω in addition to the boundary measurements would help. This is made possible by the MRI scanners, which are able to measure the map of the longitudinal component H_z—the one directed as the MRI static field $\boldsymbol{B}_0$—of magnetic fields induced in the body by externally injected currents [38] (cf. Appendix A). Consequently, by rotating the patient inside the scanner in three different positions, it would be possible to measure the whole induced magnetic field $\boldsymbol{H}$ and deduce the induced current density by means of Ampère's law $\boldsymbol{J} = \nabla \times \boldsymbol{H}$ [38]. This imaging procedure is known as magnetic resonance current density imaging (MRCDI) and led to the proposal of different magnetic resonance-based electric impedance tomography (MREIT) techniques, which take advantage in different ways of Ohm's law $|\boldsymbol{J}| = \sigma|\nabla\phi|$ to invert the conduction problem [35, 37]. In many biomedical applications, however, it would be preferable to avoid rotating the patient inside the MRI scanner, because of the technical difficulties in avoiding pixel misalignments during MRCDI and the risk of changing the geometric arrangement of the internal organs during the rotation, in addition to the physical constraint imposed by many MRI bores. The harmonic B_z algorithm overcomes this issue by implementing MREIT based on the measurement of H_z only [39]. It is based on the elementary observation that

$$-\nabla^2\boldsymbol{H} = \nabla \times \boldsymbol{J} = \nabla\phi \times \nabla\sigma\,.$$

The z-component of this vector relation implicitly defines the dependency of the electric conductivity on the measured induced magnetic field component and the electric potential. It is possible to take advantage of this implicit relation to invert the conduction problem when two linearly independent currents are considered [35, 37, 39]. In order to avoid the external current injection in the patient, the feasibility of MREIT from measurements of the eddy currents induced by the MRI gradient coils in the body has been considered [40–42]. Unfortunately, for the existing MRI sequences the noise in the measurement of the induced field is much higher than its intensity, making MREIT from gradient coils unfeasible at the moment [41, 42].

At frequencies in the RF range—from hundreds of kilohertz up to hundreds of gigahertz—the approach for the imaging of electric properties is strongly different from the one at low frequency. Usually there is no injection of current in the body, which is, instead, irradiated—or illuminated—by a RF electromagnetic field gen-

erated by a well known source arranged around it. The body distorts the incident electromagnetic field because of the scattering field generated by the eddy currents induced inside the body depending on its electric properties. Thus, it is possible to invert Maxwell's equations to obtain images of the electric properties distributions starting from measurements of the deformation of the electromagnetic field induced by the body [43]. The measurements can be performed by a set of receiver antennas located outside the body. It is worth noting that the described procedure applies to any inverse scattering problem, giving rise to a unified theory for both acoustic and electromagnetic inverse scattering [43]. In biomedical applications, the inverse electromagnetic scattering problem is often referred to as microwave tomography. Despite the many results that have been achieved on this subject [44–46], especially after the introduction of the contrast source inversion (CSI) technique [47–50], microwave tomography suffers of some theoretical limitations since it is an ill-posed problem in the sense of Hadamard [51]. Precisely, it suffers of a non continuous dependence of the electric properties on the input data, which is reflected in the existence of a maximum achievable resolution in the output images [51]. Moreover, the inverse problem is usually mathematically formalised as the minimisation problem of a certain cost functional, which may be non-convex and may have, other than the global minimum, additional local minima that play the role of false solutions for the deterministic minimisation algorithms [52].

In the same way as introducing measurements performed by MRI scanners considerably increases the resolution of EIT leading to a whole new technique, the same happens at RF, since microwave tomography would benefit from field measurements inside the inspected body for both resolution increase and local minima removal [51, 52]. At the involved frequency, MRCDI is no more feasible, and techniques able to measure the RF magnetic field $\boldsymbol{B}_1$ produced by the MRI scanner are considered (cf. Appendix A). The techniques that aims at recovering images of the electric properties at RF employing MRI measurements are called magnetic resonance-based electric properties tomography (MREPT) or just electric properties tomography (EPT). The magnitude of the active part—the component rotating in the same wise as the nuclear spin precession—of $\boldsymbol{B}_1$, denoted as B_1^+, is measured by many different methods [53–57], most of which developed to check $|B_1^+|$ homogeneity, useful in order to assess the MRI scanner quality (cf. Appendix A). With the beginning of systematic research on MREPT in 2009 [58, 59], the estimation

of the phase of B_1^+ by MRI measurements has become object of study [60, 61]. In this thesis, MREPT is investigated according to the following structure:

- Chapter 2 contains a comparative review of the main techniques proposed for MREPT implementation and a discussion of their advantages and drawbacks.
- Chapter 3 deepens a particular MREPT method based on the contrast source inversion technique, which has very promising properties, especially for MRI safety applications.
- Chapter 4 draws some conclusions about the results collected in this thesis and delineates the future research trends on MREPT.

In addition, supplemental materials that introduce basic concepts can be found in the appendices:

- Appendix A describes how MRI works and proposes the post-processing of the achieved images with a couple of examples.
- Appendix B collects some useful results of functional analysis and suggests a technique to compute the first and second order derivatives of a phase—helpful in the MREPT methods based only on the B_1^+ phase.

Chapter 2

Review of methods for the electric properties tomography

The possibility to non-invasively recover the distribution of the electric properties of a human body from the results of a MRI examination was first proposed in 1991 by Haacke and colleagues in [62]. In that work, a particular MRI sequence (cf. Appendix A), a gradient echo sequence with low flip angle, is employed in order to acquire images proportional to the magnitude of the RF field $\boldsymbol{B}_1$, which has to be interpreted in the time-harmonic domain with an omitted factor $e^{i\omega t}$, being ω the Larmor angular frequency, as all the fields appearing in this chapter. Relying on this information, the electric properties are laboriously recovered by an iterative procedure starting from an initial guess. In the same paper, an explicit formula that relates the electric properties to the RF field is proposed for homogeneous regions leading to a straightforward method to evaluate both the permittivity and the conductivity. Anyway, as stated by the authors [62], "*[...] this method is not pursued further at this time [...]*" because "*[...] MR images contain spurious phase effects unrelated to the RF penetration which makes a simple extraction difficult.*"

The matter has not been advanced any further until, in 2003, Wen presented at a conference some experimental non-invasive quantitative mapping of the electric properties using the wave propagation effects of the RF field [63], more than ten years after the work of Haacke and colleagues. To achieve the results, Wen used the explicit formula already suggested in [62]. The application of this method was made possible by the improvement of the magnetic resonance (MR) systems with

respect to the past [64] and by the introduction of high field MRI scanners, which allows to increase both the spatial resolution of the images and the accuracy of the measurements [63]. It is worth noting that Wen did not cite Haacke's article, suggesting that he developed the same technique for retrieving the electric properties independently.

In the following years, the relation between the electric conductivity and the non-resonant thermal noise measured by RF probes located around the examined body has been exploited in the noise tomography technique [65–67]. Furthermore, in 2006 a new strategy to non-invasively map the electric properties relying on the distribution of the induced RF field $\boldsymbol{B}_1$ has been described and named electric properties tomography (EPT) by Katscher and colleagues [68, 69]. Also in this case, the authors do not cite neither Haacke's nor Wen's papers, suggesting the discovery for the third time of the same concept. Differently from Wen [63], the electric properties are recovered by a complicated iterative procedure instead of the simple explicit formula. In [68, 69] it is stated that EPT is a preferable technique than both microwave and noise tomography because it does not require any probe in addition to the usual MRI equipment and because it can reach higher resolution, not being based on an ill-posed inverse problem. Actually, despite EPT can really achieve images with higher quality than other methods, the last sentence is not true—since by its own definition, EPT is an inverse problem and also the apparently most direct method to solve it, as for example the explicit relation of Wen [63], faces this fact. In particular, derivation is a typical ill-posed inverse problem (cf. Appendix B) and both Wen's and Katscher's approaches require the computation of spatial derivatives of the measured $\boldsymbol{B}_1$. The advantage of EPT with respect to other methods is rather that it relies on a big amount of information which is measured, although non-invasively, inside the examined body and not just on its periphery.

Finally, in 2009 the systematic study of EPT started [58, 59]. Up to now, a plethora of different techniques have been proposed for implementing EPT—or, as it is more often named, magnetic resonance-based electric properties tomography (MREPT)—[61, 70–78] and, allegedly, many others will be suggested in coming years. In order to classify the methods, it is convenient to introduce a MREPT taxonomy organised by a couple of categories:

Spatial categories It is possible to distinguish between *local* and *global* methods. The local methods try to recover the electric properties in a point of the body by

elaborating the electromagnetic information measured just in a neighbourhood of the point itself. On the other hand, the global methods consider all the obtained information at once to estimate the whole distribution of the electric properties.

Mathematical categories The methods can be classified as *direct* or *inverse*. The direct methods relegate the inverse nature of MREPT to some preliminary computations—usually the estimation of the spatial derivatives of $\boldsymbol{B}_1$—, while the remaining part follows a direct approach. On the other side, the inverse methods treat the whole MREPT as an inverse problem.

Up to now, the mathematical categories only make sense for global methods, because all local methods are direct.

In this chapter, the main strategies proposed in literature to implement MREPT are mentioned and reviewed.

2.1 Standard EPT

The method described in this section appeared for the first time in the pioneering paper of Haacke and colleagues [62], although there it was not applied to experimental data because of the difficulty in retrieving the needed information. The technique, in the following denoted by the symbol stdEPT, is the most studied and developed MREPT implementation [63, 58, 70, 79, 80] and one of the first applied to experimental measurements [63].

2.1.1 Derivation

For an isotropic and magnetically neutral medium—*i.e.*, whose magnetic permeability is the one of vacuum μ_0, as is a reasonable assumption for biological tissues [81]—Maxwell's equations in time-harmonic domain can be easily combined to obtain the partial differential equation for the magnetic field $\boldsymbol{H} = \boldsymbol{B}/\mu_0$

$$\nabla \times \left(\tilde{\varepsilon}^{-1} \nabla \times \boldsymbol{H}\right) = \omega^2 \mu_0 \boldsymbol{H}\,, \tag{2.1}$$

where $\tilde{\varepsilon} = \varepsilon - \mathrm{i}\sigma/\omega$ is the complex permittivity, ε is the electric permittivity and σ is the electric conductivity. In a homogeneous region, *i.e.* in points where the gradient of the complex permittivity is null—or at least negligible—, this relation can be elaborated by virtue of Gauss's law for magnetism $\nabla \cdot \boldsymbol{B} = \mu_0 \nabla \cdot \boldsymbol{H} = 0$, leading to the vector Helmholtz equation

$$-\nabla^2 \boldsymbol{H} = \kappa^2 \boldsymbol{H}\,, \tag{2.2}$$

where $\kappa^2 = \omega^2 \mu_0 \tilde{\varepsilon}$ is the square of the propagation coefficient of the radiation. The latter vector equation can be specialised for any Cartesian component α of the magnetic field H_α in

$$-\nabla^2 H_\alpha = \kappa^2 H_\alpha\,. \tag{2.3}$$

In particular, the components in the transverse plane $\hat{\boldsymbol{x}} \otimes \hat{\boldsymbol{y}}$ (cf. Appendix A) can be linearly combined to obtain the positively rotating component of the field H^+ (cf. lemma A.2). Under the assumption that the transmit sensitivity $B_1^+ = \mu_0 H^+$ has been measured in a set of points—or voxels—and that its second order derivatives have been estimated in the same points, the complex permittivity can be recovered voxel by voxel as

$$\tilde{\varepsilon} = -\frac{\nabla^2 H^+}{\omega^2 \mu_0 H^+}\,. \tag{2.4}$$

The real and the imaginary parts of (2.4) contain the information of the electric permittivity and conductivity, respectively. Precisely, the relation can be made explicit for the two properties

$$\varepsilon = -\mathrm{Re}\left(\frac{\nabla^2 H^+}{\omega^2 \mu_0 H^+}\right), \qquad \sigma = \mathrm{Im}\left(\frac{\nabla^2 H^+}{\omega \mu_0 H^+}\right). \tag{2.5}$$

Clearly, stdEPT is a local direct method.

A slightly different version of the local relation (2.4) has been obtained in [58, 70], where Maxwell equations are elaborated in integral form. Precisely, Faraday's law applied to a generic fixed surface Σ centred in $\boldsymbol{x}$ leads to

$$\oint_{\partial\Sigma} \boldsymbol{E} \cdot \boldsymbol{\tau}\, \mathrm{d}\ell = -\mathrm{i}\omega\mu_0 \int_\Sigma \boldsymbol{H} \cdot \boldsymbol{n}\, \mathrm{d}S\,, \tag{2.6}$$

where $\boldsymbol{E}$ is the electric field, $\boldsymbol{\tau}$ is the unit vector tangent to the border $\partial\Sigma$ and $\boldsymbol{n}$ is the unit vector orthogonal to Σ. Similarly, the circulation of Ampère's law around $\partial\Sigma$

reads

$$\oint_{\partial\Sigma} \nabla \times \boldsymbol{H} \cdot \boldsymbol{\tau}\, \mathrm{d}\ell = \mathrm{i}\omega \oint_{\partial\Sigma} \tilde{\varepsilon} \boldsymbol{E} \cdot \boldsymbol{\tau}\, \mathrm{d}\ell\,. \tag{2.7}$$

Taking the ratio between (2.6) and (2.7) leads to

$$\frac{\oint_{\partial\Sigma} \nabla \times \boldsymbol{H} \cdot \boldsymbol{\tau}\, \mathrm{d}\ell}{\omega^2 \mu_0 \int_{\Sigma} \boldsymbol{H} \cdot \boldsymbol{n}\, \mathrm{d}S} = \frac{\oint_{\partial\Sigma} \tilde{\varepsilon} \boldsymbol{E} \cdot \boldsymbol{\tau}\, \mathrm{d}\ell}{\oint_{\partial\Sigma} \boldsymbol{E} \cdot \boldsymbol{\tau}\, \mathrm{d}\ell} \simeq \tilde{\varepsilon}(\boldsymbol{x})\,, \tag{2.8}$$

where the last approximation is valid if in $\partial\Sigma$ the spatial variation of $\tilde{\varepsilon}$ is negligible with respect to the variation of the tangential component of the electric field.

Relation (2.8) involves all the components of the magnetic field, but their role depends on the choice of the surface Σ. However, except than in particular situations in which only the positively rotating component of the magnetic field H^+ is non-negligible, like for the RF field generated by a birdcage coil with quadrature feed [58], quantities that cannot be measured appear in (2.8). This issue has been overcome in [70], where (2.8) is further developed by some complicated mathematical manipulation which involves a rotating surface Σ. The same result achieved in [70] can be much more easily and directly obtained by integrating equation (2.3) over a small region V centred in $\boldsymbol{x}$. If the complex permittivity is constant or with negligible variations in V, then the resulting equation can be written as

$$\tilde{\varepsilon}(\boldsymbol{x}) \simeq -\frac{\int_V \nabla^2 H^+\, \mathrm{d}V}{\omega^2 \mu_0 \int_V H^+\, \mathrm{d}V} = -\frac{\oint_{\partial V} \nabla H^+ \cdot \boldsymbol{n}\, \mathrm{d}S}{\omega^2 \mu_0 \int_V H^+\, \mathrm{d}V}\,, \tag{2.9}$$

being ∂V the surface enclosing V and $\boldsymbol{n}$ the outward unit vector orthogonal to ∂V.

Since stdEPT, in both its local (2.5) and integral (2.9) formulations, relies on the hypothesis of local homogeneity of the electric properties, it presents a systematic error at the interfaces between different materials, as can be appreciated in Fig. 2.1. As a consequence, the presence of many interfaces between tissues with different electric properties in the human body—for example, let's think about the convolutions of the brain—makes the method strongly limited in clinical applications. The systematic error is deeply discussed in [79]. In order to avoid the assumption of local homogeneity and thus the systematic error, equation (2.1) can be elaborated

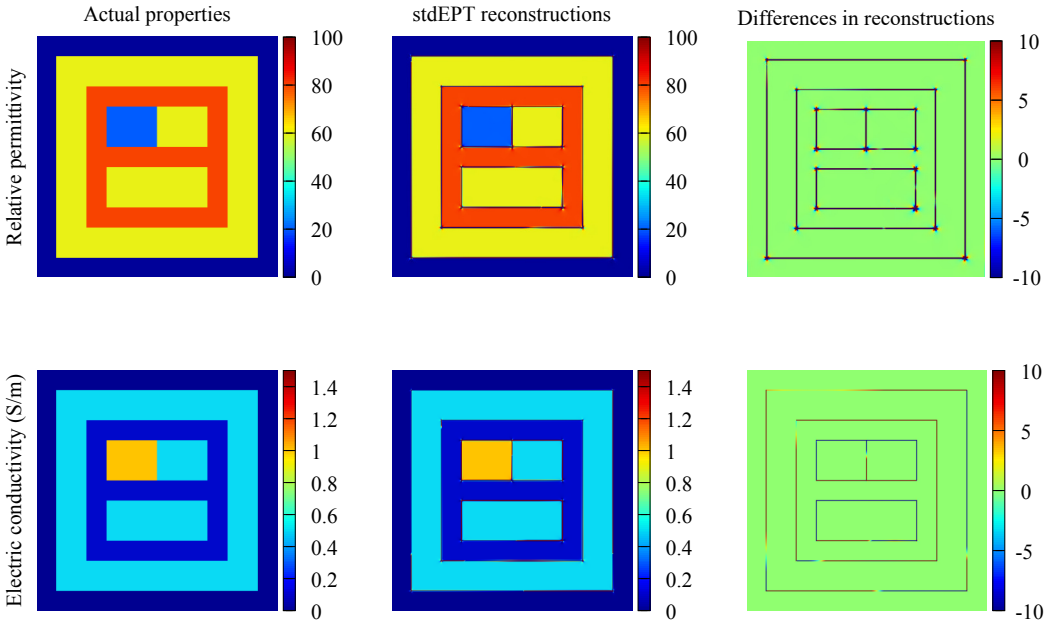

Fig. 2.1 The systematic error in stdEPT is highlighted by the application of the method to a simple two-dimensional problem. A cylinder of indefinite height, whose transverse section is a square with sides of 10 cm presenting three different values of relative permittivity and conductivity, is radiated by a plane wave at 128 MHz. The active part of the magnetic field H^+ has been computed numerically on a very fine discretisation of the domain (with a resolution of 0.2 mm) in order to make the numerical errors negligible. The errors in the reconstructions, pictured as signed differences for both the properties, are located at the interfaces between tissues.

differently by exploiting the Leibniz's product rule on the left hand side to obtain

$$\nabla\left(\tilde{\varepsilon}^{-1}\right)\times\nabla\times\boldsymbol{H}-\tilde{\varepsilon}^{-1}\nabla^2\boldsymbol{H}=\omega^2\mu_0\boldsymbol{H}\,, \tag{2.10}$$

where the Gauss's law for magnetism has been used. By multiplying both sides of the latter equation by $\nabla\times\boldsymbol{H}$, it results that [82]

$$\tilde{\varepsilon}=-\frac{\nabla^2\boldsymbol{H}\cdot\nabla\times\boldsymbol{H}}{\omega^2\mu_0\boldsymbol{H}\cdot\nabla\times\boldsymbol{H}}\,. \tag{2.11}$$

Although equation (2.11) is achieved with no approximations, it cannot be used in practice because it requires the knowledge of all the three components of the magnetic field and because it fails when $\boldsymbol{H}\cdot\nabla\times\boldsymbol{H}=0$.

It is interesting that stdEPT, being based on the extremely simple algebraic relation (2.4), can be easily manipulated and deeply analysed. In particular, by distinguishing the magnitude $|H^+|$ and the phase φ^+ of $H^+ = |H^+|e^{i\varphi^+}$, the Laplacian can be computed explicitly and equations (2.5) become

$$\varepsilon = -\frac{\nabla^2|H^+|}{\omega^2\mu_0|H^+|} + \frac{|\nabla\varphi^+|^2}{\omega^2\mu_0}, \tag{2.12}$$

and

$$\sigma = \frac{\nabla^2\varphi^+}{\omega\mu_0} + 2\frac{\nabla|H^+|\cdot\nabla\varphi^+}{\omega\mu_0|H^+|}. \tag{2.13}$$

Thus, under the hypothesis that $|\nabla^2|H^+||/|H^+| \gg |\nabla\varphi^+|^2$, the permittivity can be recovered by the approximate relation

$$\varepsilon \simeq -\frac{\nabla^2|H^+|}{\omega^2\mu_0|H^+|}, \tag{2.14}$$

which is referred to as magnitude-based stdEPT [70]. It is worth noting that, involving only non-negative terms, the error in (2.14) is always non-negative, and so the magnitude-based stdEPT systematically underestimates the permittivity. Similarly, the hypothesis that $|\nabla^2\varphi^+| \gg 2|\nabla|H^+|\cdot\nabla\varphi^+|/|H^+|$ leads to the phase-based stdEPT for the recovery of the electric conductivity [70]

$$\sigma \simeq \frac{\nabla^2\varphi^+}{\omega\mu_0}. \tag{2.15}$$

Both relations (2.14) and (2.15) introduce an additional systematic error, which can be easily deduced by comparison with (2.12) and (2.13).

The hypothesis underlying (2.15) is often fulfilled by the RF magnetic field generated by the transmit coils, which are usually designed to provide an almost homogeneous flip angle in the imaged volume. By this way, images of the proton density with a minimal influence of the transmit sensitivity would be achieved (cf. Appendix A). In general, the homogeneity of the transmit sensitivity depends on the static field intensity, on the geometry of the RF coil and so on. The additional systematic error is depicted in Fig. 2.2, where the electric properties of an indefinite cylinder have been recovered from the magnetic field H^+ generated by a birdcage coil. In [70] it is reported that phase-based stdEPT introduces a larger error when $\omega\varepsilon \gg \sigma$, situation that for biological tissues occurs only at very high Larmor

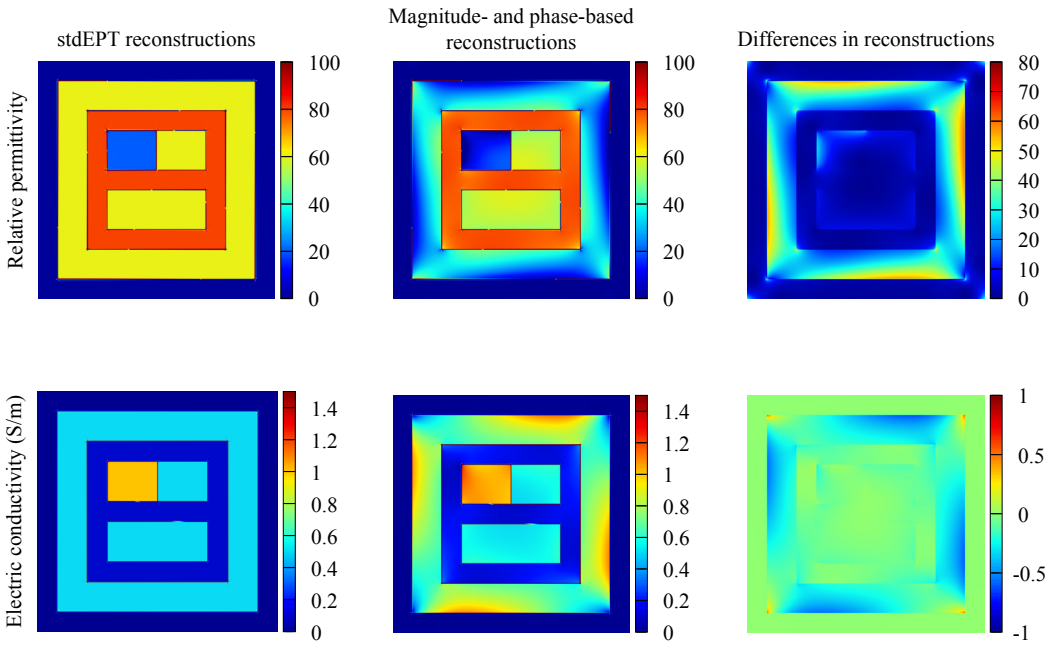

Fig. 2.2 The error introduced approximating (2.12) and (2.13) by respectively (2.14) and (2.15) is reported. The same cylinder described in Fig. 2.1 is radiated by the electromagnetic field generated by a birdcage coil with 16 legs at 128 MHz. The birdcage coil has been simulated as 16 line sources distributed uniformly on a circle of 10 cm radius, each one driven by a phase-shifted unitary current. The active part of the magnetic field $H^+ = |H^+|e^{i\varphi^+}$ has been computed numerically on a very fine discretisation of the domain (with a resolution of 0.2 mm) in order to make the numerical errors negligible. The signed differences in the reconstructions coincide with $|\nabla\varphi^+|^2/(\omega^2\mu_0\varepsilon_0)$ and $2\nabla|H^+|\cdot\nabla\varphi^+/(\omega\mu_0|H^+|)$, respectively, as can be deduced by (2.12) and (2.13).

frequencies, above 128 MHz [83]. For this reason, phase-based stdEPT (2.15) has been deeply developed [60, 83, 84] and extensively applied in many experimental contexts [9, 10, 85, 86] leading to satisfactory results. Since its hypothesis is less frequently fulfilled, magnitude-based stdEPT does not share the same fate of phase-based stdEPT.

2.1.2 Implementation

Despite its simplicity, stdEPT faces some implementation issues which characterise the MREPT problem. The one which weakens the technique the most is the measurement of the transmit sensitivity $B_1^+ = \mu_0|H^+|e^{i\varphi^+}$ using the MRI scanner. Many B_1-mapping techniques have been proposed to measure the magnitude $\mu_0|H^+|$ of the

transmit sensitivity [53–57], but only the so-called transceive phase $\varphi^{\pm} = \varphi^{+} - \tilde{\varphi}^{-}$, namely the difference of the phases of the transmit and the receive sensitivities, can be deduced from the MRI images (cf. Appendix A). The receive sensitivity is denoted by $\tilde{B}^{-} = \mu_0 \tilde{H}^{-} = \mu_0 |\tilde{H}^{-}| \mathrm{e}^{\mathrm{i}\tilde{\varphi}^{-}}$. When particular transmit and receive coils are employed in the MRI examination, as for example the same birdcage coil in quadrature feed with polarisation switching between transmission and reception [58, 64], half of the transceive phase can be used as a good approximation of the transmit sensitivity phase (cf. Appendix A)

$$\varphi^{+} \simeq \frac{\varphi^{\pm}}{2}. \tag{2.16}$$

The use of the latter relation is referred to as transceive phase assumption [64]. In case of birdcage coils with polarisation switching, the transceive phase assumption holds for Larmor frequencies up to 128 MHz [64], as can be appreciated in Fig. 2.3.

It is worth noting that the electric properties can be recovered from the receive sensitivity following the same derivation presented for the transmit sensitivity,

$$\tilde{\varepsilon} = -\frac{\nabla^2 (\tilde{H}^{-})^{*}}{\omega^2 \mu_0 (\tilde{H}^{-})^{*}}, \tag{2.17}$$

where the asterisk denotes the complex conjugation. Thus, as in (2.13),

$$\sigma = -\frac{\nabla^2 \tilde{\varphi}^{-}}{\omega \mu_0} - 2\frac{\nabla |\tilde{H}^{-}| \cdot \nabla \tilde{\varphi}^{-}}{\omega \mu_0 |\tilde{H}^{-}|}. \tag{2.18}$$

If it is true that $|\nabla^2 \tilde{\varphi}^{-}| \gg 2|\nabla |\tilde{H}^{-}| \cdot \nabla \tilde{\varphi}^{-}|/|\tilde{H}^{-}|$, then

$$\sigma \simeq -\frac{\nabla^2 \tilde{\varphi}^{-}}{\omega \mu_0}. \tag{2.19}$$

Thanks to the linearity of the Laplacian, the arithmetic mean of (2.15) and the latter relation reads

$$\sigma \simeq \frac{\nabla^2 \varphi^{\pm}}{2\omega \mu_0}. \tag{2.20}$$

This means that the transceive phase assumption can be used in phase-based stdEPT independently of the considered Larmor frequency, provided that the hypotheses behind (2.15) and (2.19) hold. In order to minimise $|\nabla |\tilde{H}^{-}||$, the technology of B_1^{+}-shimming has been employed to optimally combine the signals measured by multiple receiver coils [84], which are commonly used in clinical scanners for parallel

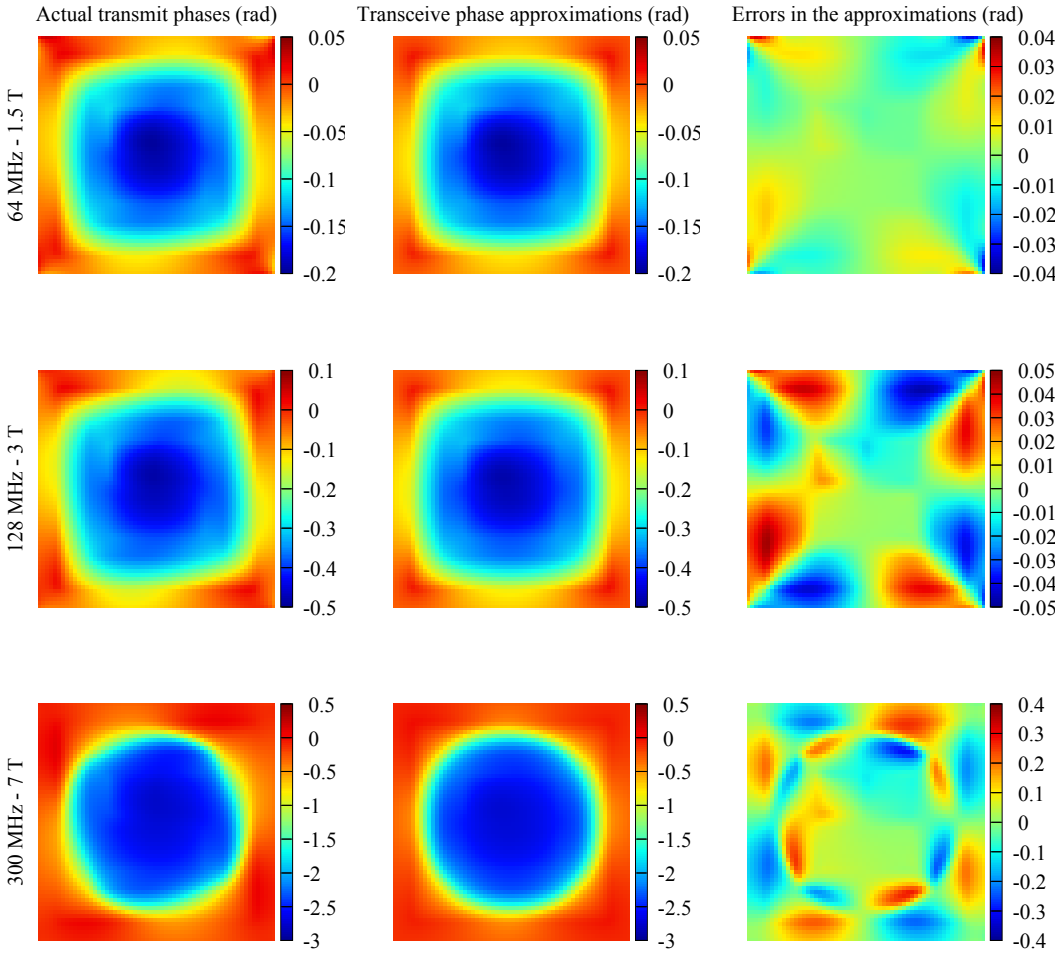

Fig. 2.3 The difference between the transmit phase and half the transceive phase induced by a birdcage with 16 legs in quadrature alimentation with polarisation switching in presence of the cylinder described in Fig. 2.1 is reported. Three Larmor frequencies corresponding to common static fields for MRI are considered. The error introduced by the transceive phase assumption growths together with the static field intensity.

imaging [87]. The possibility to employ (2.17) on the single acquisition of multiple receiver coils is investigated in [88].

Besides measurement issues, the estimation of the Laplacian of the measured, hence noisy, quantities is a critical task that stdEPT shares with all the direct methods. Computation of spatial derivatives is an ill-posed problem (cf. Appendix B) and, as such, it must be performed appropriately in order to handle noisy input. The easiest way to deal with the noise in the measurements is to apply to the map a smooth mollifier f, as for example a Gaussian filter [72, 79, 89], and approximate the derivatives by traditional finite difference schemes. Thus, equation (2.4) becomes

$$\tilde{\varepsilon} = -\frac{\nabla^2 (f * H^+)}{\omega^2 \mu_0 (f * H^+)}, \tag{2.21}$$

where $*$ denotes the convolution product. The adoption of non-linear filters has been proposed in order to preserve the spatial details of the imaged sample [90]. Alternatively, a robust kernel can be adopted for the numerical differentiation, so that both filtering and derivative estimation are performed at the same time [58, 60, 61, 70, 75, 88]. A common robust differentiation technique is the Savitzky–Golay filter [91, 92], named after the analytical chemist Abraham Savitzky and the mathematician Marcel Golay who first published a table of convolution coefficients for one-dimensional problems [91].

In the three-dimensional case, the Savitzky–Golay filter can be generalised as follows. Let's denote with u the generic complex map that has to be filtered. In each point $\boldsymbol{x}_0$, the map u is approximated by the best fitting element from the set $\mathbb{Q}_{\boldsymbol{r}}$ of polynomials with complex coefficients of degree equal or less than r_i with respect to the i-th variable for $i = 1,2,3$, being $\boldsymbol{r} \in \mathbb{N}^3$,

$$\mathbb{Q}_{\boldsymbol{r}} = \left\{ q(\boldsymbol{x}) = \sum_{i=0}^{r_1} \sum_{j=0}^{r_2} \sum_{k=0}^{r_3} a_{ijk} x^i y^j z^k, \quad a_{ijk} \in \mathbb{C} \right\}. \tag{2.22}$$

Precisely, the polynomial $q \in \mathbb{Q}_{\boldsymbol{r}}$ is chosen such that

$$q(\boldsymbol{x}) = u(\boldsymbol{x}_0 + \boldsymbol{x}), \quad \text{for } \boldsymbol{x} \to \boldsymbol{0}, \tag{2.23}$$

and the derivatives of u in $\boldsymbol{x}_0$ are approximated by the derivatives of q in $\boldsymbol{0}$. Since the map u is measured on a finite number of points, in order to choose the polynomial q

only a set of points $\boldsymbol{x}_m$ around the central point $\boldsymbol{x}_0$ is considered, for $m = 1, \ldots, M$. The equations

$$q(\boldsymbol{x}_m - \boldsymbol{x}_0) = u(\boldsymbol{x}_m), \quad m = 1, \ldots, M, \tag{2.24}$$

are collected in a linear system whose unknowns are the coefficients a_{ijk}. In order to suppress the noise from the map u, the linear system should include more equations than unknowns and the coefficients should be chosen as those which minimise the quadratic error. If the map u is measured on a uniform Cartesian grid, the points $\boldsymbol{x}_m$ should be chosen as the points within a parallelepiped centred in $\boldsymbol{x}_0$. In this way, since only the relative distance between points appears in the left hand side of (2.24), the Savitzky–Golay filter can be efficiently implemented by computing just once the Moore–Penrose pseudoinverse—or the singular value decomposition (SVD)—of the coefficient matrix. In one-dimension, the described filter coincides with the one shown in [91].

The effect of estimating the Laplacian from a linear kernel is investigated in [80], where noise propagation in stdEPT is rigorously studied. To this end, it is convenient to define a Laplacian estimator as a filter such that (i) it vanishes when applied to a constant or linear map, and (ii) it is constant, equal to the exact Laplacian, when applied to a quadratic map. It results that, under the assumption of spacially independent noise in the input measurement, summing the second derivatives with respect to x_i estimated by Savitzky-Golay filters with $\boldsymbol{r} = (2,0,0)$, $\boldsymbol{r} = (0,2,0)$ and $\boldsymbol{r} = (0,0,2)$, respectively, leads to the minimum noise propagation factor for a linear Laplacian estimator [80].

Since stdEPT relies on the assumption of local homogeneity of the electric properties, the choice of the kernel for the Laplacian computation can affect the recovery. In particular, when points that belong to different tissues are used for a Laplacian computation, the errors related to the non-fulfillment of the local homogeneity hypothesis arise. In order to limit, although not remove, this kind of errors, the derivatives should be estimated separately for each tissue, *i.e.* employing connected kernels made of points belonging to the same tissue. In a real case, this can be done by taking advantage from the images produced by the MRI scan [85, 93]. This can be done comparing the grey tone of neighbouring pixels—corresponding to near recovery points—[85], or elaborating the result of a segmentation algorithm [93]. In both cases, if the reference image is obtained with T_1 or T_2 weighting, then the hypothesis that same relaxation time coincides with same electric properties is introduced [64].

The adoption of shape-varying kernels for the Savitzky-Golay filter can be efficiently implemented in a computational code in the following way. For each point of the domain, find the shape of the kernel and check if it has already been used to compute a filter. If so, retrieve the already computed filter and apply it, else compute the filter, store it and apply it. An efficient data structure to collect the filters using as key the shapes is an hash table [94].

2.2 Dual-excitation EPT

Zhang and colleagues proposed the dual-excitation algorithm for MREPT in order to overcome the hypothesis of local homogeneity of the electric properties [59], the main drawback of stdEPT. The method, in the following denoted by deEPT, takes advantage of the technology for parallel transmission (pTX), in which more transmitter coils are employed and the magnetic field generated independently by each coil can be measured [95].

2.2.1 Derivation

The method derives from the generalised Helmholtz equation for the magnetic field (2.10), here repeated for the reader's convenience

$$\nabla\left(\tilde{\varepsilon}^{-1}\right)\times\nabla\times\boldsymbol{H}-\tilde{\varepsilon}^{-1}\nabla^2\boldsymbol{H}=\omega^2\mu_0\boldsymbol{H}\,, \tag{2.25}$$

which makes no assumption other than isotropic electric properties. The transverse components of the latter equation read

$$\frac{1}{\tilde{\varepsilon}}\frac{\partial\tilde{\varepsilon}}{\partial z}\left(\frac{\partial H_x}{\partial z}-\frac{\partial H_z}{\partial x}\right)+\frac{1}{\tilde{\varepsilon}}\frac{\partial\tilde{\varepsilon}}{\partial y}\left(\frac{\partial H_x}{\partial y}-\frac{\partial H_y}{\partial x}\right)-\omega^2\mu_0\tilde{\varepsilon}H_x=\nabla^2H_x\,, \tag{2.26}$$

and

$$\frac{1}{\tilde{\varepsilon}}\frac{\partial\tilde{\varepsilon}}{\partial z}\left(\frac{\partial H_y}{\partial z}-\frac{\partial H_z}{\partial y}\right)-\frac{1}{\tilde{\varepsilon}}\frac{\partial\tilde{\varepsilon}}{\partial x}\left(\frac{\partial H_x}{\partial y}-\frac{\partial H_y}{\partial x}\right)-\omega^2\mu_0\tilde{\varepsilon}H_y=\nabla^2H_y\,, \tag{2.27}$$

where the relation $\tilde{\varepsilon}\,\nabla(\tilde{\varepsilon}^{-1})=-\tilde{\varepsilon}^{-1}\nabla\tilde{\varepsilon}$ has been used. The first proposal of deEPT focuses on these two equations, assuming of begin able to measure the transverse

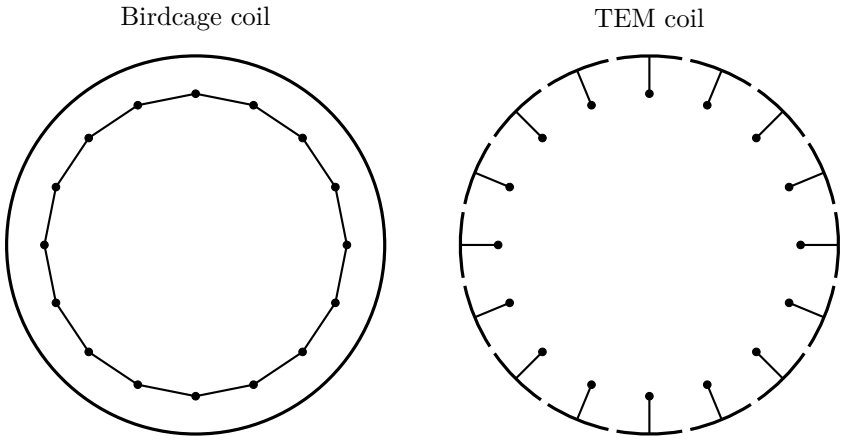

Fig. 2.4 Diagrammatic representation of a 16-legs birdcage coil (on the left) and a 16-legs TEM coil (on the right). The external circles outline the conductive shields, the black dots denote the legs and the lines represent the electric connections.

components of the magnetic field H_x and H_y and neglecting the derivatives of the longitudinal component H_z [59]. The dual-excitation algorithm treats both the complex permittivity $\tilde{\varepsilon}$ and its gradient components as algebraically independent unknowns. The measurement of the magnetic fields generated by at least a couple of excitations of the RF coil leads to a system of at least four linearly independent equations with four unknowns, which can be solved by least squares. Thus, deEPT is still a local direct method. Only some particular RF coils verify the hypothesis that the derivatives of the longitudinal component of the magnetic field are negligible. For example, surface coils are not suitable, whereas transverse electromagnetic (TEM) volume coils, similar to birdcage coils in which the leg return path follows the shield rather than the end rings [96, 97] (Fig. 2.4), satisfy the hypothesis better than birdcage coils [59]. This fact makes the method strongly coil-dependent.

This first and simplified version of the dual-excitation algorithm highlights an issue that will appear again in the global inverse method based on the contrast source inversion (CSI) technique (cf. Section 2.5). Since the longitudinal component of the electric field verifies

$$E_z = \frac{\mathrm{i}}{\omega\tilde{\varepsilon}} \left(\frac{\partial H_x}{\partial y} - \frac{\partial H_y}{\partial x} \right), \tag{2.28}$$

it acts as a denominator in the resolution of both (2.26) and (2.27). As a consequence, the recovered electric properties are affected by artefacts due to numerical errors in the regions where the longitudinal electric field component has low intensity [59].

In order to adapt the deEPT to the knowledge of only the positively rotating component of the magnetic field, equations (2.26) and (2.27) should be linearly combined to obtain

$$\frac{1}{\tilde{\varepsilon}}\frac{\partial\tilde{\varepsilon}}{\partial z}\frac{\partial H^+}{\partial z}+\frac{1}{\tilde{\varepsilon}}\left(\frac{\partial\tilde{\varepsilon}}{\partial y}-\mathrm{i}\frac{\partial\tilde{\varepsilon}}{\partial x}\right)\frac{1}{2}\left(\frac{\partial H_x}{\partial y}-\frac{\partial H_y}{\partial x}\right)-\omega^2\mu_0\tilde{\varepsilon}H^+=\nabla^2H^+, \quad (2.29)$$

where the gradient of the longitudinal component H_z has been neglected. Clearly, this equation involves explicitly both the transverse components of the magnetic field. Anyway, by neglecting $\partial H_z/\partial z$ in the Gauss law for magnetism, it is possible to write

$$\frac{1}{2}\left(\frac{\partial H_x}{\partial y}-\frac{\partial H_y}{\partial x}\right)=\frac{1}{2}\left(\frac{\partial H_x}{\partial y}-\frac{\partial H_y}{\partial x}+\mathrm{i}\left(\frac{\partial H_x}{\partial x}+\frac{\partial H_y}{\partial y}\right)\right)=\frac{\partial H^+}{\partial y}+\mathrm{i}\frac{\partial H^+}{\partial x}. \quad (2.30)$$

Thus, the central equation of deEPT is [98]

$$\frac{1}{\tilde{\varepsilon}}\frac{\partial\tilde{\varepsilon}}{\partial z}\frac{\partial H^+}{\partial z}+\frac{1}{\tilde{\varepsilon}}\left(\frac{\partial\tilde{\varepsilon}}{\partial y}-\mathrm{i}\frac{\partial\tilde{\varepsilon}}{\partial x}\right)\left(\frac{\partial H^+}{\partial y}+\mathrm{i}\frac{\partial H^+}{\partial x}\right)-\omega^2\mu_0\tilde{\varepsilon}H^+=\nabla^2H^+. \quad (2.31)$$

Introducing the vector $\boldsymbol{g}=\tilde{\varepsilon}^{-1}\nabla\tilde{\varepsilon}$ and its rotating component $g_+=g_x+\mathrm{i}g_y$ (for analogy, also $g_-=g_x-\mathrm{i}g_y$ can be introduced), equation (2.31) can be written with the compact notation [99]

$$\nabla H^+\cdot(g_+,-\mathrm{i}g_+,g_z)-\omega^2\mu_0\tilde{\varepsilon}H^+=\nabla^2H^+. \quad (2.32)$$

In this case, the algebraically independent unknowns are only three—the complex permittivity $\tilde{\varepsilon}$ and its derivatives g_+ and g_z—, thus the measurement of at least three linearly independent transmit sensitivities is required. Usually, in a birdcage coil the quadrature excitation is achieved by combining two independent linear excitations. Thus, at most two linearly independent measurements can be obtained by an ordinary birdcage coil, and special multi-channel transmit coils must be adopted to perform enough measurements of H^+ to solve (2.32). A multi-channel transmit coil that verifies the hypothesis of negligible spatial derivatives of the longitudinal component of the magnetic field H_z is the already mentioned TEM volume coil, which is used for pTX in ultra-high field (UHF) MRI with $B_0\geq 7\,\mathrm{T}$ [100]. It is worth noting that if it is known that the properties of the examined body do not vary along the longitudinal direction, then it is possible to assume $g_z=0$ and solve the system with respect to

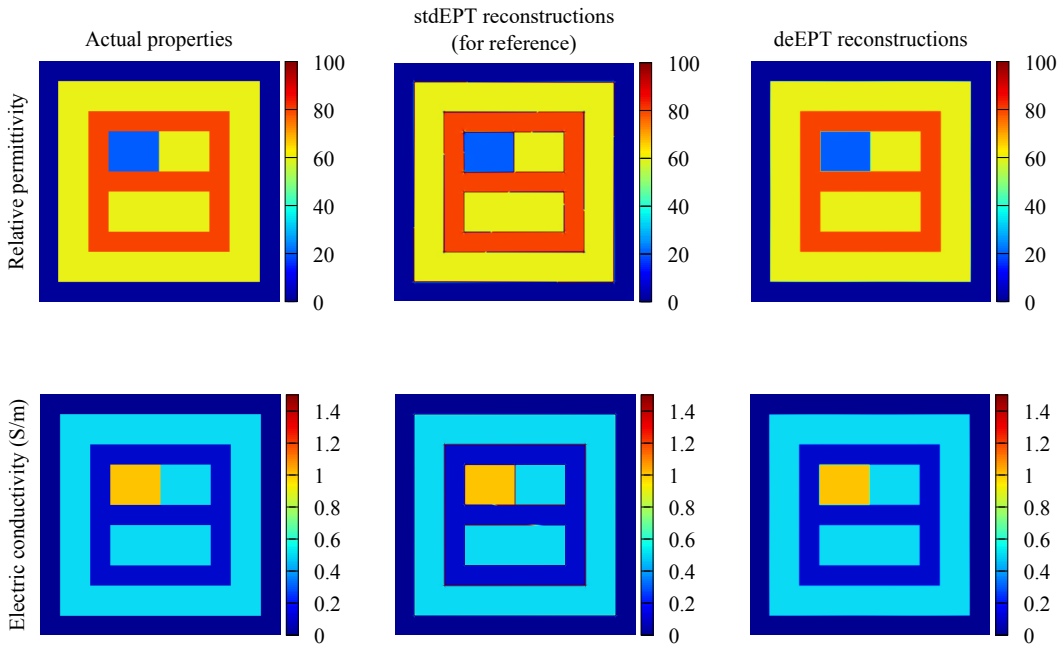

Fig. 2.5 The electric properties recovered by stdEPT and deEPT are reported for comparison. The same cylinder described in Fig. 2.1 is radiated by the electromagnetic field generated by a TEM coil with 8 legs at 128 MHz. The TEM coil has been simulated as 8 couples of line sources distributed uniformly on two circles of 10 cm and 12 cm radius. The transmit sensitivity of each couple of line sources H_j^+ has been computed numerically on a very fine discretisation of the domain (with a resolution of 0.2 mm) in order to make the numerical errors negligible. For the stdEPT reconstruction, the transmit sensitivity of the whole coil H^+ has been computed by linearly combining the transmit sensitivity of each leg. Both the magnitude and the phase of the transmit sensitivities have been assumed known exactly, although the transceive phase assumption does not fit for multi-channel transmit coils.

only two independent unknowns. In this particular two-dimensional situation, the measurements of a two-channel birdcage coil would be sufficient to perform deEPT.

The reconstruction of the electric properties achieved by deEPT based on (2.32) applied to the transmit sensitivities of a TEM coil with 8 legs is reported in Fig. 2.5, where both magnitude and phase of the measured fields are assumed to be known exactly. A big improvement with respect to stdEPT can be noticed—no artefacts are present in the images, just an erroneous smoothing at the interfaces, due to numerical diffusion, appear. Anyway, this result is optimistic, because only the transceive phase $\varphi^{\pm}$ can be measured by MRI scanners and, in general, the transceive phase assumption (2.16) does not hold for multi-channel transmit coils. Thus, the

estimation of the actual phase of the transmit sensitivity is a critical issue for a practical implementation of deEPT [98].

2.2.2 Phase retrieval

Before introducing algorithms for the determination of the phase of the transmit sensitivity of a RF coil, it is convenient to clarify which information is contained in the transceive phase. At least two situations can be distinguished for a multi-channel transmit coil:

i. The receive coil is different from the transmit coil and has only one channel. In this case, the transceive phase measured for the j-th channel is $\varphi_j^{\pm} = \varphi_j^{+} - \tilde{\varphi}^{-}$ and the relative transmit phase of channel j with respect to channel k can be computed without approximations as $\varphi_j^{+} - \varphi_k^{+} = \varphi_j^{\pm} - \varphi_k^{\pm}$. Adopting φ_0^{+} as reference phase, the j-th transmit sensitivity can be written as

$$\mu_0 H_j^{+} = \mu_0 |H_j^{+}| \mathrm{e}^{\mathrm{i}(\varphi_0^{+} + \varphi_j^{+;\mathrm{r}})}, \tag{2.33}$$

where $\varphi_j^{+;\mathrm{r}}$ denotes the relative transmit phase of channel j with respect to the reference phase.

ii. The transmit coil is used also as receive coil. In this case the RF coil is usually referred to as multi-channel transceive coil [61, 98] and a different signal is measured by each channel. The transceive phase measured by the n-th receiver channel for the j-th transmit channel is $\varphi_{jn}^{\pm} = \varphi_j^{+} - \varphi_n^{-}$, where the receive phase is written without the tilde because it is the actual phase of the negatively rotating component of $\boldsymbol{B}_{1,n}$. As in the previous case, this allows to compute without approximations the relative phases and to write for the j-th channel in addition to (2.33)

$$\mu_0 H_j^{-} = \mu_0 |H_j^{-}| \mathrm{e}^{\mathrm{i}(\varphi_0^{+} - \varphi_{0j}^{\pm})}. \tag{2.34}$$

Both the cases have been investigated for phase retrieval in [61, 101, 102].

Assuming locally homogeneous electric properties, permittivity and conductivity can be written as functions of the transmit magnitude and phase for each channel as described for stdEPT. Since constant, the properties are independent of the considered channel. So, the right hand sides of (2.12) and (2.13) can be made equal

for the generic channel $j \neq 0$ and the reference channel $j = 0$ leading respectively to [102]

$$2\nabla\varphi_j^{+;\mathrm{r}} \cdot \nabla\varphi_0^{+} = \frac{\nabla^2|H_j^+|}{|H_j^+|} - \frac{\nabla^2|H_0^+|}{|H_0^+|} - |\nabla\varphi_j^{+;\mathrm{r}}|^2\,, \tag{2.35}$$

and

$$\left(\frac{\nabla|H_0^+|}{|H_0^+|} - \frac{\nabla|H_j^+|}{|H_j^+|}\right) \cdot \nabla\varphi_0^{+} = \frac{1}{2}\nabla^2\varphi_j^{+;\mathrm{r}} + \frac{\nabla|H_j^+|}{|H_j^+|} \cdot \nabla\varphi_j^{+;\mathrm{r}}\,. \tag{2.36}$$

The unknown spatial derivatives of the reference phase φ_0^+ can be estimated solving in the least squares sense a system of the latter equations written for at least a couple of channels $j \neq 0$ [102]. The gradient of the reference phase is enough to perform deEPT [103]. Anyway, it can be integrated assuming a null phase in any point of the domain to know the absolute phase of any channel. An analogous procedure is described in [101], where the receive phase $\tilde{\varphi}^-$ is recovered instead of the reference phase.

The hypothesis of local homogeneity introduces errors in the estimated gradient similar to the ones described in the discussion of stdEPT. To avoid this issue, a different procedure based on the Gauss law for magnetism has been proposed assuming a negligible spatial derivative for the longitudinal component of the magnetic field [61],

$$\frac{\partial H_x}{\partial x} + \frac{\partial H_y}{\partial y} = \frac{\partial H^+}{\partial x} - \mathrm{i}\frac{\partial H^+}{\partial y} + \frac{\partial\,(H^-)^*}{\partial x} + \mathrm{i}\frac{\partial\,(H^-)^*}{\partial y} = 0\,. \tag{2.37}$$

The negatively rotating component H^- can be partially measured by multi-channel transceive coils. In particular, its phase can be expressed as a function of the reference phase as depicted in (2.34), whereas its magnitude can be empirically estimated under symmetry assumptions on the coil structure and the examined body [61]. By replacing expressions (2.33) and (2.34) in (2.37) and dividing it by $\mathrm{e}^{\mathrm{i}\varphi_0^+}$, the

following equation is obtained for each channel j,

$$\begin{aligned}\left(\frac{\partial|H_j^-|}{\partial x}+\mathrm{i}\frac{\partial|H_j^-|}{\partial y}+\mathrm{i}|H_j^-|\left(\frac{\partial\varphi_{0j}^{\pm}}{\partial x}+\mathrm{i}\frac{\partial\varphi_{0j}^{\pm}}{\partial y}\right)\right)\mathrm{e}^{\mathrm{i}\varphi_{0j}^{\pm}}\,\mathrm{e}^{-\mathrm{i}2\varphi_0^+}+\\ \mathrm{i}|H_j^+|\mathrm{e}^{\mathrm{i}\varphi_j^{+;\mathrm{r}}}\left(\frac{\partial\varphi_0^+}{\partial x}-\mathrm{i}\frac{\partial\varphi_0^+}{\partial y}\right)-\mathrm{i}|H_j^-|\mathrm{e}^{\mathrm{i}\varphi_{0j}^{\pm}}\left(\frac{\partial\varphi_0^+}{\partial x}+\mathrm{i}\frac{\partial\varphi_0^+}{\partial y}\right)\mathrm{e}^{-\mathrm{i}2\varphi_0^+}=\\ -\left(\frac{\partial|H_j^+|}{\partial x}-\mathrm{i}\frac{\partial|H_j^+|}{\partial y}+\mathrm{i}|H_j^+|\left(\frac{\partial\varphi_j^{+;\mathrm{r}}}{\partial x}-\mathrm{i}\frac{\partial\varphi_j^{+;\mathrm{r}}}{\partial y}\right)\right)\mathrm{e}^{\mathrm{i}\varphi_j^{+;\mathrm{r}}}.\end{aligned} \tag{2.38}$$

The latter equation is treated as non-linear in [61]. Anyway, a linear system to be solved in the least squares sense can be deduced adopting as algebraically independent unknowns $(\partial\varphi_0^+/\partial x-\mathrm{i}\partial\varphi_0^+/\partial y)$, $\mathrm{e}^{-\mathrm{i}2\varphi_0^+}$ and $(\partial\varphi_0^+/\partial x+\mathrm{i}\partial\varphi_0^+/\partial y)\mathrm{e}^{-\mathrm{i}2\varphi_0^+}$, similarly to the treatment of non-linearity used in [99, 103]. As can be seen in Fig. 2.6, by solving (2.38), the gradient of the reference phase is retrieved without the systematic error at the interfaces between materials with different electric properties that occurs with the previous method. Anyway, since its strong assumptions, this efficient approach can be applied only when particular multi-channel transceive coils are employed and the ensemble of RF coil and examined sample satisfies symmetry assumptions.

2.2.3 Extensions of the method

As shown during the description of the techniques for the absolute phase retrieval of $\boldsymbol{B}_1$, both transmit and receive sensitivities can be measured in particular situations. The equation for the receive sensitivity H_j^- of the j-th coil

$$\nabla\left(\tilde{H}^-\right)^*\cdot(g_-,\mathrm{i}g_-,g_z)-\omega^2\mu_0\tilde{\varepsilon}\left(\tilde{H}^-\right)^*=\nabla^2\left(\tilde{H}^-\right)^* \tag{2.39}$$

can be derived in the same way as (2.32) observing that

$$\frac{1}{2}\left(\frac{\partial H_x}{\partial y}-\frac{\partial H_y}{\partial x}\right)=\frac{1}{2}\left(\frac{\partial H_x}{\partial y}-\frac{\partial H_y}{\partial x}-\mathrm{i}\left(\frac{\partial H_x}{\partial x}+\frac{\partial H_y}{\partial y}\right)\right)=\frac{\partial\left(H^-\right)^*}{\partial y}-\mathrm{i}\frac{\partial\left(H^-\right)^*}{\partial x}, \tag{2.40}$$

in analogy with (2.30). Equation (2.39) can be coupled with (2.32) interpreting as algebraically independent unknowns the complex permittivity $\tilde{\varepsilon}$ and its derivatives g_+, g_- and g_z. It is worth noting that in this case at least four equations are required

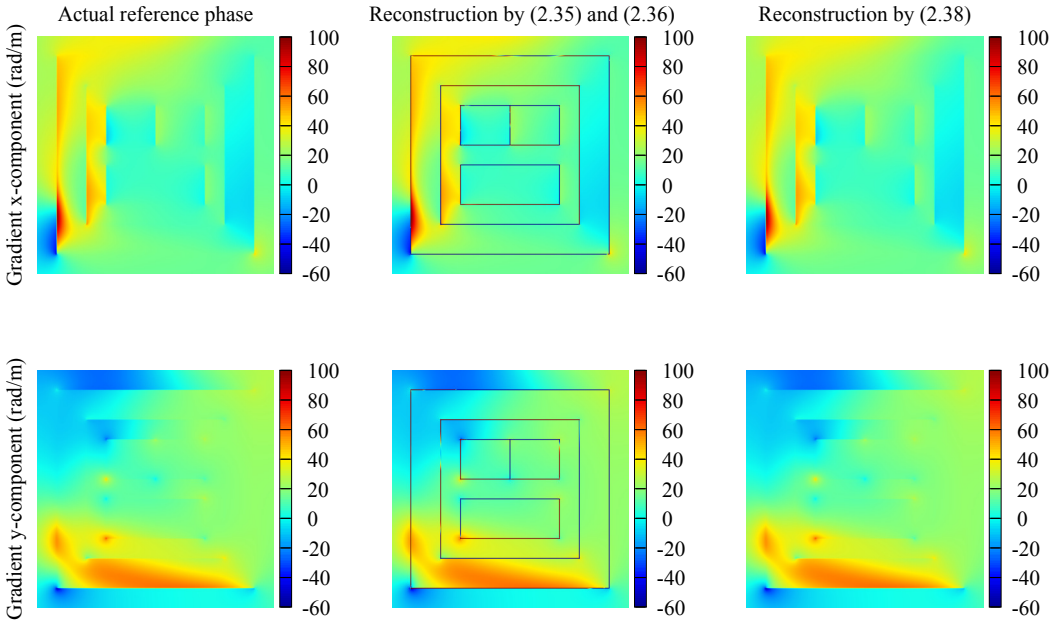

Fig. 2.6 The x and y components of the gradient of the reference phase recovered by both techniques for phase retrieval are reported for comparison. The same cylinder described in Fig. 2.1 is radiated by the same source described in Fig. 2.5. The magnitude of transmit and receive sensitivity, the relative receive phases and the transceive phases have been computed numerically on a very fine discretisation of the domain (with a resolution of 0.2 mm) and have been used as noise-free input for the reconstructions. The systematic error that appears solving (2.35) and (2.36) is not present in the solution of (2.38).

to solve the system, namely the measurement of the transmit and receive sensitivities of at least two linearly independent excitations are needed. This fact justifies the choice of the name dual-excitation algorithm.

Since the knowledge of g_+, g_- and g_z implies the whole knowledge of the gradient $\boldsymbol{g} = \tilde{\varepsilon}^{-1}\nabla\tilde{\varepsilon} = \nabla\log\tilde{\varepsilon}$, it is possible to estimate the electric properties by integration of $\boldsymbol{g}$ with the information of a seed point as initial value. This procedure has proved to be more robust in the treatment of noisy input than the direct deEPT, because of the low-pass filtering effect of the integration, and has been called gradient-based EPT (gEPT) [99]. Because of the integration step, gEPT is a borderline technique between local and global methods. Together with the introduction of gEPT, in [99] it is suggested to consider the reference phase gradient as an unknown of the inverse problem itself. It is possible to recover both $\boldsymbol{g}$ and $\nabla\varphi_0^+$ solving in the least squares sense a linear system obtained introducing the measured quantities $H_j^{+;\mathrm{r}} =$

$|H_j^+|\mathrm{e}^{\mathrm{i}\varphi_j^{+;\mathrm{r}}}$ and $H_j^{-;\mathrm{r}} = |H_j^-|\mathrm{e}^{-\mathrm{i}\varphi_{0j}^{\pm}}$, which, in accordance with (2.33) and (2.34), leads to $H_j^+ = H_j^{+;\mathrm{r}}\mathrm{e}^{\mathrm{i}\varphi_0^+}$ and $H_j^- = H_j^{-;\mathrm{r}}\mathrm{e}^{\mathrm{i}\varphi_0^+}$. By computing explicitly the gradient and the Laplacian of the sensitivities, equations (2.32) and (2.39) can be rewritten as

$$-\mathrm{i}2\nabla H_j^{+;\mathrm{r}}\cdot\nabla\varphi_0^+ + \nabla H_j^{+;\mathrm{r}}\cdot(g_+,-\mathrm{i}g_+,g_z) + H_j^{+;\mathrm{r}}\vartheta_+ = \nabla^2 H_j^{+;\mathrm{r}}, \tag{2.41}$$

and

$$\mathrm{i}2\nabla(H_j^{-;\mathrm{r}})^*\cdot\nabla\varphi_0^+ + \nabla(H_j^{-;\mathrm{r}})^*\cdot(g_-,\mathrm{i}g_-,g_z) + (H_j^{-;\mathrm{r}})^*\vartheta_- = \nabla^2(H_j^{+;\mathrm{r}})^*, \tag{2.42}$$

where $\vartheta_+ = |\nabla\varphi_0^+|^2 - \mathrm{i}\nabla^2\varphi_0^+ + \mathrm{i}\nabla\varphi_0^+\cdot(g_+,-\mathrm{i}g_+,g_z) - \omega^2\mu_0\tilde{\varepsilon}$ and $\vartheta_- = |\nabla\varphi_0^+|^2 + \mathrm{i}\nabla^2\varphi_0^+ - \mathrm{i}\nabla\varphi_0^+\cdot(g_-,\mathrm{i}g_-,g_z) - \omega^2\mu_0\tilde{\varepsilon}$ collect the non-linearities of the equations. Thus, the algebraically independent unknowns are the real gradient of the reference phase $\nabla\varphi_0^+$, the complex gradient $\boldsymbol{g}$ and the complex auxiliary variables ϑ_+ and ϑ_-. At least four linearly independent excitations are needed in order to solve this problem.

A major issue in deEPT and, in particular, gEPT is the estimation of the magnitude of the receive sensitivity $|H_j^-|$, which relies on symmetry assumptions on the coil structure and the examined body [61]. The quantity that actually can be measured is the product between the equivalent proton density ρ and the receive magnitude, which, in general, cannot be easily disentangled. In order to reduce the coil- and subject-dependence of the method, two alternatives have been proposed:

i. Since the measurable part of the receive sensitivity is $H_j^{-;\mathrm{s}} = \rho H_j^{-;\mathrm{r}}$, equation (2.39) can be elaborated by noting that $H_j^- = \rho^{-1}H_j^{-;\mathrm{s}}\mathrm{e}^{\mathrm{i}\varphi_0^+}$ to obtain

$$\begin{aligned}&\mathrm{i}2\nabla(H_j^{-;\mathrm{s}})^*\cdot\nabla\varphi_0^+ - 2\nabla(H_j^{-;\mathrm{s}})^*\cdot\nabla\log\gamma + \\ &\quad\nabla(H_j^{-;\mathrm{s}})^*\cdot(g_-,\mathrm{i}g_-,g_z) + (H_j^{-;\mathrm{s}})^*\vartheta_-^{\mathrm{s}} = \nabla^2(H_j^{-;\mathrm{s}})^*,\end{aligned} \tag{2.43}$$

where $\gamma = \rho^{-1}$ and $\vartheta_-^{\mathrm{s}} = \vartheta_- - \nabla^2\log\gamma - |\nabla\log\gamma|^2 + \nabla\log\gamma\cdot(g_-,\mathrm{i}g_-,g_z) + \mathrm{i}2\nabla\varphi_0^+\cdot\nabla\log\gamma$. The latter equation, coupled with (2.41), can be solved in the least squares sense with respect to the linearly independent unknowns $\nabla\varphi_0^+$, $\nabla\log\gamma$, $\boldsymbol{g}$, ϑ_+ and ϑ_-^{p}, provided that at least four linearly independent excitations are available in order to collect enough equations [104, 103]. It is worth noting that $\nabla\varphi_0^+$ and $\nabla\log\gamma$ are real vectors, whereas the remaining unknowns are complex. This approach is very similar to the local Maxwell

tomography (LMT) proposed by Sodickson and colleagues as a particular implementation of MREPT that makes no assumptions on non-measurable quantities [71, 105].

ii. Relying just on (2.41) it is possible to recover $\nabla\varphi_0^+$, g_+, g_z and ϑ_+. These quantities can be elaborated to extract an estimation of the complex permittivity $\tilde{\varepsilon}_0$ from ϑ_+. In order to take advantage of the low-pass filtering properties of the integral operator, the information stored in g_+ and g_z can be exploited by estimating the complex permittivity in the whole region as

$$\tilde{\boldsymbol{\varepsilon}} = \arg\min_{\tilde{\boldsymbol{\varepsilon}}^*} \left(\left\| \tilde{\boldsymbol{g}}_+ - \boldsymbol{g}_+ \right\|^2 + \left\| \tilde{\boldsymbol{g}}_z - \boldsymbol{g}_z \right\|^2 + \lambda \left\| \log \frac{\tilde{\boldsymbol{\varepsilon}}}{\tilde{\boldsymbol{\varepsilon}}_0} \right\|^2 \right), \tag{2.44}$$

where the bold symbols denote the lists of the corresponding quantities evaluated in each voxel of the domain, $\tilde{\boldsymbol{g}} = \nabla \log \tilde{\varepsilon}$ and λ is a regularisation coefficient, which can be chosen following the L-curve method [106]. In the last norm of the latter relation, the logarithm has been introduced in order to allow to find the minimum by solving a linear system. More recently, the possibility to estimate g_x and g_y from (2.41) by performing a rigid rotation of both the sample and the RF coil inside the MRI scanner has been proposed in [107].

2.3 Zero echo-time EPT

Both stdEPT and deEPT are based on B_1-mapping techniques, which usually require a long scan time and have a low signal-to-noise ratio (SNR) with respect to other clinical imaging sequences [75]. In particular, in order to perform deEPT or gEPT, the B_1-mapping scan must be repeated for each transmit channel increasing the total scan time for the patient significantly. MREPT from zero echo-time sequences (zteEPT) has been proposed to reduce the scan time and to increase the SNR of the input [75]. This method deserves an in-depth discussion because, by using as input a complex image instead of the usual transmit sensitivity, it leads to unique advantages [108].

When the MRI scan is performed with low flip angle α, such that $\sin\alpha \sim \alpha$, the achieved image can be approximately described by the relation (cf. Appendix A)

$$\mathfrak{I} = \mathfrak{I}_0 \, B_1^+ \left(\tilde{B}^-\right)^* , \tag{2.45}$$

where $\mathfrak{I}_0$ is the complex image determined by the effective proton density and other tissue properties and independent of the transmit and the receive sensitivities. Relation (2.45) has been used in the first iterative implementation of MREPT [62]. In general, the phase of $\mathfrak{I}_0$ can vary in space because of the presence of $\boldsymbol{B}_0$ inhomogeneities, chemical shifts and magnetic fields due to the eddy currents induced in the RF coil by the gradient coils switching [60]. Anyway, the adoption of a zero echo-time sequence with limited gradient switching reduces the error in neglecting $\mathfrak{I}_0$ phase [75, 109].

Under the hypothesis of locally homogeneous electric properties, the Helmholtz equation (2.3) can be specialised for both transmit and receive sensitivities. By adding the first specialisation multiplied by $(\tilde{H}^-)^*$ and the second one multiplied by H^+, the following equation results,

$$\nabla^2 \left(H^+(\tilde{H}^-)^*\right) + 2\kappa^2 H^+(\tilde{H}^-)^* - 2\nabla H^+ \cdot \nabla(\tilde{H}^-)^* = 0 , \tag{2.46}$$

where $\kappa^2 = \omega^2\mu_0\tilde{\varepsilon}$ is the square of the propagation coefficient of the radiation. By introducing the variables $a = \sqrt{H^+(\tilde{H}^-)^*}$ and $b = \sqrt{(\tilde{H}^-)^*/H^+}$, the latter equation divided by $2a^2$ can be rewritten as

$$\frac{\nabla^2 a}{a} + \kappa^2 + \underbrace{\frac{|\nabla a|^2}{a^2} - \frac{1}{a^2}\nabla\left(\frac{a}{b}\right)\cdot\nabla(ab)}_{\kappa_{\text{err}}^2} = 0 . \tag{2.47}$$

The quantity κ_{err}^2 is neglected in zteEPT, in which it plays the role of a distributed systematic error additional to the systematic error at the interfaces due to the almost homogeneous assumption. It can be compared to the systematic error introduced in stdEPT by the transceive phase assumption (2.16). Precisely, κ_{err}^2 can be further

elaborated to get

$$\begin{aligned}\kappa_{\text{err}}^2 &= \frac{1}{a^2}\left(|\nabla a|^2 - \left(\frac{\nabla a}{b} - \frac{a}{b^2}\nabla b\right)\cdot(a\nabla b + b\nabla a)\right) \\ &= \frac{1}{b^2}|\nabla b|^2 = \frac{1}{4}|\nabla \log b^2|^2 = \frac{1}{4}\left|\nabla \log\left(\frac{(\tilde{H}^-)^*}{H^+}\right)\right|^2,\end{aligned} \tag{2.48}$$

which is null when $H^+ = (\tilde{H}^-)^*$ and is negligible when the equality is almost true, like in the case of birdcage coil in quadrature feed with polarisation switching. In particular, κ_{err}^2 tends towards zero as the square of the relative difference between H^+ and $(\tilde{H}^-)^*$ [75], whereas the error introduced in stdEPT by the transceive phase assumption decreases linearly with the difference of transmit and receive phases [75]. Thus, the electric properties recovered by zteEPT are theoretically more accurate than those obtained by stdEPT with the transceive phase assumption.

Neglecting κ_{err}^2 in (2.47), the fundamental equation for zteEPT reads

$$\tilde{\varepsilon} = -\frac{\nabla^2\sqrt{H^+(\tilde{H}^-)^*}}{\omega^2\mu_0\sqrt{H^+(\tilde{H}^-)^*}}. \tag{2.49}$$

The latter equation does not change if multiplied and divided by $\mu_0\sqrt{\Im_0}$. Depending just on the physical properties of the examined body, $\Im_0$ can be assumed to be constant in each tissue. Therefore, $\Im_0$ can be moved in the Laplacian operator introducing an error located only at the interfaces between tissues, where the assumption of local homogeneity already makes the electric properties recovery untrustworthy. So, the image (2.45) can be directly used as input for zteEPT using the equation [75]

$$\tilde{\varepsilon} = -\frac{\nabla^2\sqrt{\Im}}{\omega^2\mu_0\Im}. \tag{2.50}$$

The image-based reconstruction (2.50) has been adopted also in [108], although in this case a fast spin-echo sequence is used, which involves a high flip angle. The error made in this way has been estimated to be less than the systematic error due to the phase-based stdEPT approach in a 3 T scanner [108].

2.4 Convection-reaction EPT

Although deEPT leads to more accurate results than stdEPT by including the gradient of the electric properties in the Helmholtz equation, it requires more than one measurement of linearly independent transmit sensitivities to work. In order to perform the imaging of the electric properties relying on just one measurement and not neglecting the gradient of the electric properties, a linear convection-reaction equation can be written for the properties and solved numerically as a partial differential equation (PDE) problem [72]. This method is denoted by crEPT.

2.4.1 Derivation

Equation (2.32), which has been derived from the generalised Helmholtz equation (2.10) under the assumption of negligible derivatives of the longitudinal component of the magnetic field, can be written focusing on the complex permittivity $\tilde{\varepsilon}$ as

$$\tilde{\varepsilon}^{-1}\nabla\tilde{\varepsilon}\cdot\boldsymbol{\beta}^{+}-\omega^{2}\mu_{0}\tilde{\varepsilon}H^{+}=\nabla^{2}H^{+}\,, \tag{2.51}$$

where $\boldsymbol{\beta}^{+}=\nabla H^{+}-\mathrm{i}\nabla\times(H^{+}\hat{\boldsymbol{z}})$. Although, the latter equation is non-linear with respect to $\tilde{\varepsilon}$, since $\tilde{\varepsilon}^{-2}\nabla\tilde{\varepsilon}=-\nabla(\tilde{\varepsilon}^{-1})$, the change of variable $u=\tilde{\varepsilon}^{-1}$ leads to the linear equation with respect to the inverse of the complex permittivity [72]

$$\boldsymbol{\beta}^{+}\cdot\nabla u+\nabla^{2}H^{+}u=-\omega^{2}\mu_{0}H^{+}\,. \tag{2.52}$$

Despite its parameters and its unknown are complex-valued functions, this equation looks like the classic convection-reaction equation. Thus, provided appropriate boundary conditions for u, equation (2.52) can be solved approximately by some numerical discretisation. Although this method requires the estimation of the spatial derivatives of the transmit sensitivity, which is a very noise-sensitive task, it integrates the results in a global fashion by solving a PDE. Thus, it limits the noise propagation with respect to stdEPT as is the case for gEPT. In the proposed taxonomy for MREPT techniques, crEPT turns out to be a global direct method.

In [72], the problem is solved in two dimensions—in a transverse section—by a finite difference method based on an unstructured triangular mesh assuming Dirichlet boundary conditions—namely, the electric properties are given on the boundary of

the examined domain. Precisely, the unknown function u is approximated with a piecewise affine function u_δ such that

$$u_\delta(x,y) = \sum_{i=1}^{3} u_{e,i}\phi_{e,i}(x,y)\,, \qquad (x,y) \in T_e\,, \tag{2.53}$$

being T_e the e-th triangle of the mesh, $u_{e,i}$ the value of u_δ at the i-th vertex of T_e and $\phi_{e,i}(x,y)$ the linear shape function whose value is 1 at the i-th vertex of T_e and 0 at the other vertices of T_e. By writing $\phi_{e,i}(x,y) = a_{e,i}x + b_{e,i}y + c_{e,i}$, because of the linearity of the derivative operator, it follows that

$$\nabla u_\delta(x,y) = \sum_{i=1}^{3} u_{e,i}(a_{e,i}, b_{e,i})\,, \qquad (x,y) \in T_e\,. \tag{2.54}$$

Thus, the evaluation of (2.52) in the barycentre of triangle T_e leads to the algebraic equation

$$\sum_{i=1}^{3} \left((a_{e,i}, b_{e,i}) \cdot \boldsymbol{\beta}_e^+ + \frac{1}{3}(\nabla^2 H^+)_e \right) u_{e,i} = -\omega^2 \mu_0 H_e^+\,. \tag{2.55}$$

In $\boldsymbol{\beta}_e^+$, $(\nabla^2 H^+)_e$ and H_e^+ the subscript e denotes the evaluation in the barycentre of T_e. For nodes on the boundary, $u_{e,i}$ is given by the Dirichlet condition and its term in the sum can be moved on the right hand side. The collection of equation (2.55) written for each triangle in the mesh is an algebraic linear system with more equations than unknowns, which can be solved in the least squares sense. Reasoning with tetrahedra instead of triangles, the same procedure can be described in three dimensions.

The finite difference method on triangular meshes described above [72] is used effectively on unstructured meshes in [72], but it appears to be unstable when applied to structured meshes, as the ones that are obtained naturally from the results given by a MRI experiment, collected in a Cartesian grid. The discretisation of the conservative form of (2.52) seems to be more stable from a numerical viewpoint. By virtue of the definition of $\boldsymbol{\beta}^+$, since the divergence of a rotation is always null, equation (2.52) can be written in conservative form as

$$\nabla \cdot \left(\boldsymbol{\beta}^+ u \right) = -\omega^2 \mu_0 H^+\,. \tag{2.56}$$

The latter equation can be efficiently discretised employing the finite difference method or the finite volume method. At first order of accuracy, both methods

discretise (2.56) with the same algebraic equation for the generic node (x_i, y_j, z_k) of a uniform Cartesian grid,

$$\begin{aligned}\frac{(\beta_x^+ u)_{i+1,j,k} - (\beta_x^+ u)_{i-1,j,k}}{2\Delta x} + \frac{(\beta_y^+ u)_{i,j+1,k} - (\beta_y^+ u)_{i,j-1,k}}{2\Delta y} + \\ \frac{(\beta_z^+ u)_{i,j,k+1} - (\beta_z^+ u)_{i,j,k-1}}{2\Delta z} = -\omega^2 \mu_0 H^+_{i,j,k},\end{aligned} \tag{2.57}$$

where the subscripts denote the node in which the considered quantity is evaluated and Δx, Δy and Δz are the steps of the grid. Besides the stability of the results, that shows anyway high frequency spurious oscillations, the use of the conservative form (2.56) has the benefit of avoiding the estimation of the Laplacian from noisy measurements, which is instead needed in (2.55).

The reconstruction achieved by the discretisation (2.57) of the conservative form applied to a two-dimensional model problem is reported in Fig. 2.7. The presence of high frequency spurious oscillations whose wavelength is about two pixels can be appreciated. Anyway, this error can be easily removed by post-processing the solution, for example applying a low-pass Gaussian filter with a standard deviation of 1 pixel (Fig. 2.7), so it does not undermine the method. In addition, the region around the centre of the domain shows an artefact in the recovery of both the electric properties. As described above for the dual-excitation algorithm (cf. Section 2.2) and below for the global inverse method based on the CSI technique (cf. Section 2.5), this fact is related to the low intensity of the longitudinal component of the electric field

$$E_z = \frac{\mathrm{i}}{\omega \tilde{\varepsilon}} \left(\frac{\partial H_x}{\partial y} - \frac{\partial H_y}{\partial x} \right), \tag{2.58}$$

which corresponds to negligible x and y components of $\boldsymbol{\beta}^+$ [72]. A couple of strategies have been proposed in [72] to overcome this issue:

i. In the region of low E_z, the so-called constrained crEPT recovers the electric properties by stdEPT. The obtained values are then used as additional Dirichlet boundary conditions for the PDE. This technique is unreliable when there are material boundaries in the artefact region;

ii. The dual-excitation crEPT uses two sets of transmit sensitivity measurements that have disjoint regions of low E_z, so that every node in the domain has at least one informative equation. By this way, the number of equations in

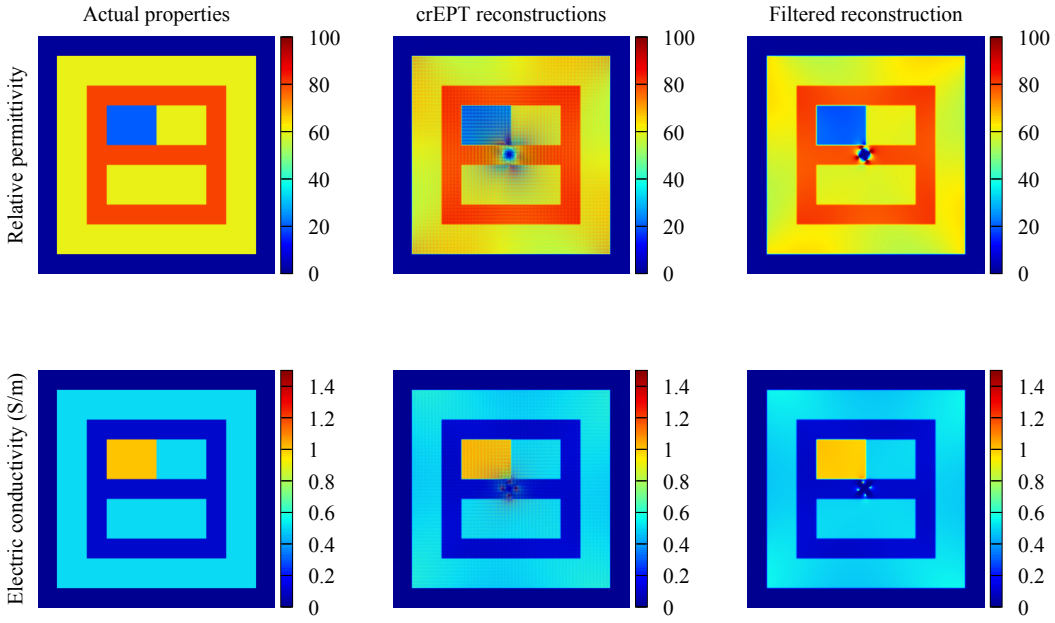

Fig. 2.7 The electric properties recovered by crEPT are reported for a two-dimensional model problem. The same cylinder described in Fig. 2.1 is radiated by the electromagnetic field generated by the same birdcage coil described in Fig. 2.2. The transmit sensitivity H^+ has been computed numerically on a very fine discretisation of the domain (with a resolution of 0.2 mm) in order to make the numerical errors negligible. Both magnitude and phase of H^+ are assumed known exactly. The properties recovered by crEPT are filtered in order to remove the spurious oscillations by applying a Gaussian filter with a standard deviation of 1 pixel.

the linear system that discretises the problem is doubled and the system is solved in the least squares sense. In order to guarantee the validity of the transceive phase assumption for each measurement, a traditional birdcage coil can be used to measure the transmit sensitivity just in presence of the body and when a padding of gels and slurries is attached to the body. Since it requires more than one measurement and the introduction of external components (the padding), this one may not be the preferable solution.

Despite its demanding computational cost and its numerical instability problems, crEPT is an interesting technique that combines the quality of deEPT—taking into account the gradient of the electric properties—with the need of stdEPT of just few measurements. Thus, crEPT has been further investigated in [110] looking for a phase-based version along the lines of (2.15).

2.4.2 Phase-based convection-reaction EPT

In order to obtain a PDE for the electric conductivity whose coefficients are related only to the measurable transceive phase, it is convenient to start again from the generalised Helmholtz equation (2.51). By distinguishing between the magnitude and the phase of the transmit sensitivity $H^+ = |H^+|\mathrm{e}^{\mathrm{i}\varphi^+}$, the convective-like coefficient $\boldsymbol{\beta}^+$ can be expressed as

$$\boldsymbol{\beta}^+ = \left(\nabla|H^+| - \mathrm{i}\nabla\times(|H^+|\hat{\boldsymbol{z}})\right)\mathrm{e}^{\mathrm{i}\varphi^+} + \left(\nabla\varphi^+ - \mathrm{i}\nabla\times(\varphi^+\hat{\boldsymbol{z}})\right)\mathrm{i}H^+. \tag{2.59}$$

For all the transmit coils that look for an almost homogeneous flip angle, like for example the birdcage coil, the magnitude of H^+ can be assumed constant, making the first term of (2.59) negligible. Under the assumption that such a coil is used, in the following it is assumed that $\boldsymbol{\beta}^+ = (\nabla\varphi^+ - \mathrm{i}\nabla\times(\varphi^+\hat{\boldsymbol{z}}))\mathrm{i}H^+$, and consequently $\nabla^2 H^+ = \nabla\cdot\boldsymbol{\beta}^+ = (\nabla^2\varphi^+ + \mathrm{i}|\nabla\varphi^+|^2)\mathrm{i}H^+$. Thus, equation (2.51) can be approximated with

$$\tilde{\varepsilon}^{-1}\nabla\tilde{\varepsilon}\cdot\left(\nabla\varphi^+ - \mathrm{i}\nabla\times(\varphi^+\hat{\boldsymbol{z}})\right) + \mathrm{i}\omega^2\mu_0\tilde{\varepsilon} = \nabla^2\varphi^+ + \mathrm{i}|\nabla\varphi^+|^2. \tag{2.60}$$

Similarly, it is possible to write equation (2.39), whose components involve the receive sensitivity $\tilde{H}^- = |\tilde{H}^-|\mathrm{e}^{\mathrm{i}\tilde{\varphi}^-}$, as

$$\tilde{\varepsilon}^{-1}\nabla\tilde{\varepsilon}\cdot\boldsymbol{\beta}^- - \omega^2\mu_0\tilde{\varepsilon}(\tilde{H}^-)^* = \nabla^2(\tilde{H}^-)^*, \tag{2.61}$$

where $\boldsymbol{\beta}^- = (\nabla\tilde{H}^- - \mathrm{i}\nabla\times(\tilde{H}^-\hat{\boldsymbol{z}}))^*$, and so $\nabla\cdot\boldsymbol{\beta}^- = \nabla^2(\tilde{H}^-)^*$. The possibility to perform imaging using the latter equation instead of (2.52) in order to take advantage of the many simultaneous measurements available from multiple receiver coils has been investigated in [111]. Assuming that the receive sensitivity fulfills relation $|\nabla|\tilde{H}^-|| \simeq 0$—also the linear combination of multiple receive sensitivities can be used to this end [84]—the coefficients of (2.61) can be approximated by $\boldsymbol{\beta}^- = -(\nabla\tilde{\varphi}^- + \mathrm{i}\nabla\times(\tilde{\varphi}^-\hat{\boldsymbol{z}}))\mathrm{i}(\tilde{H}^-)^*$ and $\nabla^2(\tilde{H}^-)^* = (-\nabla^2\tilde{\varphi}^- + \mathrm{i}|\nabla\tilde{\varphi}^-|^2)\mathrm{i}(\tilde{H}^-)^*$. So, equation (2.61) leads to

$$\tilde{\varepsilon}^{-1}\nabla\tilde{\varepsilon}\cdot\left(-\nabla\tilde{\varphi}^- - \mathrm{i}\nabla\times(\tilde{\varphi}^-\hat{\boldsymbol{z}})\right) + \mathrm{i}\omega^2\mu_0\tilde{\varepsilon} = -\nabla^2\tilde{\varphi}^- + \mathrm{i}|\nabla\tilde{\varphi}^-|^2. \tag{2.62}$$

The measurable transceive phase $\varphi^{\pm} = \varphi^{+} - \tilde{\varphi}^{-}$ appears in the sum of (2.60) and (2.62),

$$\tilde{\varepsilon}^{-1}\nabla\tilde{\varepsilon}\cdot\left(\nabla\varphi^{\pm} - \mathrm{i}\nabla\times((\varphi^{+}+\tilde{\varphi^{-}})\hat{\boldsymbol{z}})\right) + 2\mathrm{i}\omega^{2}\mu_{0}\tilde{\varepsilon} = \nabla^{2}\varphi^{\pm} + \mathrm{i}\left(|\nabla\varphi^{+}|^{2} + |\nabla\tilde{\varphi}^{-}|^{2}\right). \tag{2.63}$$

In order to isolate the electric conductivity from the latter equation, it is convenient to consider only its real part. In particular, the real part of the first term of the left hand side can be expressed as

$$\mathrm{Re}\left(\tilde{\varepsilon}^{-1}\nabla\tilde{\varepsilon}\right)\cdot\nabla\varphi^{\pm} + \mathrm{Im}\left(\tilde{\varepsilon}^{-1}\nabla\tilde{\varepsilon}\right)\cdot\nabla\times((\varphi^{+}+\tilde{\varphi}^{-})\hat{\boldsymbol{z}}). \tag{2.64}$$

The term involving the sum of the phases is often negligible with respect to the other one. For example, it is negligible whenever the transceive phase assumption holds, since it entails $\varphi^{+} \simeq -\tilde{\varphi}^{-}$. Simulations endorse its negligibility also in some cases in which the transmit and the receive coils are different coils [110]. Finally, it must be noted that

$$\mathrm{Re}\left(\tilde{\varepsilon}^{-1}\nabla\tilde{\varepsilon}\right) = \mathrm{Re}\left(\nabla\log\tilde{\varepsilon}\right) = \nabla\log\sqrt{\varepsilon^{2}+\frac{\sigma^{2}}{\omega^{2}}} = \nabla\log\sqrt{\omega^{2}\varepsilon^{2}+\sigma^{2}}. \tag{2.65}$$

For the materials whose conductivity dominates the permittivity, namely $\sigma \gg \omega\varepsilon$, the latter implies

$$\mathrm{Re}\left(\tilde{\varepsilon}^{-1}\nabla\tilde{\varepsilon}\right) \simeq \sigma^{-1}\nabla\sigma. \tag{2.66}$$

In [70], it has been shown that phase-based stdEPT (2.15) introduces larger errors when $\omega\varepsilon \gg \sigma$. So, the last hypothesis, although quite strong, is very related to the ones of phase-base stdEPT and is verified by many tissues in operative clinical conditions (at Larmor frequencies below 128 MHz [83]). The ratio $\sigma/(\omega\varepsilon)$ is plotted against the frequency of the radiation for some biological materials in Fig. 2.8, which shows that the validity of the hypothesis depends on both the examined tissues and the Larmor frequency of the MRI scanner. The electric properties of the tissues have been estimated adopting the 4^{th} order Cole–Cole dispersive model [30] and using the measurements collected in the IT'IS Foundation database [112]. By virtue of all these considerations, the real part of (2.63) reads

$$\nabla\varphi^{\pm}\cdot\nabla\rho + \nabla^{2}\varphi^{\pm}\rho = 2\omega\mu_{0}, \tag{2.67}$$

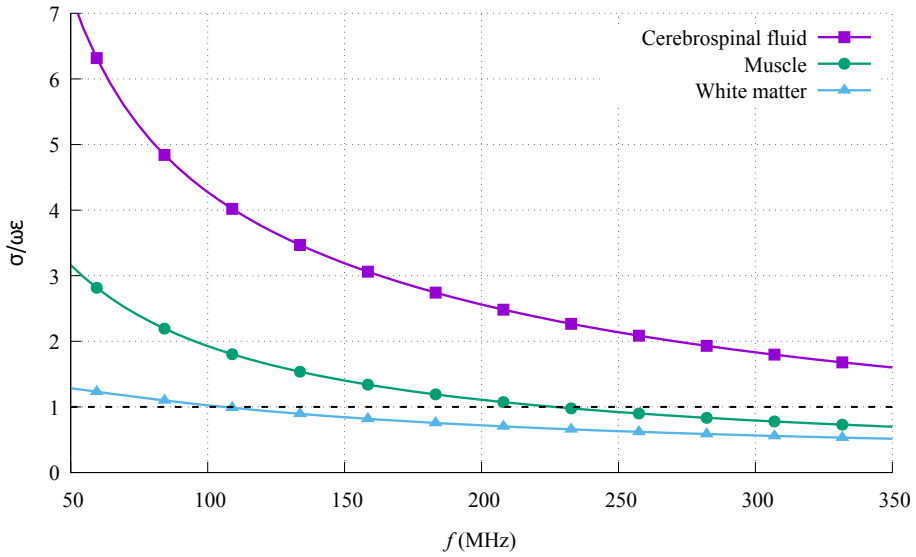

Fig. 2.8 The ratio $\sigma/(\omega\varepsilon)$ is plotted against frequency. A dashed black line highlights where the ratio is equal to one.

where the resistivity $\rho = \sigma^{-1}$ has been introduced in order make the equation linear with respect to the unknown. Unlike (2.52), phase-based crEPT (2.67) is a real-valued equation and so it is actually the classic convection-reaction equation. In conservative form, the latter equation reads

$$\nabla \cdot \left(\nabla \varphi^{\pm} \rho\right) = 2\omega\mu_0 \,. \tag{2.68}$$

Equation (2.67) and its conservative form (2.68) cannot be solved easily, because of the presence of a numerical instability in their discretisation with common numerical techniques, like the finite difference method or the finite volume method. The numerical instability arises from the absence of a diffusion term in the equation and the consequent infinite Péclet number [113]. For this reason, the issue cannot be solved simply reducing the mesh size. In order to recover the numerical stability, a small constant artificial diffusion, whose coefficient is denoted by λ, is introduced in the equation, which becomes [110]

$$\lambda \nabla^2 \rho + \nabla \cdot \left(\nabla \varphi^{\pm} \rho\right) = 2\omega\mu_0 \,. \tag{2.69}$$

The choice of the coefficient λ is a trade-off between spurious oscillations and a blurring effect in the recovered conductivity [110]. Actually, being (2.68) a real-valued conservative equation, some stable finite difference technique like the up-wind

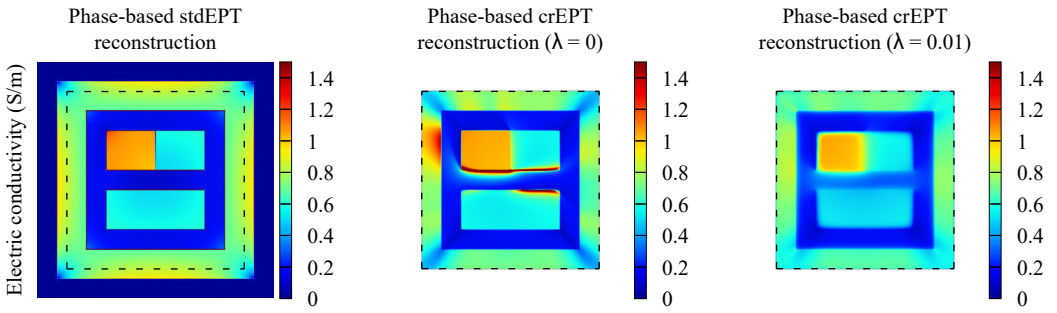

Fig. 2.9 The electric conductivity recovered by phase-based stdEPT and phase-based crEPT applied on the transceive phase are reported for a two-dimensional model problem. The same operative conditions of Fig. 2.7 are used. The crEPT technique is implemented with finite difference up-wind discretisation and artificial diffusion coefficient $\lambda = 0$ and 0.01. In order to force the Dirichlet boundary condition, equation (2.69) is solved in a restricted domain that lies inside the conductive cylinder. The dashed lines depict the restricted domain.

discretisation of the convective term, typical in computational fluid dynamics [114], can be adopted. In its easiest form, the up-wind discretisation reads

$$\left(\frac{\partial}{\partial x}(\beta_x^{\pm}\rho)\right)_{i,j,k} \simeq \begin{cases} \dfrac{(\beta_x^{\pm}\rho)_{i,j,k} - (\beta_x^{\pm}\rho)_{i-1,j,k}}{\Delta x}, & \text{if } (\beta_x^{\pm})_{i,j,k} > 0 \\ \dfrac{(\beta_x^{\pm}\rho)_{i+1,j,k} - (\beta_x^{\pm}\rho)_{i,j,k}}{\Delta x}, & \text{if } (\beta_x^{\pm})_{i,j,k} < 0 \end{cases} \tag{2.70}$$

and so on for the other directions, where the same notation introduced for (2.57) has been used and $\boldsymbol{\beta}^{\pm} = \nabla\varphi^{\pm}$. Although the up-wind discretisation is stable also when $\lambda = 0$, the presence of artificial diffusion helps in managing the input noise and should be considered.

The results obtained applying the phase-based stdEPT (2.20) and the phase-based crEPT (2.69) with finite difference up-wind discretisation are reported in Fig. 2.9, both in absence of artificial diffusion and with $\lambda = 0.01$. In both cases, it is possible to appreciate the smooth gradient between the electric conductivities of adjacent materials recovered by crEPT. In addition, the artificial diffusion reduces the artefacts due to the non-fulfilment of the method hypotheses. Since the conductivity of the air is null $\sigma = 0$, the resistivity ρ is not defined in air. Thus, a domain that lies inside the conductive cylinder has been used for crEPT. It is worth noting that in presence of artificial diffusion the problem depends continuously on the Dirichlet boundary conditions and the reconstruction is perturbed by wrong boundary conditions only around the boundary itself, making the method robust against errors in the boundary

conditions [110]. For example, with $\lambda = 0.01$, the same result of Fig. 2.9 is achieved assuming at the boundary the double of the actual conductivity.

2.5 Contrast source inversion EPT

The need of a MREPT technique that recovers the electric properties at tissues interfaces and that does not rely on many measurements from multiple transmitter coils leads to the development, in addition to crEPT, of various inverse methods [73, 74, 76, 115, 116]. Amongst them, the method based on the contrast source inversion (CSI) technique [74, 117] is particularly interesting because of its efficiency and flexibility. In addition, this method, denoted by the symbol csiEPT, has the intrinsic advantage of recovering the whole electromagnetic field generated by the transmit coil as well as the electric properties distribution [74, 118]. This fact makes the method appealing for dosimetric and safety applications (cfr. Section 3.1). In this section, csiEPT is briefly introduced in its original form, whereas the next chapter is completely devoted to a generalised and detailed analysis of the method.

2.5.1 Derivation

The csiEPT requires the knowledge of the electromagnetic field that the transmit coil generates in vacuum, the so-called incident field, in addition to the measurement of the transmit sensitivity in presence of the sample [74, 118]. If the design of the transmit coil is known, then an estimation of the incident field can be obtained by means of simulations, otherwise measurements must be used.

In a boundary-free domain, Maxwell's equations are analytically solved by convolution of the dyadic Green's functions with the forced current density [119]. In particular, the scattered field in presence of the examined body, namely the electromagnetic field generated by the body as a reaction to the incident field, can be expressed as [43]

$$\boldsymbol{E}^{\mathrm{s}}[\boldsymbol{w}](\boldsymbol{x}) = \int_{\mathbb{R}^3} \left(\left(\nabla\nabla + \kappa_0^2 \mathscr{I} \right) \psi(\boldsymbol{x}-\boldsymbol{y}) \right) \boldsymbol{w}(\boldsymbol{y}) \, \mathrm{d}\boldsymbol{y}, \tag{2.71}$$

and

$$\boldsymbol{H}^{\mathrm{s}}[\boldsymbol{w}](\boldsymbol{x}) = \int_{\mathbb{R}^3} \mathrm{i}\omega\varepsilon_0 \nabla\psi(\boldsymbol{x}-\boldsymbol{y}) \times \boldsymbol{w}(\boldsymbol{y}) \, \mathrm{d}\boldsymbol{y}, \tag{2.72}$$

where $\mathscr{I}$ is the identity operator, ψ is the fundamental solution of the Helmholtz equation with propagation coefficient $\kappa_0 = \omega\sqrt{\varepsilon_0\mu_0}$, and $\boldsymbol{w} = \chi(\boldsymbol{E}^{\mathrm{i}} + \boldsymbol{E}^{\mathrm{s}}[\boldsymbol{w}])$ is the so-called contrast source. The contrast $\chi = \tilde{\varepsilon}/\varepsilon_0 - 1$ is the actual unknown of csiEPT, whereas the contrast source plays the role of an auxiliary unknown. The superscripts i and s denote the incident and the scattered field, respectively. In three dimensions, the fundamental solution of the Helmholtz equation is

$$\psi(\boldsymbol{r}) = \frac{\mathrm{e}^{-\mathrm{i}\kappa_0|\boldsymbol{r}|}}{4\pi|\boldsymbol{r}|}. \tag{2.73}$$

When, instead, a two-dimensional problem is solved, the fundamental solution reads

$$\psi(\boldsymbol{r}) = -\frac{\mathrm{i}H_0^{(2)}(\kappa_0|\boldsymbol{r}|)}{4}, \tag{2.74}$$

being $H_0^{(2)}$ the zeroth order Hankel function of the second kind. It is worth noting that the support of the contrast function χ is the bounded volume occupied by the examined sample, so both integrals are well defined. The scattered field described by relations (2.71) and (2.72) can be interpreted physically as the electromagnetic field generated in air by an equivalent current density $\boldsymbol{J}^{\mathrm{s}} = \mathrm{i}\omega\varepsilon_0\boldsymbol{w}$ that takes the place of the scatterer, which is, instead, removed by the domain.

Two error functions for the contrast source $\boldsymbol{w}$ and the contrast χ can be determined based on relations (2.71) and (2.72). On the one hand, a data residual ρ that quantifies the difference between the scattered part of the measured transmit sensitivity $H^{+;\mathrm{s}}$ and the one estimated by a guess of the contrast source $\boldsymbol{w}$ is introduced as [74, 118]

$$\rho[\boldsymbol{w}] = H^{+;\mathrm{s}} - \frac{H_x^{\mathrm{s}}[\boldsymbol{w}] + \mathrm{i}H_y^{\mathrm{s}}[\boldsymbol{w}]}{2}. \tag{2.75}$$

On the other hand, a state residual $\boldsymbol{r}$ that measures the discrepancy between the actual incident electric field $\boldsymbol{E}^{\mathrm{i}}$ and the one estimated by a guess couple of contrast source $\boldsymbol{w}$ and contrast χ is defined as [74, 118]

$$\boldsymbol{r}[\boldsymbol{w},\chi] = \chi\boldsymbol{E}^{\mathrm{i}} - \boldsymbol{w} + \chi\boldsymbol{E}^{\mathrm{s}}[\boldsymbol{w}]. \tag{2.76}$$

Both the residuals are null for the actual values of $\boldsymbol{w}$ and χ. Therefore, csiEPT method recasts the inverse problem as the minimisation of the cost functional F that

combines the aforementioned residuals,

$$F[\boldsymbol{w},\chi] = \frac{1}{2\|H^{+;\mathrm{s}}\|^2}\|\rho[\boldsymbol{w}]\|^2 + \frac{1}{2\|\chi\boldsymbol{E}^{\mathrm{i}}\|^2}\|\boldsymbol{r}[\boldsymbol{w},\chi]\|^2, \tag{2.77}$$

where $\|\cdot\|$ denotes the L^2-norm. Thanks to the weights chosen in (2.77), the two residuals have the same relevance in the definition of the cost.

Despite the linear dependency of the scattered electromagnetic field on the contrast source $\boldsymbol{w}$, the minimisation of the cost functional (2.77) is not trivial because of the non-linearity that appears in the state residual. Here, the contrast χ multiplies the scattered electric field $\boldsymbol{E}^{\mathrm{s}}[\boldsymbol{w}]$, and the state residual weight involves the unknown contrast. In order to overcome this non-linearity, the numerical minimisation of (2.77) is performed by a two-step alternating conjugate gradient method [120]. Precisely, a guess of the contrast source and the contrast $(\boldsymbol{w}^{n-1},\chi^{n-1})$ is assumed to be known. In the first step, the contrast χ^{n-1} is kept fixed and the contrast source is updated to $\boldsymbol{w}^n$ by the conjugate gradient method with Polak-Ribière direction applied to the quadratic cost functional $F[\,\cdot\,,\chi^{n-1}]$. Then, in the second step, the contrast is updated to χ^n by applying the formula

$$\chi^n = \frac{\boldsymbol{w}^n\cdot(\boldsymbol{E}^{\mathrm{i}}+\boldsymbol{E}^{\mathrm{s}}[\boldsymbol{w}^n])^*}{|\boldsymbol{E}^{\mathrm{i}}+\boldsymbol{E}^{\mathrm{s}}[\boldsymbol{w}^n]|^2}, \tag{2.78}$$

namely minimising the L^2-norm of the state residual $\boldsymbol{r}[\boldsymbol{w}^n,\,\cdot\,]$, where the newly estimated contrast source $\boldsymbol{w}^n$ is kept fixed. The convenience of this approach relies also on the fact that the gradient of the cost functional with respect to the contrast source can be computed analytically making the implementation of the conjugate gradient easy. More details on the numerical minimisation are provided in the next chapter.

The electric properties recovered by csiEPT after 250 and 1000 iterative steps are reported in Fig. 2.10. The reconstructions are affected by numerical diffusion, which is reduced by increasing the number of iterative steps. The numerical diffusion can be exploited as the artificial diffusion in phase-based crEPT, so that in presence of noise only a limited number of iterative steps is performed, as the author has shown in [121]. Independently of the number of steps, a localised artefact can be identified in the estimated properties distribution. As already seen for deEPT and crEPT, the singular behaviour is located where the total electric field—*i.e.*, the sum

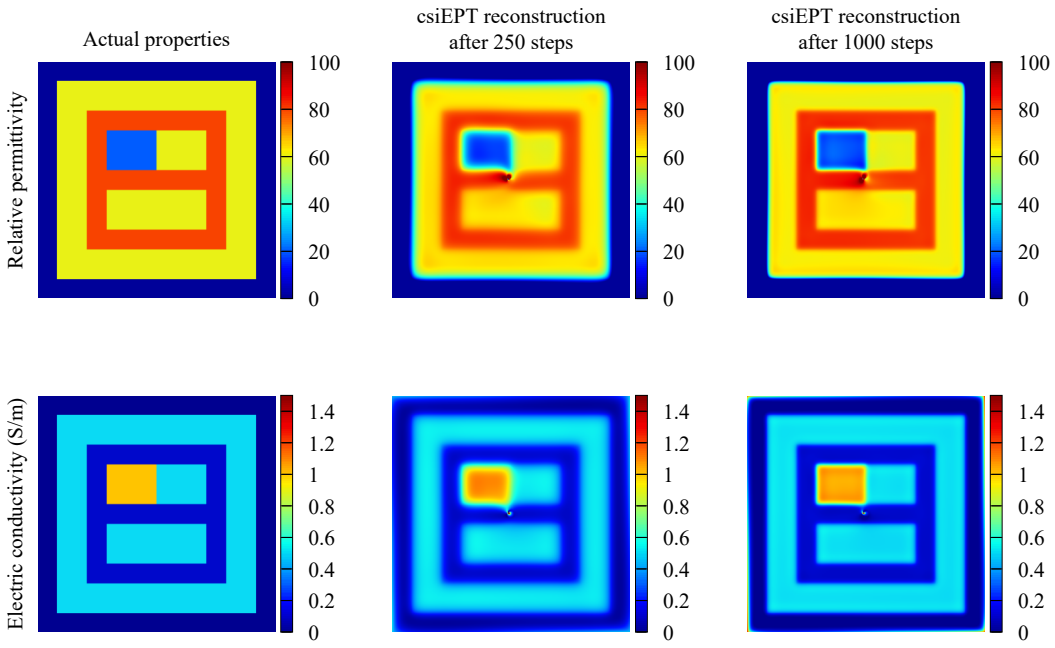

Fig. 2.10 The electric properties recovered by csiEPT are reported for a two-dimensional model problem. The same operative conditions of Fig. 2.7 are used. Both magnitude and phase of H^+ are assumed to be known exactly. The properties are displayed after 250 and 1000 iterative steps of the conjugate gradient method.

of the incident and the scattered fields—tends to zero. This fact happens because the total electric field intensity appears in the denominator of (2.78) and is strictly related to local noise propagation [121], as depicted in the next chapter. It is worth noting that csiEPT recovers the contrast source $\boldsymbol{w}$ as well as the contrast χ. Thus, at the end of the iterative procedure, the knowledge of the whole RF electromagnetic field is stored in the contrast source by means of relations (2.71) and (2.72).

2.6 Other methods

Despite its extension, the proposed overview is not exhaustive. Many other methods have been proposed in literature in the last few years, each one with strengths and weaknesses. A brief presentation of the most recent techniques is proposed below. Table 2.1 summarises the methods described above and the ones sketched out below.

2.6.1 Fourier transform-based EPT

Inspired by the integral approach of csiEPT, a global direct technique that exploits relation (2.72) has been proposed in [78]. In particular, the relation between the scattered part of the transmit sensitivity and the contrast source can be seen as the convolution product of a proper dyadic Green's function G^+ and the contrast source $\boldsymbol{w} = \chi \boldsymbol{E}$. Since the convolution product in spatial coordinates corresponds to the pointwise product in the Fourier domain, in a transverse section where it is reasonable to assume that E_x, E_y and H_z are null it is possible to write

$$H^{+;\mathrm{s}} = \mathscr{F}^{-1}\left\{\mathscr{F}\left\{G^+\right\}\mathscr{F}\left\{\chi E_z\right\}\right\}, \tag{2.79}$$

where $\mathscr{F}$ denotes the Fourier transform operator. The latter equation can be rearranged to find the following explicit expression for the contrast χ,

$$\chi = \frac{1}{E_z}\mathscr{F}^{-1}\left\{\frac{\mathscr{F}\left\{H^{+;\mathrm{s}}\right\}}{\mathscr{F}\left\{G^+\right\}}\right\}. \tag{2.80}$$

Whereas $H^{+;\mathrm{s}}$ can be obtained by MRI measurements, the electric field is unknown. In [78], it is assumed that the electric field can be approximated by the one generated

Table 2.1 List of the MREPT methods proposed in literature.

Name	(Section §)	Symbol	Taxonomy	References
Standard EPT	(2.1)	stdEPT	local direct	[58, 60, 70, 84]
Dual-excitation EPT	(2.2)	deEPT	local direct	[59, 95, 98]
Gradient-based EPT	(2.2)	gEPT	global direct	[99, 103, 107]
Local Maxwell tomography	(2.2)	LMT	local direct	[71, 105]
Zero echo-time EPT	(2.3)	zteEPT	local direct	[75]
Convection-reaction EPT	(2.4)	crEPT	global direct	[72, 110, 111]
Contrast source inversion EPT	(2.5)	csiEPT	global inverse	[74, 122]
Fourier transform-based EPT	(2.6)	—	global direct	[78]
Optimisation-based EPT	(2.6)	—	global inverse	[73, 76, 116]
Water content-based EPT	(2.6)	—	—	[123, 124]
Cauchy formula-based EPT	(2.6)	—	global direct	[77, 125]

by the same source in a homogeneous sample, like a phantom with known properties,

$$E_z \simeq \frac{1}{\chi_{\text{const}}} \mathscr{F}^{-1} \left\{ \frac{\mathscr{F}\left\{H^{+;\text{s}}_{\chi_{\text{const}}}\right\}}{\mathscr{F}\left\{G^{+}\right\}} \right\}. \tag{2.81}$$

By this way, the method leads to an estimation of the electric properties that makes no assumptions on the sample homogeneity.

2.6.2 Optimisation-based EPT

Many inverse methods, based on fitting a mathematical model to measured data by means of the optimisation theory, have been proposed for MREPT in addition to csiEPT [73, 76, 115, 116, 126]. A couple of methods have been developed starting from the phase-based stdEPT equation (2.15) [76, 116, 127]. In both cases, instead of estimating the Laplacian of the transmit phase, a cost functional like

$$F[\sigma] = \|\varphi^{+}[\sigma] - \varphi^{+}_{\text{meas}}\|^2 + \lambda\, \psi[\sigma] \tag{2.82}$$

is minimised. In (2.82), $\varphi^{+}[\sigma]$ is the solution of the Poisson equation $\nabla^2\varphi^{+} = \omega\mu_0\sigma$ with suitable boundary conditions, $\varphi^{+}_{\text{meas}}$ is the measured transmit phase, $\psi[\sigma]$ is a regularisation functional and λ is the corresponding regularisation factor. This approach has many advantages: it handles the noise globally and naturally thanks to regularisation; by choosing properly the regularisation functional, it is possible to adapt the method to *a priori* knowledge [76]; similarly, the cost functional can be changed and complicated by the introduction of masks and non-linear terms without changing the mathematical nature of the minimisation problem [116]. The generalised Helmholtz equation is considered in [73, 115], where the possibility to solve the MREPT problem by minimising iteratively a cost functional is proved mathematically. In [115], the properties are estimated by stdEPT first, then only at the interfaces between different tissues the solution is iteratively refined. On the other hand, in the paper of Ammari and colleagues [73] the properties in the whole domain are recovered iteratively by performing a constrained minimisation. Last but not least, the Global Maxwell Tomography (GMT) proposed in [126] minimises the discrepancy in the modelled and the measured magnitude of the transmit sensitivity only, which is achieved from the electric properties by solving the Maxwell equations.

2.6.3 Water content-based EPT

It has been shown that macroscopically the permittivity of biological tissues at RF is mainly determined by the volume ratio of water, whereas the capacitive effect of the cell membrane gets negligible [128]. In particular, the determination of the electric properties of biological tissues from the content of water is highly precise at the Larmor frequency of UHF MRI [124]. Since there exists an evident correlation between the water content of biological tissues and their spin-lattice relaxation time T_1, which can be expressed by an explicit formula whose coefficients are determined by the main field strength B_0 of the MRI scanner, it is possible to measure the volume ratio of water employing peculiar MRI sequences. Thus, once a model that relates the electric properties with the water content has been found, it is possible to perform MREPT by elaborating the water volume ratio maps [123, 124]. This approach was proposed for the first time by Farace and colleagues in 1997 [123], when the term MREPT had not yet been coined, in order to advance in the patient-specific hyperthermia treatment planning. Recently, it has been reintroduced in the context of electric properties tomography by Michel and colleagues [124], who discovered, by fitting measurements available in literature for the brain tissues, an exponential dependency of the conductivity from the water volume ratio and a parabolic relation for the permittivity. To the best of this author's knowledge, this is the only technique for MREPT that does not make use of Maxwell equations and transmit/receive sensitivity estimation, so it does not fit in the proposed taxonomy for MREPT methods.

2.6.4 Cauchy formula-based EPT

The application of advanced complex analysis concepts has led Palamodov to the definition of an analytical solution of the MREPT problem when the transmit sensitivity H^+ is completely known [77]. By performing dimensional analysis it is possible to find an incorrect equation in the derivation of the explicit relation [125]. The inaccuracy has been corrected by Nara and colleagues in [125], where accuracy and robustness to noise of the method are verified numerically. In order to get the analytical expression, the generalised Helmholtz equation is elaborated in complex domain until a so-called $\bar{\partial}$-problem (or DBAR problem) [129] is obtained. The $\bar{\partial}$-problem is solved by the Cauchy formula, which involves the integration of the

forcing term in the domain and of the unknown variable on the boundary, where an estimation of the electric properties must be provided [125]. The formula has been obtained under the assumption that $\partial H^+/\partial z = 0$, anyway the result can be iteratively corrected in order to account for the non-null longitudinal derivative [125].

Chapter 3

Contrast source inversion electric properties tomography

The contrast source inversion (CSI) technique was firstly proposed to solve inverse scattering problems for both acoustic and electromagnetic radiations [47]. Indeed, the physics of acoustic and electromagnetic scattering are very similar [43]. In particular, in the context of electromagnetic scattering, CSI has been formerly applied to microwave tomography for many purposes, *e.g.* in medicine [48], elasticity [130], geology [131], through-wall imaging [132], agronomy [49], forest product industry [133] and so on.

In microwave tomography, a radar system composed of a set of transmitter and receiver antennas is arranged outside the investigated sample. As a consequence, because of the shortage of measurable information, the inverse scattering problem is strongly ill-posed and the maximum achievable resolution is very limited [46, 51]. The introduction of the MRI scanner as a transmitter and receiver device that allows measuring RF magnetic fields inside a body can benefit the CSI technique, mainly with an increasing resolution. Clearly, since the MRI scanner employing B_1-mapping techniques [53–57] can measure only the transmit sensitivity of the RF coil, some variations on CSI have been introduced giving rise to csiEPT [117], briefly described in the previous chapter.

As shown in the previous chapter, csiEPT is just one among a plethora of MREPT methods, but it is the only one that recovers the electric properties as well as the whole electromagnetic field generated by the MRI transmit coil in the body [74, 118]. Thus,

despite its severe computational burden, which must be handled by coding an efficient parallel algorithm, csiEPT is particularly interesting for MRI safety [118, 134]. Indeed, the RF transmitter coil of MRI scanners can induce dangerous localised hot-spots of deposited power in the human body, with a risk increased in high field MRI because of the small wavelength of the radiation [135]. Thus, the local specific absorption rate (SAR) of the RF electromagnetic field should be estimated on-line in a patient-specific framework.

This chapter is devoted to an in-depth analysis of csiEPT. In Section 3.1, the convenience in MRI safety of csiEPT, as it has been described in the previous chapter, with respect to the other MREPT methods is shown. Then, Section 3.2 describes a general and abstract formalism for csiEPT that increases the applicability of the method to many physical situations. Finally, the possibility of neglecting the presence of a magnetic shield around the RF coil in the mathematical model inverted by the generalised csiEPT is analysed in Section 3.3 and the noise propagation in the method is studied in Section 3.4.

3.1 Local specific absorption rate estimation

The specific absorption rate (SAR) is the power deposited by the electromagnetic radiation in the tissues per unit of mass,

$$\mathrm{SAR} = \frac{\sigma |\boldsymbol{E}|^2}{2\delta}, \tag{3.1}$$

where σ is the effective conductivity, δ is the volumetric mass density and the phasor of the electric field $\boldsymbol{E}$ is defined with reference to the peak value of the field. The SAR is an element of concern in MRI, because it quantifies the electromagnetic power absorbed by the patient body. In particular, it appears explicitly in the bioheat transfer equation [136], which describes the temperature increase in the human body, the actual biological effect due to exposure to RF electromagnetic fields.

3.1.1 Legislative regulation

The relevant standard for the legal regulation of MRI equipment for medical diagnosis is IEC 60601-2-33 [137], which states, among other things, some safety requirements

about the SAR of the RF radiation. In particular, it must be ensured that the global SAR in the head of the patient is below $3.2\,\mathrm{W\,kg^{-1}}$ and the global SAR in the whole body is below $2.0\,\mathrm{W\,kg^{-1}}$ in normal operating mode or $4.0\,\mathrm{W\,kg^{-1}}$ in first level controlled operating mode. The normal operating mode is such that no physiological stress can be cause to the patient by the MRI scanner, whereas the first level controlled operating mode can cause some physiological stress to the patient, who needs to be monitored by medical supervision [137]. In order to comply with these limits, it is sufficient to check the ratio of the measurable absorbed RF power and patient mass. Usually, the manufacturer builds this monitoring in the MRI scanner. In addition, a constraint in the locally deposited power is stated: in normal operating mode, the local SAR averaged over 10 g of tissue have to be kept below $10\,\mathrm{W\,kg^{-1}}$ everywhere in the examined body but in extremities, where it may reach $20\,\mathrm{W\,kg^{-1}}$. All the mentioned values must be averaged on 6 minutes intervals. This constraint is the same as the one prescribed for occupational exposure by ICNIRP (International Commission on Non-Ionizing Radiation Protection) guidelines [138].

Since, unlike global SAR, local SAR cannot be measured directly during MRI examinations, the standard states to use theoretical models or experiments for its determination. Numerical simulations of the field generated by typical RF coils in presence of anatomical human models, like the ones provided by the Visible Human Project [139] and the Virtual Family [140, 141], suggest that compliance with the standard for global SAR implies compliance for local SAR when ordinary equipment with static field B_0 up to 3 T are employed. Thus, to monitor the global SAR is sufficient for many clinical applications. Nonetheless, an explicit verification of compliance with the local SAR limits must be performed in some particular cases:

i. When scanners with ultra-high field ($B_0 = 7\,\mathrm{T}$) are used, because localised peaks of the local SAR, referred to as hot-spots, may arise. This fact is due to the wavelength of the RF field in tissues being comparable with the body dimensions [142].

ii. When surface coils or multi-channel transmit coils for parallel transmission (pTX) are used, because strongly inhomogeneous fields may be generated independently of the wavelength [135].

In these situations, local SAR should be estimated by performing numerical simulations on patient-specific models. A strategy has been proposed to obtain quickly

patient-specific anatomical models [143], which can be used in accurate numerical simulations. Anyway, the electromagnetic simulations remain the bottleneck of such procedures because of their very high computational cost, which goes from tens of minutes up to some hours depending on the used numerical method and on the aimed accuracy. In order to avoid this step, nowadays a database of fields is produced by simulating numerically the RF coil in presence of different anatomical models at many positions. During the examination, a simulated model is assigned to the patient based on some traits—like age, height, weight, gender, and so on—then, by comparison of the selected simulation with the result of a preliminary B_1-mapping scan, the simulated local SAR is scaled to fit with the patient [144]. Such a database could be dynamically updated with simulations performed on the patient-specific anatomical models mentioned above [143]. However, this procedure cannot deal with exceptional cases, whose responses to the RF field is sensibly different from the simulated ones because of peculiar electric properties in some regions, *e.g.* the higher conductivity of some tumours.

3.1.2 Electric properties tomography

In order to perform a truly patient-specific estimation of local SAR, it would be very useful to know the actual distribution of the electric properties at the Larmor frequency inside the patient body. If just a segmentation is achieved [143], electric properties would be assigned from some database, like the one of IT'IS Foundation [112], which estimates the properties adopting the 4^{th} order Cole–Cole dispersive model [30]. The main drawback of this kind of database is that measurements are usually performed on freshly excised specimen, whose electric properties may be substantially different from the ones of the *in vivo* tissue. In addition, by relying on the average of a few measurements, the information about the statistical variation of the electric properties between different individuals or between different conditions of the same individual can hardly be obtained from databases. For this reason, MREPT would play a fundamental role in local SAR estimation.

The heterogeneous map of the electric properties estimated by any MREPT technique may be used in many ways in order to evaluate the local SAR distribution:

i. The most straightforward approach consists in using the knowledge of the electric properties distribution and of the RF coil design to simulate numerically

the transmitted electromagnetic field and obtain the local SAR accordingly. As stated above, this procedure is not feasible because of the too high computational cost. Anyway, it would provide a more reliable dynamical update of the database of maximum local SARs described above.

ii. The components of the magnetic field measured by the MRI scanner and used to perform MREPT can be reused for a fast estimation of the electric field generated by the RF coil, and as a consequence the local SAR. Precisely, Ampère's law in time-harmonic domain reads

$$\boldsymbol{E} = -\frac{\mathrm{i}}{\omega\tilde{\varepsilon}}\nabla\times\boldsymbol{H}\,. \tag{3.2}$$

Therefore, the electric field can be estimated locally employing the recovered electric properties $\tilde{\varepsilon}$ and approximating the magnetic field $\boldsymbol{H}$ by its measurable parts [58, 98, 101, 118, 145, 146]. Assuming that only the transmit sensitivity is measurable—in the previous chapter it has been shown that it is possible to approximately estimate also the receive sensitivity when using multi-channel transceive coils [98]—the magnetic field can be approximated neglecting all its components but $H^+ = (H_x + \mathrm{i}H_y)/2$. In Cartesian components, this results in

$$\boldsymbol{H} = \big(H^+ + (H^-)^*, \mathrm{i}\big((H^-)^* - H^+\big), H_z\big) \simeq \big(H^+, -\mathrm{i}H^+, 0\big)\,. \tag{3.3}$$

Thus, the electric field intensity can be estimated as

$$|\boldsymbol{E}|^2 \simeq \frac{1}{\omega^2|\tilde{\varepsilon}|^2}\left(2\left|\frac{\partial H^+}{\partial z}\right|^2 + \left|\mathrm{i}\frac{\partial H^+}{\partial x} + \frac{\partial H^+}{\partial y}\right|^2\right), \tag{3.4}$$

where the spatial derivatives must be approximated by a robust numerical algorithm, such as the three-dimensional Savitzky-Golay filter (cf. Section 2.1). As shown in the following example, neglecting H_z and, especially, H^- in the electric field estimation leads to a precise location of local SAR hot-spots, but strongly underestimates their intensity. The error committed in this way appears to increase with increasing Larmor frequency [145]. It would be possible to improve the electric field estimation by iteratively applying in alternation Ampère's law and Faraday's law as described in [147]. The iterations are proven to converge to the actual field if both H^+ and H^- are known, but it can

lead to satisfactory results also when only H^+ is measured [147]. However, to the best of this author's knowledge, this iterative approach has not been tested *in vivo* yet.

iii. As briefly described in the previous chapter and reworded in a general context in the next section, csiEPT recovers the contrast χ, from which the electric properties are deduced, as well as the contrast source $\boldsymbol{w}$, an auxiliary unknown that describes the scattered field with the relations (2.71) and (2.72). In this case, the particular MREPT implementation gives the additional information necessary for a full-wave estimation of the electric field, without neglecting any contribution,

$$\boldsymbol{E}[\boldsymbol{w}] = \boldsymbol{E}^{\mathrm{i}} + \boldsymbol{E}^{\mathrm{s}}[\boldsymbol{w}]\,. \tag{3.5}$$

3.1.3 Model problem

In order to check the capability of the methods to estimate the specific absorption rate, a realistic two-dimensional model problem is investigated. An unshielded 16-legs birdcage coil with a radius of 14 cm is simulated at 128 MHz, the Larmor frequency of protons corresponding to a static field $B_0 = 3\,\mathrm{T}$. Precisely, the mid-plane of the birdcage—parallel to $\hat{\boldsymbol{x}} \otimes \hat{\boldsymbol{y}}$—is approximated by the transverse magnetic (TM) assumption, namely H_x, H_y and E_z are assumed to be the only non-null components of the electromagnetic field. This allows handling the problem as a two-dimensional one in the plane, where the legs of the birdcage are modelled as line sources uniformly distributed on a circle. The current in each line source has the same intensity I as in the other lines and a time delay such that the positively rotating component of the magnetic field H^+ inside the birdcage is almost homogeneous and it is predominant over the negatively rotating one H^-. Numerically, assuming to number the line sources clockwise with the index $k = 1, \ldots, 16$, the current in the k-th source is

$$I_k = I\mathrm{e}^{\mathrm{i}k\pi/8}\,. \tag{3.6}$$

In order to simulate the electromagnetic field generated by the coil in presence of a head, the TM assumption is maintained and just a section of the head is considered. In particular, the anatomical human model Duke of the Virtual Family [140, 141] has been considered for this study and the section depicted in Fig. 3.1, where the corpus callosum can be easily recognised, has been selected. The electric properties are

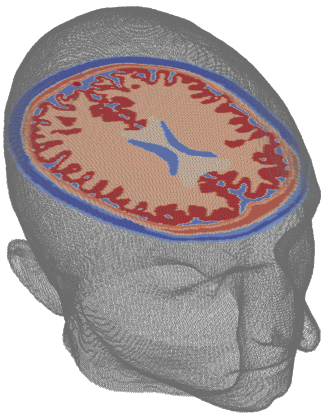

Fig. 3.1 Section of the head of the anatomical human model Duke of the Virtual Family [140, 141] that has been employed for the numerical simulations. In the section, each colour denotes a different biological tissue.

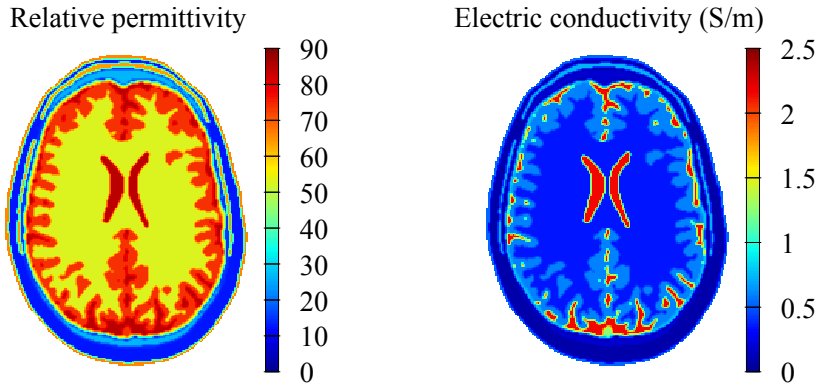

Fig. 3.2 Maps of the electric properties assigned to the section of the head taken into account.

assigned to each tissue in the section by applying the 4^{th} order Cole–Cole dispersive model [30] to the measurements collected in the IT'IS Foundation database [112]. The result is the heterogeneous distributions shown in Fig. 3.2. Whereas the incident electromagnetic field is known analytically, the scattered electric field is computed by solving numerically—employing the biconjugate gradient method and the fast Fourier transform (FFT) algorithm—the electric field integral equation (EFIE) (2.71) and, consequently, the scattered magnetic field is obtained by (2.72).

The electromagnetic field computed on a uniform Cartesian grid with 1 mm resolution is used as virtual measurement with no further post-processing in order to simulate noise-free measurements. In particular, the positively rotating component is assumed to be known exactly, neglecting the transceive phase assumption. Although such an ideal context is favourable for the MREPT techniques and does not stress

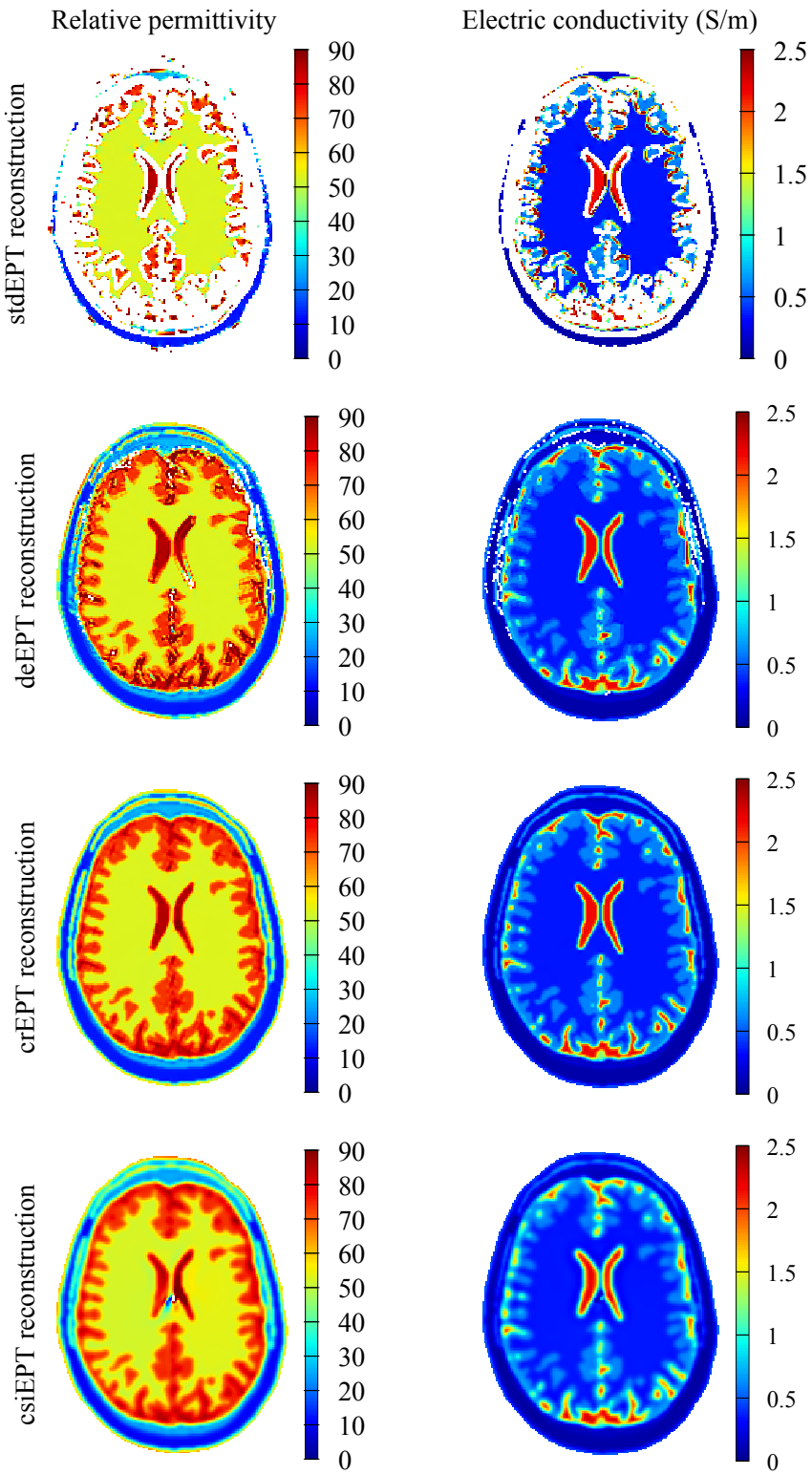

Fig. 3.3 Electric properties of the head section recovered by different MREPT techniques.

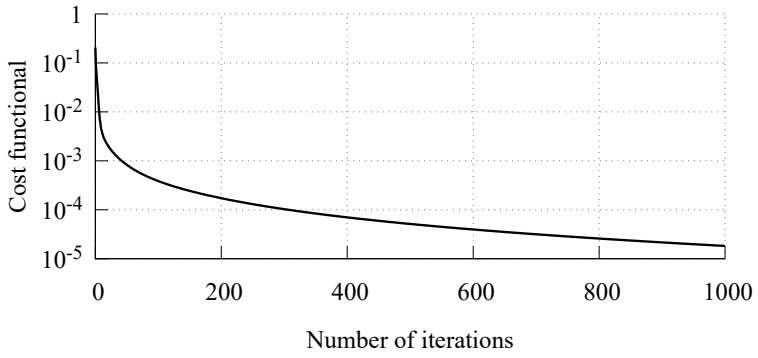

Fig. 3.4 Trend of the cost functional in csiEPT against the iterative step of the numerical minimisation procedure.

their capabilities, it highlights how good the estimation of the local SAR using different MREPT techniques could be. The techniques compared are stdEPT, deEPT, crEPT and csiEPT, as described in the previous chapter. Since the model problem is noise-free, the spatial derivatives of the magnetic field H^+ have been computed, for the techniques which need them, using second order centred finite difference schemes. For deEPT four independent fields are obtained by feeding just four line sources at each time such that four 4-legs birdcage coils are mimicked.

The electric properties recovered by the four methods are collected in Fig. 3.3. Reconstructed values that are negative or unrealistically high—over 200 for the relative permittivity and over $5\,\mathrm{S\,m^{-1}}$ for the conductivity—are discarded and not displayed in the pictures. Because of the many tissues' interfaces, primarily due to the brain gyri, the local homogeneity hypothesis—the basis of stdEPT—is unfulfilled in many points, in which, therefore, the recovered properties are discarded. Despite deEPT makes no assumptions on the homogeneity of the electric properties, also for this method a few negative or too high values are obtained at tissues' interfaces, where the Laplacian is not well defined and so it is difficult to be estimated. The error is further reduced by crEPT and csiEPT, which do not retrieve any anomalous value. Although crEPT, as deEPT, is based on the estimation of the Laplacian of H^+, the low-pass filtering effect of solving a PDE makes crEPT more robust than deEPT. In this particular case, crEPT does not seems to suffer from the low electric field intensity issue. In addition, no spurious oscillations are present in the distributions recovered by the finite difference method—the results reported in Fig. 3.3 have not been post-processed. On the other hand, the low electric field intensity issue appears in the csiEPT estimation of the properties, which is affected by numerical diffusion

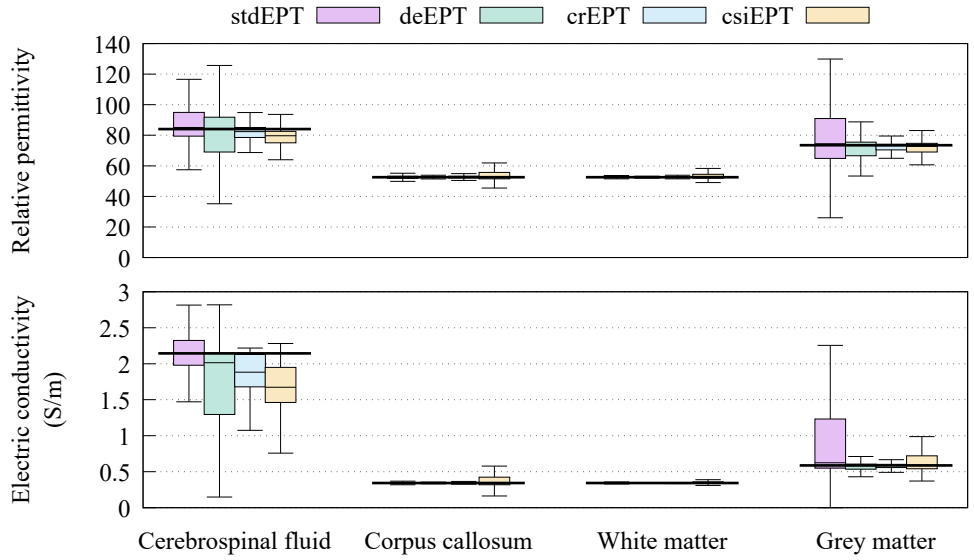

Fig. 3.5 Boxplots divided in quartiles of the estimated electric properties in the more significant tissues. The black horizontal lines indicate the actual values of the properties. The values out of the range 1 to 200 for the relative permittivity and $0\,\mathrm{S\,m^{-1}}$ to $5\,\mathrm{S\,m^{-1}}$ for the electric conductivity are outliers.

due to stopping the iterative procedure after 1000 steps. By increasing the maximum number of iterations, both the issues would be gradually reduced. Anyway, after 1000 steps the result is already satisfactory, so it has been used in the comparison. In addition, as can be seen in Fig. 3.4, the decreasing rate of the cost function after 1000 steps is very low with respect to the rate in the first iterations, suggesting that further small corrections in the estimated maps would require many additional steps.

A more quantitative analysis can be performed referring to the boxplots reported in Fig. 3.5. Boxplots are a very common and powerful tool to visualise statistical information on samples [148]. Each horizontal line in the boxes denotes a quartile of the underlying distribution and the whiskers go from the minimum to the maximum of the samples. In Fig. 3.5, the boxplots have been produced from the properties recovered pixel-by-pixel in the most significant tissues in the brain, whose distribution in the section is depicted in Fig. 3.6. It is worth noting that corpus callosum is made of the same material as the white matter, anyway the distinction between the two tissues is convenient for commenting on the data. Both properties of the cerebrospinal fluid are recovered with a sensible spatial variability by all the studied MREPT techniques. The apparent small variability of stdEPT estimation is because just the values recovered in the extended central x-shaped region are not treated

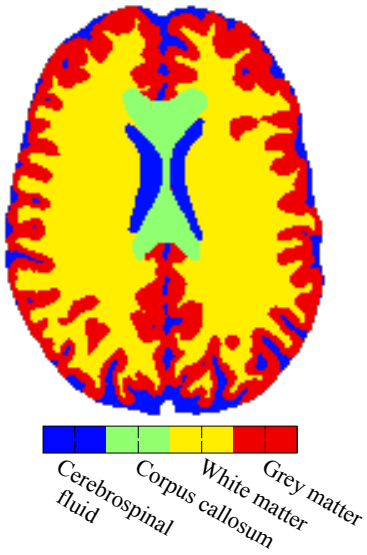

Fig. 3.6 Map of the most significant tissues in the considered section of the head.

as outliers. The variability in crEPT and csiEPT is mainly due to the numerical diffusion, which strongly affects the recovery of the small components of the cerebrospinal fluid. Corpus callosum and white matter constitute a very large region with few interfaces. Consequently, their properties are recovered very precisely and uniformly by all the techniques. An anomalous spatial variability can be appreciated just in the properties recovered by csiEPT in the corpus callosum. This happens because of the low electric field intensity issue. Indeed, the electric field has its minimum intensity in the corpus callosum. Finally, grey matter shows a sensible spatial variability, especially for stdEPT, because of the many gyri.

Fig. 3.5 is very important because it shows that for each method, when the outliers are not taken into account, the medians of the properties estimated in each tissue are very close to the actual properties of the tissue. Since the outliers, in particular the negative values, would lead to wrong and unphysical results when used in (3.1) and (3.4) for local SAR estimation, the distributions achieved by stdEPT and deEPT are post-processed assuming to have a segmentation of the domain. In practice it would be possible to segment the images produced by MRI during H^+ measurement. The post-processing is performed as follow. The median values estimated in each tissue neglecting the outliers are assigned to all the pixels of the tissue. In order to compute the median avoiding the ordering of the values, the iterative Weiszfeld's

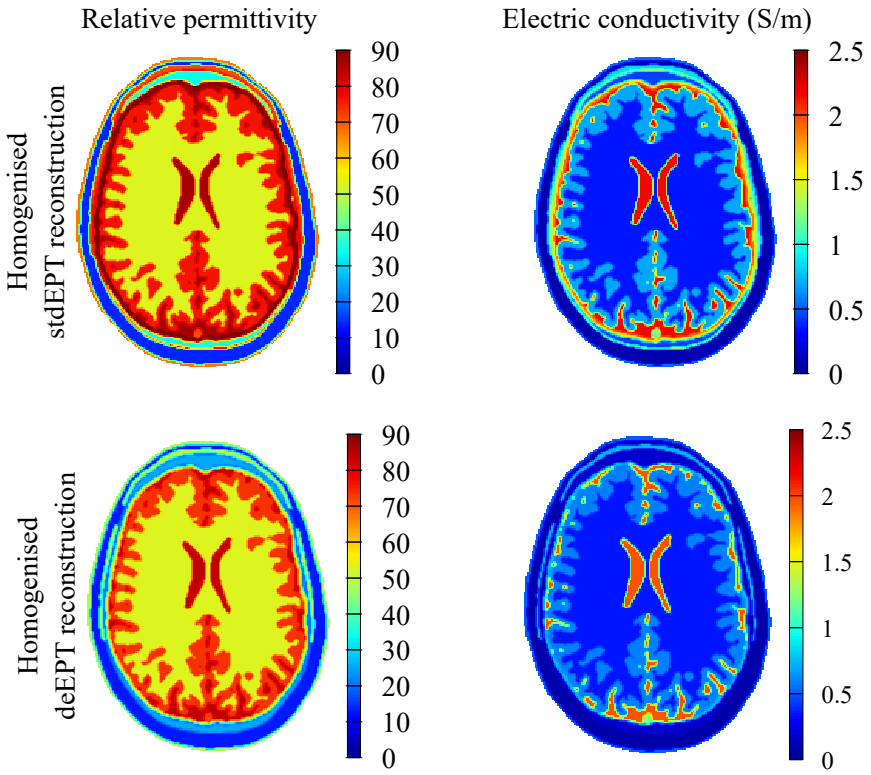

Fig. 3.7 Estimations of the electric properties distributions achieved by post-processing stdEPT and deEPTrecoveries. The medians of the properties estimated in each tissue neglecting the outliers are assigned to all the pixels that belong to the tissue.

algorithm has been used [149]. The homogenised distributions obtained in this way are reported in Fig. 3.7.

Finally, the local SAR is estimated based on the electric properties estimated by the MREPT techniques. For stdEPT and deEPT the post-processed reconstruction is used, whereas the distributions estimated by crEPT and csiEPT are directly used with no further post-processing. The electric field intensity is estimated by the first three techniques using (3.4), where the contribution of the unknown negatively rotating component is neglected. On the other hand, csiEPT estimates the electric field by (3.5) thanks to the auxiliary unknown contrast source $\boldsymbol{w}$, which implicitly considers the effects of the unknown components of the magnetic field. Thus, the non-averaged local SAR is estimated by (3.1), where the mass density is assumed constant and equal to the one of water, $\delta = 1000\,\mathrm{kg\,m^{-3}}$, for all the biological tissues. The same hypothesis on the mass density has been used in the actual local SAR computation. The actual local SAR due to the 16-legs birdcage coil and its four

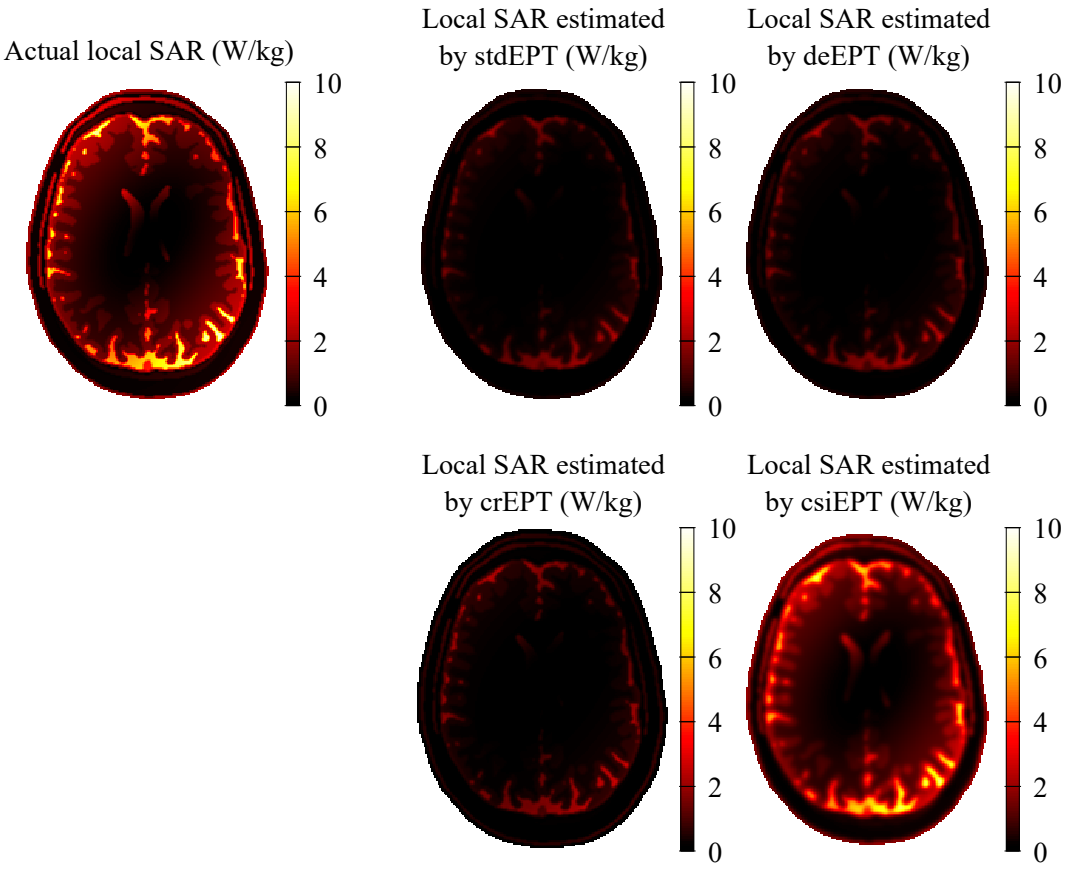

Fig. 3.8 The maps of the actual and estimated non-averaged local SAR due to a 16-legs birdcage coil of radius 14 cm rescaled such that the actual local SAR maximum is equal to $10\,\mathrm{W\,kg^{-1}}$.

estimated maps are collected in Fig. 3.8, where the results have been rescaled in order to have the maximum of the actual local SAR equal to $10\,\mathrm{W\,kg^{-1}}$. Only csiEPT allows approximating quantitatively the local SAR, whereas the other techniques strongly underestimates it because of neglecting the unknown components of the magnetic field. However, the hot-spots are precisely localised by all the techniques, confirming the results presented in [145] for stdEPT. It is worth noting that for special transmit coils that generate a non-negligible longitudinal component of the magnetic field H_z, the discrepancy between csiEPT and other MREPT techniques can further grow in terms of local SAR estimation capability.

The analysis performed in this section reproduces, with some variations and integrations, the one published by the author in [118]. The safety application is the main reason for an in-depth research about csiEPT.

3.2 Generalised formulation

Although csiEPT has been originally described in terms of integral equations for homogeneous boundary-free domains [74], the technique can be presented in a more general fashion, based on the functional point of view published by the author in [122], from which the original formulation can be deduced as a special case. A precise description of all the physical and mathematical objects involved in csiEPT is necessary in order to provide the generalised framework.

The electromagnetic field generated by the RF coil in absence of the examined body is called incident field and is denoted as $\{\boldsymbol{E}^{\mathrm{i}},\boldsymbol{H}^{\mathrm{i}}\}$. The background, namely the linear, non-magnetic ($\mu_{\mathrm{b}}=\mu_0$) and possibly heterogeneous medium of the incident field, is characterised by its electric conductivity σ_{b} and permittivity ε_{b}, which are conveniently gathered in the complex permittivity $\tilde{\varepsilon}_{\mathrm{b}}=\varepsilon_{\mathrm{b}}-\mathrm{i}\sigma_{\mathrm{b}}/\omega$, being ω the angular frequency of the radiation. The total field $\{\boldsymbol{E},\boldsymbol{H}\}$ is defined as the electromagnetic field generated by the same source of the incident field when the examined body is present and alters the background. The medium of the total field remains linear and non-magnetic, as it is a reasonable assumption for biological tissues [81], and it is characterised by the heterogeneous complex permittivity $\tilde{\varepsilon}=\varepsilon-\mathrm{i}\sigma/\omega$. Finally, the scattered field is the difference between the total and the incident fields $\{\boldsymbol{E}^{\mathrm{s}},\boldsymbol{H}^{\mathrm{s}}\}=\{\boldsymbol{E}-\boldsymbol{E}^{\mathrm{i}},\boldsymbol{H}-\boldsymbol{H}^{\mathrm{i}}\}$. It can be interpreted physically as the distortion to the incident field induced by the presence of the body.

Given the linearity of the media, the scattered field solves the system of equivalent Maxwell equations obtained by subtracting the equations for the total and the incident fields,

$$\begin{cases}\nabla\times\boldsymbol{E}^{\mathrm{s}}=-\mathrm{i}\omega\mu_0\boldsymbol{H}^{\mathrm{s}}\\ \nabla\times\boldsymbol{H}^{\mathrm{s}}=\mathrm{i}\omega\tilde{\varepsilon}_{\mathrm{b}}\boldsymbol{E}^{\mathrm{s}}+\boldsymbol{J}^{\mathrm{s}}\end{cases}\tag{3.7}$$

where $\boldsymbol{J}^{\mathrm{s}}=\mathrm{i}\omega\tilde{\varepsilon}_{\mathrm{b}}\boldsymbol{w}$ is an equivalent scattering current, $\boldsymbol{w}=\chi\boldsymbol{E}$ is the contrast source and χ is the contrast. In csiEPT, both the contrast source and the contrast are unknowns. In the most general anisotropic case, in which the complex permittivities are tensors, the contrast is the tensor $\chi=\tilde{\varepsilon}_{\mathrm{b}}^{-1}\tilde{\varepsilon}-I$, being I the identity matrix. However, only isotropic media are considered in the following, so the easiest definition $\chi=\tilde{\varepsilon}/\tilde{\varepsilon}_{\mathrm{b}}-1$ is used. Equations (3.7) are defined in a domain of interest $\Omega\subset\mathbb{R}^3$, on whose boundary $\partial\Omega$—or at infinity for unbounded Ω—reasonable boundary conditions are provided. It is worth noting that any forcing term that appears in

the equations of the incident field are also present in the equations of the total field. Thus, the only forcing term for the scattered field is the equivalent scattering current $\boldsymbol{J}^{\mathrm{s}}$ and any boundary condition is homogeneous. Under these hypothesis, the partial differential equation (PDE) problem is solved by one and only one couple $\{\boldsymbol{E}^{\mathrm{s}}, \boldsymbol{H}^{\mathrm{s}}\}$, which depends continuously on $\boldsymbol{J}^{\mathrm{s}}$, or, by composition, on the contrast source $\boldsymbol{w}$ [32, 119]. In more technical words, there exists a couple of linear and bounded operators $\mathscr{S}_{\mathrm{e}}$ and $\mathscr{S}_{\mathrm{h}}$ such that

$$\boldsymbol{E}^{\mathrm{s}} = \mathscr{S}_{\mathrm{e}} \boldsymbol{w}, \qquad \boldsymbol{H}^{\mathrm{s}} = \mathscr{S}_{\mathrm{h}} \boldsymbol{w}. \tag{3.8}$$

3.2.1 Cost functional

In order to define a cost functional whose minimum solves the inverse problem, a couple of error functions for the contrast source $\boldsymbol{w}$ and the contrast χ must be identified.

In the following it is assumed that the transmit sensitivity $B_1^+ = \mu_0 H^+$ is completely measured by the MRI scanner—the magnitude mapped by any B_1-mapping technique and the phase retrieved by the transceive phase assumption or some other technique (cfr. Chapter 2). Thus, a data residual ρ can be introduced to quantify the difference between the measured transmit sensitivity and a guess of the contrast source $\boldsymbol{w}$. In order to write the data residual with a convenient notation, a couple of operators should be introduced. First, the positively rotating part operator $\mathscr{P}$ receives as input a vector field $\boldsymbol{u}$ and returns the scalar field

$$\mathscr{P}\boldsymbol{u} = \frac{u_x + \mathrm{i}u_y}{2}. \tag{3.9}$$

Clearly, returning a linear combination of the Cartesian components of the input field, $\mathscr{P}$ is a linear and bounded operator. Next, an observation operator $\mathscr{O}$ that models mathematically the measurement of the magnetic field starting from its actual distribution is needed in order to make the discrete measured sample and the continuous guess map comparable. Different implementations of $\mathscr{O}$ can be suggested:

i. If the transmit sensitivity is measured in an ordered collection of N points $(\boldsymbol{x}_i)_{i=1}^N$, the measurement can be modelled as the evaluation of the generic

input scalar field u in the points

$$\mathscr{O}u = \big(u(\boldsymbol{x}_i)\big)_{i=1}^{N}. \tag{3.10}$$

From a mathematical point of view, this definition is critical when the input field u belongs to some Lebesgue or Sobolev space, because in this case the evaluation of u in a point is not well defined. The issue is particularly evident when u has a jump discontinuity.

ii. If the mean value of the transmit sensitivity is measured in an ordered collection of N regions (the voxels) $(V_i)_{i=1}^{N}$, the measurement of the generic input scalar field u can be modelled as

$$\mathscr{O}u = \left(\frac{1}{|V_i|}\int_{V_i} u(\boldsymbol{x})\mathrm{d}\boldsymbol{x}\right)_{i=1}^{N}, \tag{3.11}$$

where $|V_i|$ is the volume of V_i. This definition solves the previous mathematical issue and, despite looking awkward, it models quite precisely the measurement operation of MRI scanners.

Both definitions (3.10) and (3.11) lead to a linear and bounded observation operator. Finally, the data residual is

$$\rho[\boldsymbol{w}] = B_1^{+;\mathrm{s}}/\mu_0 - \mathscr{O}\mathscr{S}_{\mathrm{h}}^{+}\boldsymbol{w}, \tag{3.12}$$

where the scattered part of the transmit sensitivity $B_1^{+;\mathrm{s}}$ and the composed operator $\mathscr{S}_{\mathrm{h}}^{+} = \mathscr{P}\mathscr{S}_{\mathrm{h}}$ have been introduced.

On the other hand, the definition of the contrast source

$$\boldsymbol{w} = \chi\boldsymbol{E} = \chi\boldsymbol{E}^{\mathrm{i}} + \chi\boldsymbol{E}^{\mathrm{s}} = \chi\boldsymbol{E}^{\mathrm{i}} + \chi\mathscr{S}_{\mathrm{e}}\boldsymbol{w}, \tag{3.13}$$

leads naturally to the state residual $\boldsymbol{r}$, which estimates the difference between the actual incident electric field $\boldsymbol{E}^{\mathrm{i}}$ and the guess couple of contrast source and contrast,

$$\boldsymbol{r}[\boldsymbol{w},\chi] = \chi\boldsymbol{E}^{\mathrm{i}} - \boldsymbol{w} + \chi\mathscr{S}_{\mathrm{e}}\boldsymbol{w}. \tag{3.14}$$

The incident electromagnetic field is an input of csiEPT for the computation of both $B_1^{+;\mathrm{s}}$ and $\boldsymbol{E}^{\mathrm{i}}$. If the RF coil design is known, then an accurate numerical simulation of

the coil in free space can estimate the incident field. Otherwise, it can be measured once and for all during the coil characterisation. If the incident field is known by means of measurements, the result can be interpolated in order to obtain a continuous map of $\boldsymbol{E}^{\mathrm{i}}$, otherwise another observation operator must be introduced for the state residual. In the following, the knowledge of a map of $\boldsymbol{E}^{\mathrm{i}}$ is assumed.

The two residuals are combined in the definition of the cost functional F that must be minimised in order to obtain the electric properties distributions [122],

$$F[\boldsymbol{w},\chi] = \frac{\eta_{\mathrm{d}}}{2}\|\rho[\boldsymbol{w}]\|_{\mathbb{D}}^2 + \frac{\eta_{\mathrm{s}}[\chi]}{2}\|\boldsymbol{r}[\boldsymbol{w},\chi]\|_{\mathbb{S}}^2 . \tag{3.15}$$

In the latter equation, $\eta_{\mathrm{d}} = \|B_1^{+;\mathrm{s}}/\mu_0\|_{\mathbb{D}}^{-2}$ and $\eta_{\mathrm{s}}[\chi] = \|\chi\boldsymbol{E}^{\mathrm{i}}\|_{\mathbb{S}}^{-2}$ are the weights that keep the two errors at the same relevance in the overall cost. The symbols $\|\cdot\|_{\mathbb{D}}$ and $\|\cdot\|_{\mathbb{S}}$ denote the norm of the Banach spaces $\mathbb{D}$, the discrete space of the data, and $\mathbb{S}$, the continuous space of the state, respectively. In the following computations, for sake of simplicity, it is assumed that both $\mathbb{D}$ and $\mathbb{S}$ are Hilbert spaces with inner products $(\cdot|\cdot)_{\mathbb{D}}$ and $(\cdot|\cdot)_{\mathbb{S}}$, respectively.

3.2.2 Numerical minimisation

As it is common use in CSI tradition, the cost functional F is minimised numerically by a two-step alternating conjugate gradient method [47, 74, 120]. The two-step approach allows to deal easily with the non-linearity of the problem due to the presence of the product between χ and $\boldsymbol{w}$ in the state residual and to the dependence on χ of the weight η_{s}. This numerical procedure has been criticised and a couple of alternative algorithms have been proposed [150], anyway the method is very common and it has been proven robust in many experimental contexts [48, 49, 131–133].

Starting from an initial guess couple $(\boldsymbol{w}^n, \chi^n)$—the result of the n-th iterative step—, the contrast source is updated first keeping the contrast map fixed. The update is done using the conjugate gradient iterative scheme

$$\boldsymbol{w}^{n+1} = \boldsymbol{w}^n + \alpha^n \boldsymbol{v}^n , \tag{3.16}$$

where α^n is the optimal real-valued step length and $\boldsymbol{v}^n$ is the Polak-Ribière direction [151], which is defined iteratively as

$$\begin{cases} \boldsymbol{v}^0 = \boldsymbol{0} \\ \boldsymbol{v}^n = \boldsymbol{g}^n + \dfrac{\left(\boldsymbol{g}^n | \boldsymbol{g}^n - \boldsymbol{g}^{n-1}\right)_{\mathbb{S}}}{\|\boldsymbol{g}^{n-1}\|_{\mathbb{S}}^2} \boldsymbol{v}^{n-1}, \quad \text{if } n > 0 \end{cases} \tag{3.17}$$

In (3.17), $\boldsymbol{g}^n$ is the gradient of the cost functional F with respect to the contrast source $\boldsymbol{w}$ evaluated in the couple $(\boldsymbol{w}^n, \chi^n)$. Since $\mathbb{S}$ is assumed to be an Hilbert space, the gradient $\boldsymbol{g}^n$ is the Riesz representation of the Fréchet differential $\mathrm{d}_{\boldsymbol{w}} F|_{(\boldsymbol{w}^n, \chi^n)}$, so it can be computed using the definition of the Gâteaux derivative as follows.

For simplicity of notation, the quantities $\eta_{\mathrm{s}}^n = \eta_{\mathrm{s}}[\chi^n]$, $\rho^n = \rho[\boldsymbol{w}^n]$ and $\boldsymbol{r}^n = \boldsymbol{r}[\boldsymbol{w}^n, \chi^n]$ are introduced. For any generic field $\boldsymbol{u} \in \mathbb{S}$,

$$\begin{gathered} (\boldsymbol{g}^n | \boldsymbol{u})_{\mathbb{S}} = \mathrm{d}_{\boldsymbol{w}} F|_{(\boldsymbol{w}^n, \chi^n)} [\boldsymbol{u}] = \lim_{h \to 0} \frac{F[\boldsymbol{w}^n + h\boldsymbol{u}, \chi^n] - F[\boldsymbol{w}^n, \chi^n]}{h} = \\ \frac{\eta_{\mathrm{d}}}{2} \lim_{h \to 0} \frac{\|\rho[\boldsymbol{w}^n + h\boldsymbol{u}]\|_{\mathbb{D}}^2 - \|\rho^n\|_{\mathbb{D}}^2}{h} + \frac{\eta_{\mathrm{s}}^n}{2} \lim_{h \to 0} \frac{\|\boldsymbol{r}[\boldsymbol{w}^n + h\boldsymbol{u}, \chi^n]\|_{\mathbb{S}}^2 - \|\boldsymbol{r}^n\|_{\mathbb{S}}^2}{h}. \end{gathered} \tag{3.18}$$

The first addendum of the latter equation reads

$$\frac{\eta_{\mathrm{d}}}{2} \lim_{h \to 0} \frac{h^2 \left\| \mathscr{O} \mathscr{S}_{\mathrm{h}}^{+} \boldsymbol{u} \right\|_{\mathbb{D}}^2 - 2h \left(\rho^n | \mathscr{O} \mathscr{S}_{\mathrm{h}}^{+} \boldsymbol{u}\right)_{\mathbb{D}}}{h} = -\eta_{\mathrm{d}} \left(\mathscr{S}_{\mathrm{h}}^{+;\star} \mathscr{O}^{\star} \rho^n | \boldsymbol{u}\right)_{\mathbb{S}}, \tag{3.19}$$

whereas the second addendum is

$$\frac{\eta_{\mathrm{s}}^n}{2} \lim_{h \to 0} \frac{h^2 \|\chi^n \mathscr{S}_{\mathrm{e}} \boldsymbol{u} - \boldsymbol{u}\|_{\mathbb{S}}^2 + 2h \left(\boldsymbol{r}^n | \chi^n \mathscr{S}_{\mathrm{e}} \boldsymbol{u} - \boldsymbol{u}\right)_{\mathbb{S}}}{h} = \eta_{\mathrm{s}}^n \left(\mathscr{S}_{\mathrm{e}}^{\star} [\chi^{n,*} \boldsymbol{r}^n] - \boldsymbol{r}^n | \boldsymbol{u}\right)_{\mathbb{S}}, \tag{3.20}$$

where the superscript star denotes the adjoint operators (cfr. Appendix B) and the asterisk the complex conjugation. Given the generality of $\boldsymbol{u} \in \mathbb{S}$, it results that

$$\boldsymbol{g}^n = -\eta_{\mathrm{d}} \mathscr{S}_{\mathrm{h}}^{+;\star} \mathscr{O}^{\star} \rho^n + \eta_{\mathrm{s}}^n \left(\mathscr{S}_{\mathrm{e}}^{\star} [\chi^{n,*} \boldsymbol{r}^n] - \boldsymbol{r}^n\right). \tag{3.21}$$

Similarly, also the optimal step length α^n can be computed analytically in the general framework. Once the update direction $\boldsymbol{v}^n$ is known, the step length α^n is

chosen by solving the line minimisation problem

$$\min_{\alpha\in\mathbb{R}} F[\boldsymbol{w}^n + \alpha\boldsymbol{v}^n, \chi^n], \tag{3.22}$$

which, being unconstrained, is solved by the solution of the Euler equation

$$\frac{\mathrm{d}}{\mathrm{d}\alpha} F[\boldsymbol{w}^n + \alpha\boldsymbol{v}^n, \chi^n]\bigg|_{\alpha=\alpha^n} = 0\,. \tag{3.23}$$

The left hand side of the latter equation can be elaborated by the chain-rule to obtain

$$\mathrm{d}_{\boldsymbol{w}} F|_{(\boldsymbol{w}^n+\alpha^n\boldsymbol{v}^n,\chi^n)}[\boldsymbol{v}^n] = (\boldsymbol{g}^n|\boldsymbol{v}^n)_{\mathbb{S}} + \alpha^n\left(\eta_{\mathrm{d}}\|\mathscr{O}\mathscr{S}_{\mathrm{h}}^{+}\boldsymbol{v}^n\|_{\mathbb{D}}^2 + \eta_{\mathrm{s}}^n\|\chi^n\mathscr{S}_{\mathrm{e}}\boldsymbol{v}^n - \boldsymbol{v}^n\|_{\mathbb{S}}^2\right) = 0\,, \tag{3.24}$$

and so

$$\alpha^n = \frac{-(\boldsymbol{g}^n|\boldsymbol{v}^n)_{\mathbb{S}}}{\eta_{\mathrm{d}}\|\mathscr{O}\mathscr{S}_{\mathrm{h}}^{+}\boldsymbol{v}^n\|_{\mathbb{D}}^2 + \eta_{\mathrm{s}}^n\|\chi^n\mathscr{S}_{\mathrm{e}}\boldsymbol{v}^n - \boldsymbol{v}^n\|_{\mathbb{S}}^2}\,. \tag{3.25}$$

It is worth noting that both the gradient $\boldsymbol{g}^n$ and the optimal step length α^n have been computed analytically by just assuming that the operators are linear and bounded. The actual implementation or the numerical discretisation of the operators does not change the results, which are completely general.

The application of the contrast source update step leads to the intermediate guess couple $(\boldsymbol{w}^{n+1}, \chi^n)$, in which the contrast χ^n is updated keeping the contrast source fixed. The contrast affects the cost functional F only by means of the state residual, so to minimise the cost functional with respect to the contrast is equivalent to minimise the weighted state error

$$F_{\mathrm{s}}[\boldsymbol{w}^{n+1}, \chi] = \frac{\|\boldsymbol{r}[\boldsymbol{w}^{n+1}, \chi]\|_{\mathbb{S}}^2}{2\|\chi\boldsymbol{E}^{\mathrm{i}}\|_{\mathbb{S}}^2}\,. \tag{3.26}$$

This problem is not trivial because of the non-linearity due to the presence of the contrast both in numerator and in denominator. Usually, in order to deal analytically with this minimisation, the weight is assumed constant and just the norm of the state residual $\|\boldsymbol{r}[\boldsymbol{w}^{n+1}, \chi]\|_{\mathbb{S}}^2$ is minimised [47, 120]. This simplification is criticised in [150] because it leads to a solution that is not the actual minimiser of F. Anyway, this trick prevents the procedure from converging towards degenerate solutions [150], justifying its spread in many CSI applications. Since the simplified functional is convex, the contrast update can be performed analytically by solving the Euler

equation

$$\begin{aligned}
\lim_{h\to 0}\frac{\|\boldsymbol{r}[\boldsymbol{w}^{n+1},\chi^{n+1}+hu]\|_{\mathbb{S}}^2-\|\boldsymbol{r}[\boldsymbol{w}^{n+1},\chi^{n+1}]\|_{\mathbb{S}}^2}{h}=\\
\lim_{h\to 0}\frac{h^2\left\|u\left(\boldsymbol{E}^{\mathrm{i}}+\mathscr{S}_{\mathrm{e}}\boldsymbol{w}^{n+1}\right)\right\|_{\mathbb{S}}^2+2h\left(\boldsymbol{r}[\boldsymbol{w}^{n+1},\chi^{n+1}]|u\left(\boldsymbol{E}^{\mathrm{i}}+\mathscr{S}_{\mathrm{e}}\boldsymbol{w}\right)\right)_{\mathbb{S}}}{h}=\\
2\left(\boldsymbol{r}[\boldsymbol{w}^{n+1},\chi^{n+1}]|u\left(\boldsymbol{E}^{\mathrm{i}}+\mathscr{S}_{\mathrm{e}}\boldsymbol{w}\right)\right)_{\mathbb{S}}=\\
2\left(\left|\boldsymbol{E}^{\mathrm{i}}+\mathscr{S}_{\mathrm{e}}\boldsymbol{w}^{n+1}\right|^2\chi^{n+1}-\boldsymbol{w}^{n+1}\cdot\left(\boldsymbol{E}^{\mathrm{i}}+\mathscr{S}_{\mathrm{e}}\boldsymbol{w}^{n+1}\right)^*|u\right)_{\mathbb{X}}=0,
\end{aligned}\tag{3.27}$$

for any scalar field $u\in\mathbb{X}$, being $\mathbb{X}$ the continuous space of the contrast. Given the generality of the test function $u\in\mathbb{X}$, the latter equation is solved by

$$\chi^{n+1}=\frac{\boldsymbol{w}^{n+1}\cdot\left(\boldsymbol{E}^{\mathrm{i}}+\mathscr{S}_{\mathrm{e}}\boldsymbol{w}^{n+1}\right)^*}{\left|\boldsymbol{E}^{\mathrm{i}}+\mathscr{S}_{\mathrm{e}}\boldsymbol{w}^{n+1}\right|^2},\tag{3.28}$$

where $\boldsymbol{E}[\boldsymbol{w}^{n+1}]=\boldsymbol{E}^{\mathrm{i}}+\mathscr{S}_{\mathrm{e}}\boldsymbol{w}^{n+1}$ is the current estimation of the total electric field. As before, also in this case, the update has been performed analytically with no assumptions about the actual implementation or the numerical discretisation of the linear and bounded operators that appear in the cost function definition.

The iterative procedure that has been described performs an unconstrained minimisation, but it can be easily adapted to respect some *a priori* knowledge modelled as convex constraint for the contrast. Precisely, if $C\subset\mathbb{X}$ is a convex subset of $\mathbb{X}$ and the contrast is constrained to belong to C, it is sufficient to project the result of each contrast update (3.28) into C to converge towards the constrained solution [120]. A typical example of convex constraint is the positivity and negativity of the real and imaginary parts of χ, respectively, due to the positivity of the physical properties ε and σ. To enforce this constraint by projection consists in setting, after the contrast update, the real or the imaginary part of χ equal to zero in the regions where they are negative or positive, respectively. In addition, since the MRI scanner cannot measure any signal in air, it is possible to identify a region of null contrast by elaborating the measured data. The imposition $\chi=0$ in that region is a convex constraint that can be enforced by setting the contrast in that region equal to zero after the contrast update.

In order to make the iterative procedure start, an initial guess is done on the contrast source, which is selected by back propagation [120], namely $\boldsymbol{w}^0$ is the

contrast sources that minimises the data residual norm $\|\rho[\boldsymbol{w}]\|_{\mathbb{D}}^2$,

$$\boldsymbol{w}^0 = \frac{\left\|\mathscr{S}_{\mathrm{h}}^{+;\star}\mathscr{O}^{\star}B_1^{+;\mathrm{s}}\right\|_{\mathbb{S}}^2}{\left\|\mathscr{O}\mathscr{S}_{\mathrm{h}}^{+}\mathscr{S}_{\mathrm{h}}^{+;\star}\mathscr{O}^{\star}B_1^{+;\mathrm{s}}\right\|_{\mathbb{D}}^2}\mathscr{S}_{\mathrm{h}}^{+;\star}\mathscr{O}^{\star}B_1^{+;\mathrm{s}}/\mu_0\,. \tag{3.29}$$

By applying (3.28), the initial contrast $\boldsymbol{\chi}^0$ is then obtained.

Being based on a functional point of view, the proposed formalism is completely general and makes no hypothesis on the homogeneity of the background—$\tilde{\varepsilon}_{\mathrm{b}}$ may be heterogeneous—or the adoption of particular boundary conditions. In addition, the whole procedure has been described with no assumptions on the numerical implementation of the resolvent operators $\mathscr{S}_{\mathrm{e}}$ and $\mathscr{S}_{\mathrm{h}}$, which can rely on semi-analytical solutions [120], on the finite difference method [132], on the finite element method [152], on the wavelet transform [153] and so on in order to model the scattered electromagnetic field in the most precise and efficient way.

3.2.3 Implementation for the boundary-free domain

In the generalised framework described above, to implement the csiEPT technique for a particular situation means to define properly the linear and bounded resolvent operators $\mathscr{S}_{\mathrm{e}}$ and $\mathscr{S}_{\mathrm{h}}$ and to compute their adjoint operators $\mathscr{S}_{\mathrm{e}}^{\star}$ and $\mathscr{S}_{\mathrm{h}}^{\star}$.

In this section, the generalised framework is specialised for a homogeneous and boundary-free domain as the one originally considered in [74] and presented in the previous chapter. In this way, the original proposal of csiEPT is recovered as a particular case of the generalised formulation presented in this thesis [122]. In such a domain, Maxwell equations are solved by the convolution integral of the dyadic Green's functions with the imposed current density [119]. Thus, the resolvent operators for the scattered electromagnetic field are for any input $\boldsymbol{w} \in \mathbb{S}$ [43]

$$\left(\mathscr{S}_{\mathrm{e}}\boldsymbol{w}\right)(\boldsymbol{x}) = \int_{\mathbb{R}^3}\left(\left(\nabla\nabla + \kappa_{\mathrm{b}}^2\mathscr{I}\right)\psi(\boldsymbol{x}-\boldsymbol{y})\right)\boldsymbol{w}(\boldsymbol{y})\,\mathrm{d}\boldsymbol{y}\,, \tag{3.30}$$

and

$$\left(\mathscr{S}_{\mathrm{h}}\boldsymbol{w}\right)(\boldsymbol{x}) = \int_{\mathbb{R}^3}\mathrm{i}\omega\tilde{\varepsilon}_{\mathrm{b}}\nabla\psi(\boldsymbol{x}-\boldsymbol{y})\times\boldsymbol{w}(\boldsymbol{y})\,\mathrm{d}\boldsymbol{y}\,. \tag{3.31}$$

In the latter relations, $\mathscr{I}$ is the identity operator and ψ is the fundamental solution of the Helmholtz equation with propagation coefficient $\kappa_{\mathrm{b}} = \omega\sqrt{\tilde{\varepsilon}_{\mathrm{b}}\mu_0}$—in three

dimensions it is

$$\psi(\boldsymbol{r}) = \frac{\mathrm{e}^{-\mathrm{i}\kappa_\mathrm{b}|\boldsymbol{r}|}}{4\pi|\boldsymbol{r}|}, \tag{3.32}$$

whereas in two dimensions it is

$$\psi(\boldsymbol{r}) = -\frac{\mathrm{i}H_0^{(2)}(\kappa_\mathrm{b}|\boldsymbol{r}|)}{4}, \tag{3.33}$$

where $H_0^{(2)}$ is the zeroth order Hankel function of the second kind. These relations hold for homogeneous, possibly dissipative, backgrounds. Since the contrast source $\boldsymbol{w}$ has a bounded support—it coincides with the bounded volume of the examined body—, both the operators are well defined. Relations (3.30) and (3.31) are the same as (2.71) and (2.72) from the previous chapter when the background is air.

Since the adjoint operators are defined by means of inner products, it is necessary to explicitly choose the functional spaces $\mathbb{D}$ and $\mathbb{S}$ in order to compute them. Given the discrete nature of the measurements, which can be interpreted as an ordered collection of N complex values each one associated to a point in space or to a voxel—with reference to the definitions of the observation operator (3.10) and (3.11), respectively—, it is reasonable that $\mathbb{D} = \mathbb{C}^N$, and that for any $u, v \in \mathbb{D}$

$$(u|v)_\mathbb{D} = \mathrm{Re}\sum_{i=1}^{N} u_i v_i^* . \tag{3.34}$$

Being a continuous space, there is more freedom in the definition of the state space $\mathbb{S}$. For sake of simplicity, in the following it is set that $\mathbb{S} = L^2(\Omega, \mathbb{C}^3)$ and so for any $\boldsymbol{u}, \boldsymbol{v} \in \mathbb{S}$

$$(\boldsymbol{u}|\boldsymbol{v})_\mathbb{S} = \mathrm{Re}\int_\Omega \boldsymbol{u}(\boldsymbol{x}) \cdot \boldsymbol{v}^*(\boldsymbol{x})\,\mathrm{d}\boldsymbol{x}. \tag{3.35}$$

In this particular case the domain is the whole space, so $\Omega = \mathbb{R}^3$.

Once the inner products are defined, it is possible to compute the adjoint operators simply applying their definition (cfr. Appendix B). For the scattered electric field resolvent $\mathscr{S}_\mathrm{e}$ the following equalities, where Fubini's theorem [154] and the

symmetry of the dyadic Green's function are used, hold for any $\boldsymbol{u},\boldsymbol{v}\in\mathbb{S}$,

$$\begin{aligned}(\boldsymbol{u}|\mathscr{S}_{\mathrm{e}}\boldsymbol{v})_{\mathbb{S}} &= \mathrm{Re}\int_{\mathbb{R}^3}\boldsymbol{u}(\boldsymbol{x})\cdot\left(\int_{\mathbb{R}^3}\left(\left(\nabla\nabla+\kappa_0^2\mathscr{I}\right)\psi(\boldsymbol{x}-\boldsymbol{y})\right)\boldsymbol{v}(\boldsymbol{y})\,\mathrm{d}\boldsymbol{y}\right)^*\mathrm{d}\boldsymbol{x} = \\ &\mathrm{Re}\int_{\mathbb{R}^3\times\mathbb{R}^3}\boldsymbol{u}(\boldsymbol{x})\cdot\left(\left(\left(\nabla\nabla+\kappa_0^{*2}\mathscr{I}\right)\psi^*(\boldsymbol{x}-\boldsymbol{y})\right)\boldsymbol{v}^*(\boldsymbol{y})\right)\mathrm{d}\boldsymbol{x}\,\mathrm{d}\boldsymbol{y} = \\ &\mathrm{Re}\int_{\mathbb{R}^3\times\mathbb{R}^3}\left(\left(\left(\nabla\nabla+\kappa_0^{*2}\mathscr{I}\right)\psi^*(\boldsymbol{x}-\boldsymbol{y})\right)\boldsymbol{u}(\boldsymbol{x})\right)\cdot\boldsymbol{v}^*(\boldsymbol{y})\,\mathrm{d}\boldsymbol{x}\,\mathrm{d}\boldsymbol{y} = \\ &\mathrm{Re}\int_{\mathbb{R}^3}\left(\int_{\mathbb{R}^3}\left(\left(\nabla\nabla+\kappa_0^{*2}\mathscr{I}\right)\psi^*(\boldsymbol{x}-\boldsymbol{y})\right)\boldsymbol{u}(\boldsymbol{x})\,\mathrm{d}\boldsymbol{x}\right)\cdot\boldsymbol{v}^*(\boldsymbol{y})\,\mathrm{d}\boldsymbol{y} = (\mathscr{S}_{\mathrm{e}}^{\star}\boldsymbol{u}|\boldsymbol{v})_{\mathbb{S}}\,.\end{aligned} \tag{3.36}$$

Similarly, for the scattered magnetic field resolvent $\mathscr{S}_{\mathrm{h}}$ the following equalities, where Fubini's theorem and the relation $\boldsymbol{a}\cdot(\boldsymbol{b}\times\boldsymbol{c}) = -\boldsymbol{c}\cdot(\boldsymbol{b}\times\boldsymbol{a})$ are used, hold for any $\boldsymbol{u},\boldsymbol{v}\in\mathbb{S}$,

$$\begin{aligned}(\boldsymbol{u}|\mathscr{S}_{\mathrm{h}}\boldsymbol{v})_{\mathbb{S}} &= \mathrm{Re}\int_{\mathbb{R}^3}\boldsymbol{u}(\boldsymbol{x})\cdot\left(\int_{\mathbb{R}^3}\mathrm{i}\omega\tilde{\varepsilon}_{\mathrm{b}}\nabla\psi(\boldsymbol{x}-\boldsymbol{y})\times\boldsymbol{v}(\boldsymbol{y})\,\mathrm{d}\boldsymbol{y}\right)^*\mathrm{d}\boldsymbol{x} = \\ &\mathrm{Re}\int_{\mathbb{R}^3\times\mathbb{R}^3}\boldsymbol{u}(\boldsymbol{x})\cdot\left(-\mathrm{i}\omega\tilde{\varepsilon}_{\mathrm{b}}^*\nabla\psi^*(\boldsymbol{x}-\boldsymbol{y})\times\boldsymbol{v}^*(\boldsymbol{y})\right)\mathrm{d}\boldsymbol{x}\,\mathrm{d}\boldsymbol{y} = \\ &\mathrm{Re}\int_{\mathbb{R}^3\times\mathbb{R}^3}\left(\mathrm{i}\omega\tilde{\varepsilon}_{\mathrm{b}}^*\nabla\psi^*(\boldsymbol{x}-\boldsymbol{y})\times\boldsymbol{u}(\boldsymbol{x})\right)\cdot\boldsymbol{v}^*(\boldsymbol{y})\,\mathrm{d}\boldsymbol{x}\,\mathrm{d}\boldsymbol{y} = \\ &\mathrm{Re}\int_{\mathbb{R}^3}\left(\int_{\mathbb{R}^3}\mathrm{i}\omega\tilde{\varepsilon}_{\mathrm{b}}^*\nabla\psi^*(\boldsymbol{x}-\boldsymbol{y})\times\boldsymbol{u}(\boldsymbol{x})\,\mathrm{d}\boldsymbol{x}\right)\cdot\boldsymbol{v}^*(\boldsymbol{y})\,\mathrm{d}\boldsymbol{y} = (\mathscr{S}_{\mathrm{h}}^{\star}\boldsymbol{u}|\boldsymbol{v})_{\mathbb{S}}\,.\end{aligned} \tag{3.37}$$

Thus, the adjoint of the resolvent operators are the correlation products of the complex conjugate transpose of the dyadic Green's functions and the input fields,

$$\left(\mathscr{S}_{\mathrm{e}}^{\star}\boldsymbol{u}\right)(\boldsymbol{y}) = \int_{\mathbb{R}^3}\left(\left(\nabla\nabla+\kappa_0^{*2}\mathscr{I}\right)\psi^*(\boldsymbol{x}-\boldsymbol{y})\right)\boldsymbol{u}(\boldsymbol{x})\,\mathrm{d}\boldsymbol{x}, \tag{3.38}$$

and

$$\left(\mathscr{S}_{\mathrm{h}}^{\star}\boldsymbol{u}\right)(\boldsymbol{y}) = \int_{\mathbb{R}^3}\mathrm{i}\omega\tilde{\varepsilon}_{\mathrm{b}}^*\nabla\psi^*(\boldsymbol{x}-\boldsymbol{y})\times\boldsymbol{u}(\boldsymbol{x})\,\mathrm{d}\boldsymbol{x}, \tag{3.39}$$

for any field $u\in\mathbb{S}$. The derivation proposed here is based on the assumption that $\mathscr{S}_{\mathrm{e}}:\mathbb{S}\to\mathbb{S}$ and $\mathscr{S}_{\mathrm{h}}:\mathbb{S}\to\mathbb{S}$, which is reasonable for $\mathbb{S} = L^2(\Omega,\mathbb{C}^3)$.

For the positively rotating part operator, it is convenient to underline that $\mathscr{P}:\mathbb{S}\to L^2(\Omega,\mathbb{C})$ and that for any $u,v\in L^2(\Omega,\mathbb{C})$

$$(u|v)_{L^2(\Omega,\mathbb{C})} = \mathrm{Re}\int_{\Omega}u(\boldsymbol{x})v^*(\boldsymbol{x})\,\mathrm{d}\boldsymbol{x}. \tag{3.40}$$

Thus, the adjoint operator $\mathscr{P}^\star : L^2(\Omega,\mathbb{C}) \to \mathbb{S}$ is obtained noting that for any $u \in L^2(\Omega,\mathbb{C})$ and $\boldsymbol{v} \in \mathbb{S}$,

$$\begin{aligned}(u|\mathscr{P}\boldsymbol{v})_{L^2(\Omega,\mathbb{C})} = \mathrm{Re}\int_\Omega u(\boldsymbol{x})\left(\frac{v_x(\boldsymbol{x})+\mathrm{i}v_y(\boldsymbol{x})}{2}\right)^* \mathrm{d}\boldsymbol{x} = \\ \mathrm{Re}\int_\Omega \left(\frac{u(\boldsymbol{x})}{2}\hat{\mathbf{x}} - \mathrm{i}\frac{u(\boldsymbol{x})}{2}\hat{\mathbf{y}}\right)\cdot \boldsymbol{v}^*(\boldsymbol{x})\,\mathrm{d}\boldsymbol{x} = (\mathscr{P}^\star u|\boldsymbol{v})_{\mathbb{S}}\,,\end{aligned} \tag{3.41}$$

namely, for any $u \in L^2(\Omega,\mathbb{C})$,

$$\mathscr{P}^\star u = \frac{u}{2}\hat{\mathbf{x}} - \mathrm{i}\frac{u}{2}\hat{\mathbf{y}}. \tag{3.42}$$

It is worth noting that $\mathscr{S}_{\mathrm{h}}^{+;\star} = \mathscr{S}_{\mathrm{h}}^\star \mathscr{P}^\star$.

Finally, for the observation operator a couple of definitions have been proposed. Each definition leads to a different adjoint operator, so the two must be treated separately:

i. In the pointwise evaluations case (3.10), the domain of the observation operator is the subset of $L^2(\Omega,\mathbb{C})$ of continuous functions, $\mathscr{O} : \mathrm{dom}\,(\mathscr{O}) \subset L^2(\Omega,\mathbb{C}) \to \mathbb{D}$. The domain of $\mathscr{O}$ is dense in $L^2(\Omega,\mathbb{C})$, so it excludes just few elements, which can be approximated with arbitrary precision by continuous functions. The inner product reads for any $u \in \mathbb{D}$ and $v \in \mathrm{dom}\,(\mathscr{O})$

$$\begin{aligned}(u,\mathscr{O}v)_{\mathbb{D}} = \mathrm{Re}\sum_{i=1}^N u_i v^*(\boldsymbol{x}_i) = \mathrm{Re}\sum_{i=1}^N u_i \int_{\mathbb{R}^3} v^*(\boldsymbol{x})\delta_{\boldsymbol{x}_i}(\boldsymbol{x})\,\mathrm{d}\boldsymbol{x} = \\ \mathrm{Re}\int_{\mathbb{R}^3}\left(\sum_{i=1}^N u_i\delta_{\boldsymbol{x}_i}(\boldsymbol{x})\right) v^*(\boldsymbol{x})\,\mathrm{d}\boldsymbol{x} = (\mathscr{O}^\star u, v)_{L^2(\Omega,\mathbb{C})}\,,\end{aligned} \tag{3.43}$$

where $\delta_{\boldsymbol{x}_i}(\boldsymbol{x})$ is the Dirac delta centred in $\boldsymbol{x}_i$ and the linearity of integration has been employed. Therefore, using the definition of the observation operator by means of pointwise evaluations (3.10), for any $u \in \mathbb{D}$

$$\left(\mathscr{O}^\star u\right)(\boldsymbol{x}) = \sum_{i=1}^N u_i \delta_{\boldsymbol{x}_i}(\boldsymbol{x})\,. \tag{3.44}$$

ii. In the case in which the observation is defined by mean values of regions (3.11), the operator $\mathscr{O} : L^2(\Omega,\mathbb{C}) \to \mathbb{D}$ is well defined for every element of the

Lebesgue space. For any $u \in \mathbb{D}$ and $v \in L^2(\Omega, \mathbb{C})$, the inner product is

$$(u|\mathscr{O}v)_{\mathbb{D}} = \mathrm{Re}\sum_{i=1}^{N} u_i \frac{1}{|V_i|}\int_{V_i} v^*(\boldsymbol{x})\,\mathrm{d}\boldsymbol{x} = \mathrm{Re}\sum_{i=1}^{N} u_i \frac{1}{|V_i|}\int_{\mathbb{R}^3} v^*(\boldsymbol{x})\mathbb{1}_{V_i}(\boldsymbol{x})\,\mathrm{d}\boldsymbol{x} = \mathrm{Re}\int_{\mathbb{R}^3}\left(\sum_{i=1}^{N}\frac{u_i}{|V_i|}\mathbb{1}_{V_i}(\boldsymbol{x})\right) v^*(\boldsymbol{x})\,\mathrm{d}\boldsymbol{x} = (\mathscr{O}^\star u|v)_{L^2(\Omega,\mathbb{C})}\,, \tag{3.45}$$

where $\mathbb{1}_{V_i}(\boldsymbol{x})$ is the indicator function of V_i, equal to one inside V_i and to zero elsewhere. The linearity of integration has been used in the latter equalities. Thus, if the observation operator is defined as in (3.11), then for any $u \in \mathbb{D}$

$$\big(\mathscr{O}^\star u\big)(\boldsymbol{x}) = \sum_{i=1}^{N}\frac{u_i}{|V_i|}\mathbb{1}_{V_i}(\boldsymbol{x})\,. \tag{3.46}$$

3.2.4 Extension to multi-channel transmit coils

The cost functional (3.15) can be modified in order to incorporate the measurements of the transmit sensitivities of different sources, such as in the case of multiple coil settings [74] or for multi-channel transmit coils [121]. Assuming that for each of J settings, being J the number of considered sources, the scattered part of the transmit sensitivity $B_{1,j}^{+;\mathrm{s}}$ and the incident electric field $\boldsymbol{E}_j^{\mathrm{i}}$ are known—by measurements and by simulations, respectively—, a contrast source $\boldsymbol{w}_j$ for each setting and a common contrast χ are unknowns. Thus, by introducing for each coil setting a data residual

$$\rho_j[\boldsymbol{w}_j] = B_{1,j}^{+;\mathrm{s}}/\mu_0 - \mathscr{O}\mathscr{S}_{\mathrm{h}}^{+}\boldsymbol{w}_j\,, \tag{3.47}$$

and a state residual

$$\boldsymbol{r}_j[\boldsymbol{w}_j,\chi] = \chi\boldsymbol{E}_j^{\mathrm{i}} - \boldsymbol{w}_j + \chi\mathscr{S}_{\mathrm{e}}\boldsymbol{w}_j\,, \tag{3.48}$$

the cost functional becomes [74, 121]

$$F\left[(\boldsymbol{w}_j)_{j=1}^{J},\chi\right] = \frac{\eta_{\mathrm{d}}}{2}\sum_{j=1}^{J}\|\rho_j[\boldsymbol{w}_j]\|_{\mathbb{D}}^2 + \frac{\eta_{\mathrm{s}}[\chi]}{2}\sum_{j=1}^{J}\|\boldsymbol{r}_j[\boldsymbol{w}_j,\chi]\|_{\mathbb{S}}^2\,, \tag{3.49}$$

where $\eta_{\mathrm{d}} = (\sum_{j=1}^{J}\|B_{1,j}^{+;\mathrm{s}}/\mu_0\|_{\mathbb{D}}^2)^{-1}$ and $\eta_{\mathrm{s}}[\chi] = (\sum_{j=1}^{J}\|\chi\boldsymbol{E}_j^{\mathrm{i}}\|_{\mathbb{S}}^2)^{-1}$. The summations of the square norms of the residuals are the naturally induced square norms in the product spaces $\mathbb{D}^J$ and $\mathbb{S}^J$, where the minimisation takes place.

The minimisation procedure described above applies also for (3.49) with just few variations [120]. The first step is the contrast sources $(\boldsymbol{w}_j)_{j=1}^J$ update. It is performed using the conjugate gradient method with Polak-Ribière directions. Since just one contrast source appears in each addendum of the cost function F, this step is easily performed for each $j = 1,\dots,J$ by

$$\boldsymbol{w}_j^{n+1} = \boldsymbol{w}_j^n + \alpha^n \boldsymbol{v}_j^n, \tag{3.50}$$

where the direction $\boldsymbol{v}_j^n$ is defined by (3.17) using the gradient of the cost functional with respect to the j-th contrast source,

$$\boldsymbol{g}_j^n = -\eta_\mathrm{d} \mathscr{S}_\mathrm{h}^{+;\star} \mathscr{O}^\star \rho_j^n + \eta_\mathrm{s}^n (\mathscr{S}_\mathrm{e}^\star [\chi^{n,*} \boldsymbol{r}_j^n] - \boldsymbol{r}_j^n). \tag{3.51}$$

The step length α^n is chosen as the optimal real-valued step that minimises the cost functional along the selected direction,

$$\alpha^n = \underset{\alpha\in\mathbb{R}}{\arg\min}\, F\left[\left(\boldsymbol{w}_j^n + \alpha^n \boldsymbol{v}_j^n\right)_{j=1}^J, \chi^n\right]. \tag{3.52}$$

The optimal step length can be computed analytically following the same procedure as for the single-measurement case, namely by solving the Euler equation of the line minimisation problem. The result is

$$\alpha^n = \frac{-\sum_{j=1}^J \left(\boldsymbol{g}_j^n | \boldsymbol{v}_j^n\right)_\mathbb{S}}{\eta_\mathrm{d} \sum_{j=1}^J \|\mathscr{O}\mathscr{S}_\mathrm{h}^+ \boldsymbol{v}_j^n\|_\mathbb{D}^2 + \eta_\mathrm{s}^n \sum_{j=1}^J \|\chi^n \mathscr{S}_\mathrm{e} \boldsymbol{v}_j^n - \boldsymbol{v}_j^n\|_\mathbb{S}^2}, \tag{3.53}$$

which is equivalent to (3.25), but the inner product and the norms are the ones induced in the product spaces $\mathbb{D}^J$ and $\mathbb{S}^J$.

Similarly, the contrast is updated by minimising analytically the $\mathbb{S}^J$-norm of the state residual $\sum_{j=1}^J \|\boldsymbol{r}_j[\boldsymbol{w}_j^{n+1}, \chi]\|_\mathbb{S}^2$. To solve the Euler equation associated to this

minimisation problem leads to the following result, analogous to relation (3.28),

$$\chi^{n+1} = \frac{\sum_{j=1}^{J} \boldsymbol{w}_j^{n+1} \cdot \left(\boldsymbol{E}_j^{\mathrm{i}} + \mathscr{S}_{\mathrm{e}} \boldsymbol{w}_j^{n+1} \right)^*}{\sum_{j=1}^{J} \left| \boldsymbol{E}^{\mathrm{i}} + \mathscr{S}_{\mathrm{e}} \boldsymbol{w}_j^{n+1} \right|^2} . \tag{3.54}$$

Finally, the initial guess on the contrast source is done by back propagation [120], namely the vector $(\boldsymbol{w}_j^0)_{j=1}^J$ is the minimiser of the $\mathbb{D}^J$-norm of the data residual $\sum_{j=1}^J \|\rho_j[\boldsymbol{w}_j]\|_{\mathbb{D}}^2$. Being the addendum of the sum all positive, it is equivalent to choose $\boldsymbol{w}_j^0$ such that it minimises $\|\rho_j[\boldsymbol{w}_j]\|_{\mathbb{D}}^2$, that is, for each $j = 1, \ldots, J$ [120],

$$\boldsymbol{w}_j^0 = \frac{\left\| \mathscr{S}_{\mathrm{h}}^{+;\star} \mathscr{O}^\star B_{1,j}^{+;\mathrm{s}} \right\|_{\mathbb{S}}^2}{\left\| \mathscr{O} \mathscr{S}_{\mathrm{h}}^{+} \mathscr{S}_{\mathrm{h}}^{+;\star} \mathscr{O}^\star B_{1,j}^{+;\mathrm{s}} \right\|_{\mathbb{D}}^2} \mathscr{S}_{\mathrm{h}}^{+;\star} \mathscr{O}^\star B_{1,j}^{+;\mathrm{s}} / \mu_0 . \tag{3.55}$$

The extension of csiEPT to multiple coil settings may be extremely useful in MRI safety applications when multi-channel transmit coils are used for parallel transmission (pTX), because it allows to estimate the electric field $\boldsymbol{E}_j[\boldsymbol{w}_j] = \boldsymbol{E}_j^{\mathrm{i}} + \mathscr{S}_{\mathrm{e}} \boldsymbol{w}_j$ generated by each channel. Indeed, thanks to the linearity of the electromagnetic problem, the electric field generated by whichever feed of the channels is a linear combination of the field generated by each channel. This fact opens up the possibility of introducing a constraint on the maximum local SAR as a selection criterion when looking for the optimal feed in pTX.

3.3 The importance of modelling physics

The intrinsic advantage of the generalised framework described in the previous section is the possibility to adapt the csiEPT technique to different physical situations by properly defining the linear and bounded operators $\mathscr{S}_{\mathrm{e}}$ and $\mathscr{S}_{\mathrm{h}}$. Since csiEPT is an iterative procedure that applies many times the mentioned operators, the right balance between accuracy and efficiency of the implementation must be found in order to perform a reasonable estimate of the electric properties in few minutes.

Since birdcage coils are usually shielded with conductive materials in order to avoid the propagation of the RF field in the surrounding environment, avoid detuning when the coil is inserted in the static magnetic field and increase efficiency, the problem of a shielded birdcage coil is considered in this section. For such a problem, the boundary-free implementation introduced above [74] is a rough approximation of the physical system, which is better modelled by a numerical solution of Maxwell equations [122].

3.3.1 2D implementation for a shielded birdcage coil

The mid-plane of a shielded birdcage coil, which is parallel to the transverse plane $\hat{\boldsymbol{x}} \otimes \hat{\boldsymbol{y}}$, can be approximately modelled by the TM assumption, *i.e.* $H_z = E_x = E_y = 0$. This approximation is quite accurate when the coil is unloaded, anyway, it is maintained in presence of a body, of which just a section is considered. Usually, the shield for a birdcage coil is a cylinder concentric with the birdcage itself and made of an electrically conductive material. In the following, the shield is assumed to be made of a perfect electric conductor (PEC), *i.e.* it is assumed to have an infinite electric conductivity. Mathematically, this means that the electric field must be perpendicular to the surface of the shield, or equivalently that the component of the electric field tangential to the surface of the shield must vanish, which reads like a homogeneous Dirichlet boundary condition for the E_z^{s} unknown.

The equivalent Maxwell equations (3.7) can be combined in a single second-order equation for the scattered electric field by explicating the magnetic field from the equivalent Faraday's law

$$\boldsymbol{H}^{\mathrm{s}} = \frac{\mathrm{i}}{\omega \mu_0} \nabla \times \boldsymbol{E}^{\mathrm{s}}, \tag{3.56}$$

and substituting it in the equivalent Ampère's law

$$\nabla \times \nabla \times \boldsymbol{E}^{\mathrm{s}} = \kappa_{\mathrm{b}}^2 \boldsymbol{E}^{\mathrm{s}} + \kappa_{\mathrm{b}}^2 \boldsymbol{w}. \tag{3.57}$$

In the particular case in which $\boldsymbol{E}^{\mathrm{s}} = E_z^{\mathrm{s}} \hat{\boldsymbol{z}}$, the latter equation is the two-dimensional Helmholtz equation. Thus, the mid-plane of a shielded birdcage coil can be modelled

by the following problem,

$$\begin{cases} -\nabla^2 E_z^{\mathrm{s}} - \kappa_{\mathrm{b}}^2 E_z^{\mathrm{s}} = \kappa_{\mathrm{b}}^2 w_z\,, & \text{in } \Omega \\ E_z^{\mathrm{s}} = 0\,, & \text{on } \partial\Omega \end{cases} \tag{3.58}$$

whose domain Ω is the circle bounded by the PEC shield. The linear and bounded operator $\mathscr{S}_{\mathrm{e}}$ is conveniently interpreted as the resolvent of problem (3.58). Differently from the boundary-free implementation (3.30), where an explicit representation of $\mathscr{S}_{\mathrm{e}}$ is achieved, in this case the implicit definition is the best result that can be reached, since no analytical solutions are known for the considered Helmholtz problem.

Being the resolvent operator $\mathscr{S}_{\mathrm{e}}$ defined implicitly, the computation of the adjoint operator $\mathscr{S}_{\mathrm{e}}^{\star}$ is a little trickier than for the boundary-free implementation. In order to perform this computation, it is convenient to introduce an abstract explicit definition for the operator. Precisely, the Helmholtz problem with homogeneous Dirichlet boundary conditions is denoted by the operator $\mathscr{H}$, and the operator $\mathscr{K}$ is introduced such that, for any $u \in \mathbb{S}$, $\mathscr{K} u = \kappa_{\mathrm{b}}^2 u$. Thus, the problem (3.58) can be rewritten as $\mathscr{H} E_z^{\mathrm{s}} = \mathscr{K} w_z$, and the resolvent operator is

$$\mathscr{S}_{\mathrm{e}} = \mathscr{H}^{-1}\mathscr{K}\,, \tag{3.59}$$

whose adjoint is (cfr. Appendix B)

$$\mathscr{S}_{\mathrm{e}}^{\star} = \mathscr{K}^{\star}\left(\mathscr{H}^{-1}\right)^{\star} = \mathscr{K}^{\star}\left(\mathscr{H}^{\star}\right)^{-1}. \tag{3.60}$$

On the one hand, whatever the choice of $\mathbb{S}$ is, it is easy to show that, for any $u \in \mathbb{S}$, $\mathscr{K}^{\star} u = \kappa_{\mathrm{b}}^{*2} u$. Indeed, for any $u, v \in \mathbb{S}$,

$$\left(u|\mathscr{K} v\right)_{\mathbb{S}} = \left(u|\kappa_{\mathrm{b}}^2 v\right)_{\mathbb{S}} = \left(\kappa_{\mathrm{b}}^{*2} u|v\right)_{\mathbb{S}} = \left(\mathscr{K}^{\star} u|v\right)_{\mathbb{S}}. \tag{3.61}$$

On the other hand, the operator $\mathscr{H}^{\star}$ is associated to the partial differential equation problem that is the dual of the Helmholtz one with homogeneous Dirichlet boundary conditions. In summary, to apply the adjoint operator $\mathscr{S}_{\mathrm{e}}^{\star}$ to any field $u \in \mathbb{S}$ is equivalent to multiply by κ_{b}^{*2} the solution $v \in \mathbb{S}$ to the dual problem [131]

$$\begin{cases} -\nabla^2 v - \kappa_{\mathrm{b}}^{*2} v = u\,, & \text{in } \Omega \\ v = 0\,, & \text{on } \partial\Omega \end{cases} \tag{3.62}$$

The resolvent operator for the scattered magnetic field $\mathscr{S}_{\mathrm{h}}$ can be defined starting from $\mathscr{S}_{\mathrm{e}}$, because of Faraday's law (3.56). Under the TM assumption, Faraday's law can be written in operator notation as

$$\left(H_x^{\mathrm{s}}, H_y^{\mathrm{s}}\right) = \mathscr{D} E_z^{\mathrm{s}} = \frac{\mathrm{i}}{\omega\mu_0}\left(\frac{\partial E_z^{\mathrm{s}}}{\partial y}, -\frac{\partial E_z^{\mathrm{s}}}{\partial x}\right), \tag{3.63}$$

where $\mathscr{D}$ is the differential operator proportional to the curl. Thus, the resolvent operator for the magnetic field is defined by composition as $\mathscr{S}_{\mathrm{h}} = \mathscr{D}\mathscr{S}_{\mathrm{e}}$, whose adjoint is $\mathscr{S}_{\mathrm{h}}^{\star} = \mathscr{S}_{\mathrm{e}}^{\star}\mathscr{D}^{\star}$. In order to compute the adjoint operator $\mathscr{D}^{\star}$, it is worth noting that, by construction, the range of $\mathscr{S}_{\mathrm{e}} : \mathbb{S} \to \mathrm{ran}\,(\mathscr{S}_{\mathrm{e}}) \subset \mathbb{S}$ is a subset of $\mathbb{S}$ whose functions are null at the boundary $\partial\Omega$. Therefore, for any "magnetic" field $\boldsymbol{u} \in L^2(\Omega, \mathbb{C}^2)$ and any "electric" field $v \in \mathrm{ran}\,(\mathscr{S}_{\mathrm{e}})$

$$\begin{aligned}(\boldsymbol{u}|\mathscr{D}v)_{L^2(\Omega,\mathbb{C}^2)} = \mathrm{Re}\int_{\Omega} \boldsymbol{u}(\boldsymbol{x}) \cdot \left(\frac{\mathrm{i}}{\omega\mu_0}\left(\frac{\partial v}{\partial y}(\boldsymbol{x}), -\frac{\partial v}{\partial x}(\boldsymbol{x})\right)\right)^{*} = \\ \mathrm{Re}\int_{\Omega} \frac{-\mathrm{i}}{\omega\mu_0}\left(\frac{\partial u_y}{\partial x}(\boldsymbol{x}) - \frac{\partial u_x}{\partial y}(\boldsymbol{x})\right) v^{*}(\boldsymbol{x})\,\mathrm{d}\boldsymbol{x} = (\mathscr{D}^{\star}\boldsymbol{u}|v)_{\mathbb{S}}\,,\end{aligned} \tag{3.64}$$

where Green's identities have been used to move the derivatives from v to $\boldsymbol{u}$ and the integral on the boundary vanishes because $v = 0$ on $\partial\Omega$. As a consequence, $\mathscr{D}^{\star}$ is the formal adjoint of the differential operator $\mathscr{D}$, namely for any field $\boldsymbol{u} \in L^2(\Omega, \mathbb{C}^2)$

$$\mathscr{D}^{\star}\boldsymbol{u} = \frac{-\mathrm{i}}{\omega\mu_0}\left(\frac{\partial u_y}{\partial x} - \frac{\partial u_x}{\partial y}\right). \tag{3.65}$$

The particular two-dimensional implementation of csiEPT for a shielded birdcage coil developed in this section has been proposed for the first time by the author in [122].

3.3.2 Numerical coding of the csiEPT implementations

The generalised procedure for csiEPT described above has been coded in C++ with an extensive use of the object-oriented programming paradigm and the template metaprogramming technique [155]. The adoption of such an advanced programming set-up allows translating naturally in C++ code the abstract mathematical formalism used in this chapter. Since the two-step iterative procedure for cost minimisation has

been coded once and for all, different implementations of csiEPT are obtained just by coding properly the resolvent operators $\mathscr{S}_\mathrm{e}$ and $\mathscr{S}_\mathrm{h}$ and their adjoint operators.

Boundary-free implementation

The boundary-free domain implementation is characterised by convolution integrals with a kernel $G(\boldsymbol{x}-\boldsymbol{y})$ for both the resolvent operators (3.30), (3.31). In this case, given a generic input field $f(\boldsymbol{x})$, the application of any of the operators can be discretised on a uniform Cartesian grid of a parallelepiped big enough to contain the support of f as the discrete linear convolution

$$u_{i,j,k} = \Delta x \Delta y \Delta z \sum_{i'=1}^{N_x} \sum_{j'=1}^{N_y} \sum_{k'=1}^{N_z} G_{i-i',j-j',k-k'} f_{i',j',k'} \,, \tag{3.66}$$

where the subscripts i, j, k denote the evaluation of the quantity in the node $\boldsymbol{x}_{i,j,k}$ of the grid, Δx, Δy and Δz are the steps in the three Cartesian directions of the grid and N_x, N_y and N_z are the number of nodes in the grid for each direction.

In order to compute efficiently a discrete linear convolution, the discrete Fourier transform can be used, as it is shown in the following with reference to the one-dimensional case

$$u_i = \sum_{i'=1}^{N} G_{i-i'} f_{i'} \,, \quad \text{for } \; i = 1,\ldots,N \,. \tag{3.67}$$

Clearly, the kernel $G_{i-i'}$ is the longest vector in the convolution relation, because its index $i-i'$ goes from $-N+1$ to $N-1$, for a total of $L = 2N-1$ elements. The discrete linear convolution can be computed by the discrete Fourier transform after the introduction of the zero-padded input quantity

$$\hat{f}_i = \begin{cases} f_i, & \text{if } \; 1 \le i \le N \\ 0, & \text{if } \; N+1 \le i \le L \end{cases} \tag{3.68}$$

By assuming that all the sequences are extended from $\{1,\ldots,L\}$ to $\mathbb{Z}$ by periodicity, the following proposition is proven [156].

Proposition 3.1. *The following relation holds,*

$$\sum_{i'=1}^{N} G_{i-i'} f_{i'} = \frac{1}{L} \sum_{k=1}^{L} \theta^{-ik} \sum_{m=1}^{L} G_m \theta^{mk} \sum_{n=1}^{L} \hat{f}_n \theta^{nk} \,, \tag{3.69}$$

with $\theta = \mathrm{e}^{-\mathrm{i}2\pi/L}$. *Namely, the discrete Fourier transform of a discrete linear convolution is equal to the component wise product of the discrete Fourier transforms of the zero-padded periodically extended factors of the convolution.*

Proof. The right hand side of (3.69) is elaborated first to obtain

$$\phi_i = \frac{1}{L}\sum_{k=1}^{L}\theta^{-ik}\sum_{m=1}^{L}G_m\theta^{mk}\sum_{n=1}^{L}\hat{f}_n\theta^{nk} = \sum_{n=1}^{N}\sum_{m=1}^{L}G_m f_n\frac{1}{L}\sum_{k=1}^{L}\theta^{(m+n-i)k}.$$

The summation of the θ powers can be computed analytically. Indeed, if the exponent of θ is a multiple of L, *i.e.*, there exists an integer $s \in \mathbb{Z}$ such that $m+n-i = sL$, then the addenda of the summation are all equal to one and the result is L; otherwise—when the exponent of θ is not a multiple of L—the sum is null. This can be seen geometrically by observing that the addenda are disposed in the Argand diagram as the vertices of the regular polygon with L sides inscribed in the circumference of radius 1 centred at the origin. Thus, the previous relation can be further elaborated by using the Kronecker delta notation,

$$\phi_i = \sum_{n=1}^{N}\sum_{m=1}^{L}G_m f_n\delta_{m+n-i,sL} = \sum_{n=1}^{N}G_{i-n+sL}f_n\,, \quad \forall s \in \mathbb{Z}.$$

By choosing $s = 0$, the latter relation is equivalent to the left hand side of (3.69). ♦

This result is naturally extended to two or three dimensions by linearity. Since the discrete Fourier transform is computed very efficiently by the fast Fourier transform (FFT) algorithm [156], proposition 3.1 is extremely useful for the efficient coding of the boundary-free implementation. The computational cost of the FFT is linearithmic with respect to the number of nodes in the Cartesian grid. Precisely, the complexity of computing the convolution (3.67) using the FFT algorithm is $O(L\log L)$, whereas the complexity of the direct computation of the sum is $O(N^2)$, so, despite $L > N$, for a grid with enough nodes the convenience of FFT is massive [157]. The efficient implementation of the FFT algorithm in the library FFTW 3.3.4 [158] has been used for the C++ coding of the operators.

In a completely analogous fashion, it is possible to apply the adjoint operators (3.38) and (3.39) by using the FFT algorithm. Both the operators are correlation products whose kernels are the complex conjugate of the primal operators' kernels.

The one-dimensional case of study reads

$$u_i = \sum_{i'=1}^{N} G^*_{i'-i} f_{i'}\,, \quad \text{for } i = 1,\dots,N\,. \tag{3.70}$$

In this case, it is true that

$$u_i = \frac{1}{L}\sum_{k=1}^{L} \theta^{-ik} \sum_{m=1}^{L} G^*_m \theta^{-mk} \sum_{n=1}^{L} \hat{f}_n \theta^{nk} = \frac{1}{L}\sum_{k=1}^{L} \theta^{-ik} \left(\sum_{m=1}^{L} G_m \theta^{mk}\right)^* \sum_{n=1}^{L} \hat{f}_n \theta^{nk}\,. \tag{3.71}$$

The latter relation can be proven in the same way as proposition 3.1. It is worth noting that the forward discrete Fourier transform of the kernel, $\sum_{m=1}^{L} G_m \theta^{mk}$, appears in both the convolution (3.69) and the correlation (3.71). Therefore, the code can be optimised by performing the FFT of the two kernels once and for all during the whole minimisation procedure.

Shielded birdcage coil 2D implementation

In the two-dimensional implementation for a shielded birdcage coil, the resolvent operator $\mathscr{S}_\mathrm{e}$ and its adjoint are defined implicitly by the differential problems (3.58) and (3.62). Since these problems cannot be solved analytically, the application of the operators is performed relying on some numerical method. Precisely, the finite element method (FEM) with linear elements on a triangular mesh is used in the following. The result resembles what is described in [152].

Thanks to FEM, both the problems can be approximated as algebraic linear systems, which have to be solved any time the operators are applied. It is possible to solve the linear systems in an advantageous way for the iterative procedure by noting that the stiffness matrices depend only on the electric properties of the background. This fact allows to factorise the matrices only once before the start of iterations and to perform just a back and a forward substitutions for each operator application [132, 152]. In this way, the computational cost for the application of the resolvent operators in csiEPT is quadratic with respect to the number of unknowns—its complexity is $O(N^2)$. In order to code in C++ the electric field resolvent and its adjoint operator, the linear algebra has been handled using the open source library Eigen 3.3.3 [159].

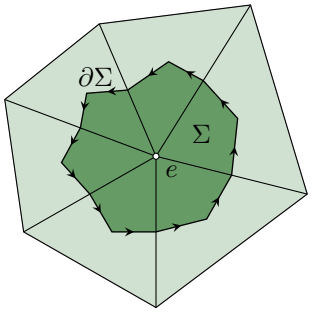

Fig. 3.9 Detail of the triangular mesh with a dual cell (dark green area). A diagrammatic representation of the terms involved in (3.72) is reported on the picture.

The discrete implementation of the operators $\mathscr{S}_\mathrm{h}$ and $\mathscr{S}_\mathrm{h}^\star$ is a little trickier. First, being the electric field E_z^s approximated by FEM with a continuous function that is affine in each triangle of the mesh, the differential operator $\mathscr{D}$ can be applied analytically on the discrete field to obtain an approximated magnetic field $\boldsymbol{H}^\mathrm{s}$, which is homogeneous on each triangle. As a consequence, the sets on which the discrete adjoint operator $\mathscr{D}^\star$ works are the set of "magnetic" fields that are constants in each triangle of the mesh—the domain—and the set of "electric" fields that are continuous and affine in each triangle of the mesh—the codomain. Thus, for any approximated "magnetic" field $\boldsymbol{u}$, $\mathscr{D}^\star\boldsymbol{u}$ should assign a value to each node of the triangular mesh, where the derivatives of the discontinuous field are not well-defined. To perform this, Stokes' theorem is employed as follows [122],

$$\left(\mathscr{D}^\star\boldsymbol{u}\right)_e \simeq \frac{1}{|\Sigma_e|}\int_{\Sigma_e}\left(\mathscr{D}^\star\boldsymbol{u}\right)(\boldsymbol{x})\,\mathrm{d}\boldsymbol{x} = \frac{-\mathrm{i}}{\omega\mu_0|\Sigma_e|}\oint_{\partial\Sigma_e}\boldsymbol{u}(\boldsymbol{x})\cdot\boldsymbol{\tau}(\boldsymbol{x})\,\mathrm{d}l(\boldsymbol{x})\,, \tag{3.72}$$

where e is the index of the node where the output is evaluated, Σ_e is the cell of the dual mesh corresponding to the node of index e and $\boldsymbol{\tau}$ is the unit vector counter clockwise tangent to $\partial\Sigma_e$, as shown in Fig. 3.9. The dual mesh is defined by connecting the barycentres of the triangles with the barycentres of the edges of the triangular mesh. Since $\boldsymbol{u}$ is known and constant in each triangle, the circulation in the latter equation is computed analytically for each node of the mesh. This approach is analogous to the one proposed in [160] for the computation of the divergence.

3.3.3 Model problem

The presented boundary free implementation (from now on referred to as FFT-CSI) is computationally more efficient than the two-dimensional implementation in presence of a conductive shield coded as described above (in the following referred to as FEM-CSI). Indeed, in general FFT-CSI requires less time than FEM-CSI to perform the same number of iterative steps [122]. This fact suggests the adoption of FFT-CSI to recover the electric properties independently of the presence of a conductive shield, in the expectation that the error introduced by disregarding the shield is negligible with respect to the numerical approximation. In order to quantify the discrepancy in the electric properties estimations achieved by FFT-CSI and FEM-CSI in presence of a conductive shield, the two implementations are tested on a realistic two-dimensional model problem.

A 16-legs birdcage coil with radius 16 cm is surrounded by a circular concentric PEC shield with radius 20 cm. The mid-plane of the birdcage—parallel to $\hat{\boldsymbol{x}} \otimes \hat{\boldsymbol{y}}$—is simulated under the TM assumption at 128 MHz, corresponding to a static field $B_0 = 3\,\mathrm{T}$. Each leg of the birdcage is modelled as a line source in the same way described in Section 3.1.3. The TM assumption is used also when the head of the anatomical human model Duke of the Virtual Family [140, 141] is inserted inside the birdcage coil. Only the section of the head pictured in figure 3.1 is considered. The electric properties are assigned to each tissue by elaborating the measurements collected in [112] in accordance to the 4^{th} order Cole–Cole dispersive model [30]. This procedure leads to the heterogeneous distributions depicted in Fig. 3.2, which are considered as the reference ones. In this case, both the incident and the total field are simulated numerically by the FEM applied to the triangular mesh pictured in Fig. 3.10, which has been obtained by the open source software Triangle 1.6 [161, 162]. The section of the head is located inside the inner structured portion of the mesh, which has 1 mm sides.

The electromagnetic field computed in this way is used as virtual measurement with no further post-processing, so it simulates a noise-free measurement where both the magnitude and the phase of the transmit sensitivity are known exactly. This ideal situation allows to study the error due to the physical modelling and the numerical procedure without the additional influence of other assumptions and noise. For both FFT-CSI and FEM-CSI, just a measurement of the transmit sensitivity is used as input. Since FFT-CSI works on a uniform Cartesian grid, only the values on the

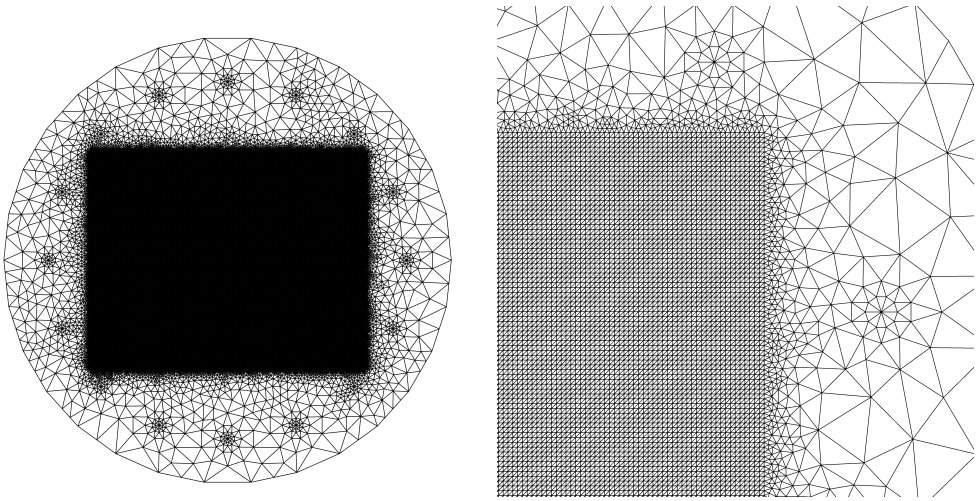

Fig. 3.10 Mesh on which the FEM has been applied. On the right, a detail of the structured portion of the mesh with 1 mm sides is shown.

structured portion of the mesh are used as input for it. The domain reduction implies a speed increase in FFT-CSI with respect to FEM-CSI.

The virtual measurements are performed as a point-wise evaluation (3.10). The measurement points are selected as the points of a uniform Cartesian grid with 1 mm resolution that fall inside the section of the head. This choice leads to an accurate modelling of the measurement that are performed by a MRI scanner, since no significant nuclear magnetic resonance signal is emitted by air due to the rareness of protons. Because of the steep change of electric properties from air to skin, the knowledge of the transmit sensitivity in some points in air is useful for a precise recovery of the properties. On the other hand, the lack of this information affects csiEPT [122]. Anyway, the accuracy is restored by the introduction of some *a priori* knowledge. Precisely, the non-negativity of the electric conductivity ($\sigma \geq 0$) and of the real part of the contrast ($\varepsilon_r \geq 1$) are imposed, together with a null contrast in air, as convex constraints. Clearly, the nodes in air can be deduced as the points where the transmit sensitivity cannot be measured by the MRI scanner.

Fig. 3.11 collects the electric properties distributions reconstructed by the two implementations of csiEPT after 5000 iterative steps of the minimisation procedure. The values estimated to be equal to the corresponding property of air ($\varepsilon_r = 1$ or $\sigma = 0$) are discarded and not displayed in the pictures. FFT-CSI is not able to recover the whole section, many points at the boundary are recovered as air, especially for the electric conductivity, whose reasonable reconstruction begins at the depth of the

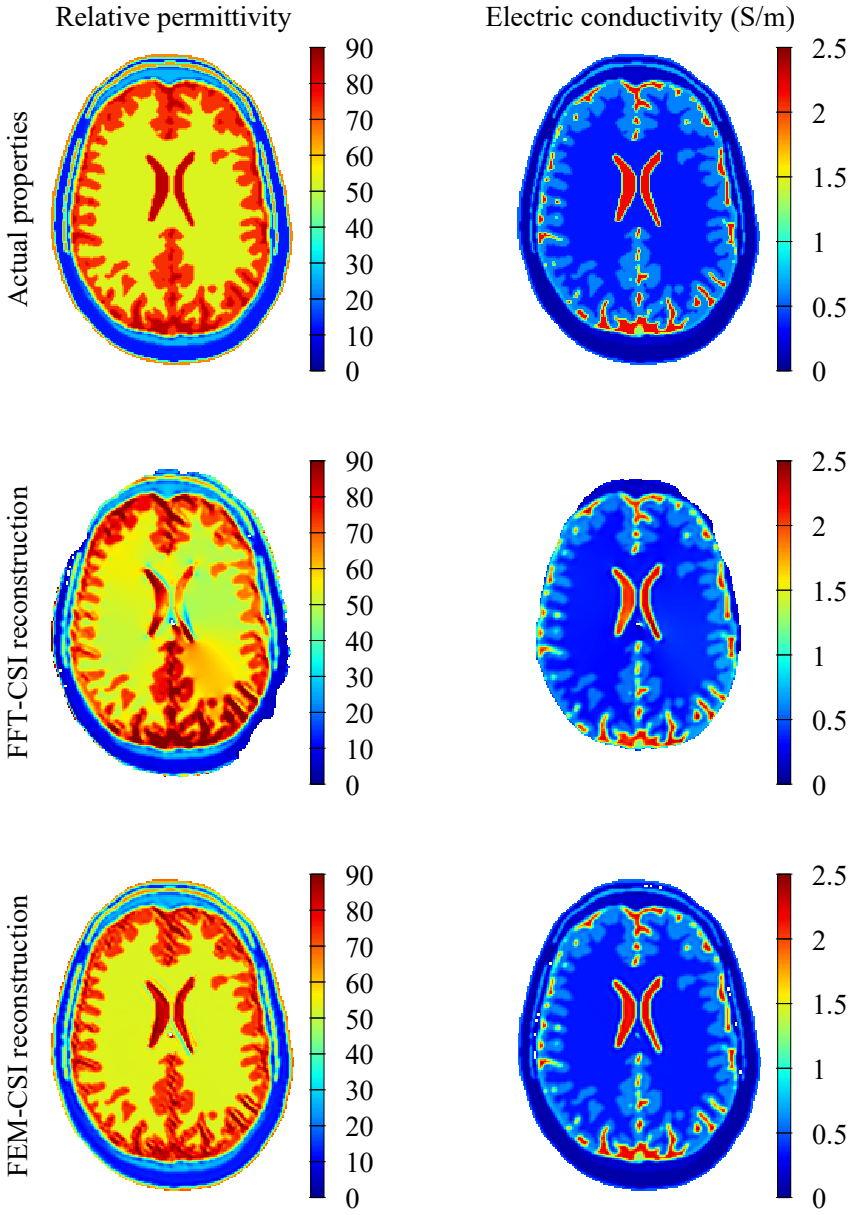

Fig. 3.11 The actual distributions of the electric properties of the head section and the ones recovered by the two implementations of csiEPT. The points where the estimated property is the same as the one of air ($\varepsilon_r = 1$ or $\sigma = 0$) are not displayed.

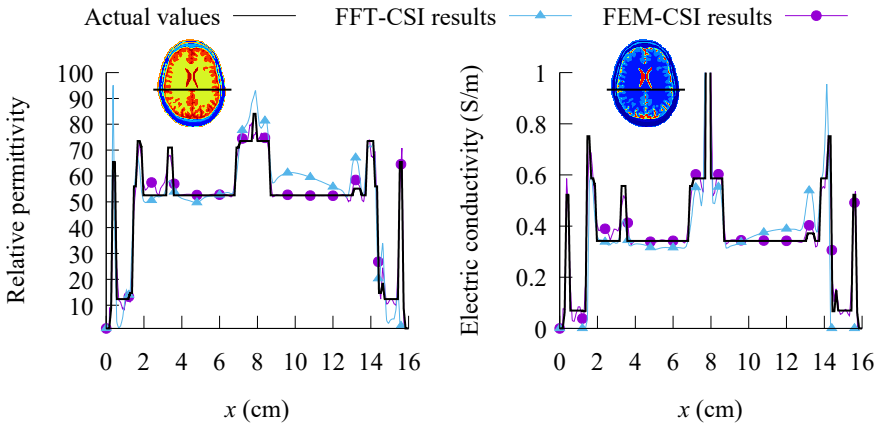

Fig. 3.12 Distributions of the actual electric properties and of the estimated ones along the line depicted in the insets.

brain. Although the electric conductivity is recovered by FFT-CSI with an acceptable accuracy inside the brain, the relative permittivity shows anomalous variations and heterogeneities with respect to the actual value. On the other hand, both the electric properties are accurately recovered by FEM-CSI. In this case, small errors in relative permittivity appear at some tissues' boundaries. They are related to the triangular mesh. Indeed, the errors change if the structured mesh is oriented differently and they would presumably disappear if quadrangular finite elements were employed. The distributions recovered by the two implementations can be compared more quantitatively in the plots of Fig. 3.12, where the trends of the actual and estimated electric properties along a line are reported. Limiting the analysis to the recovered points, the errors introduced by FFT-CSI are a little larger in relative permittivity than in electric conductivity, whereas a very precise reconstruction is obtained by FEM-CSI. However, the discontinuities at tissues' boundaries are located very precisely by both the methods.

It is worth noting that the discrepacies between FFT-CSI and FEM-CSI estimations grow up when the measurements of the transmit sensitivity are performed on coarser grids. The distributions recovered on a grid with 4 mm sides are reported in Fig. 3.13, where the values estimated as the properties of air are not displayed. Despite the low resolution, FEM-CSI recovers the tissues extension as well as the value of the properties. On the other hand, from the FFT-CSI result it is possible just to guess the boundaries of some tissues. It results that a robust implementation of csiEPT requires an accurate modelling of the physics of the measurements.

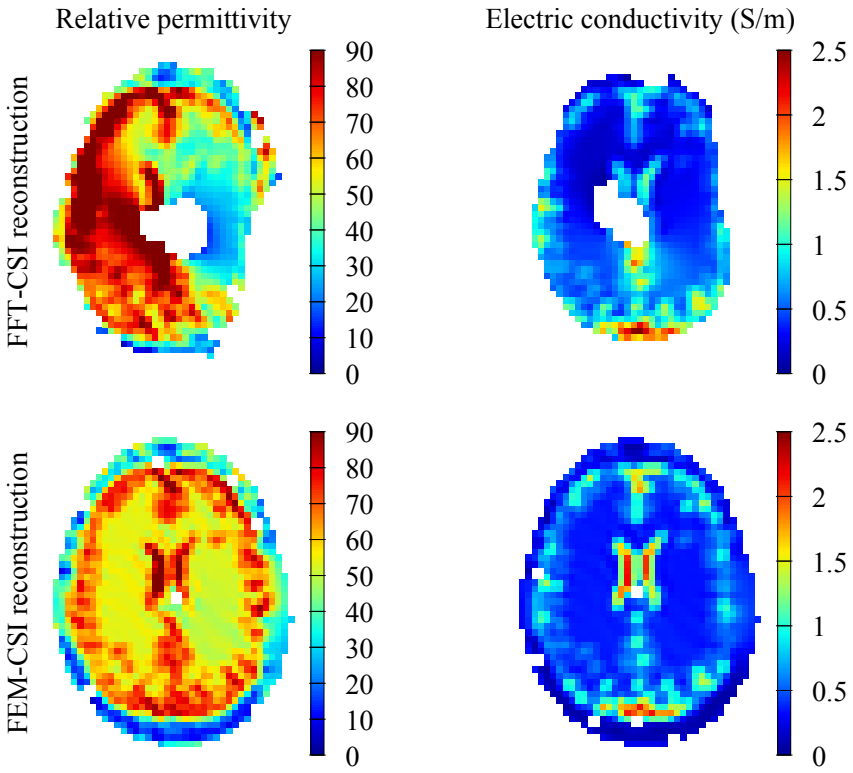

Fig. 3.13 Distributions of the electric properties estimated by the two implementation of csiEPT on a measurement and computational grid of 4 mm sides. The points where the estimated property is the same as the one of air ($\varepsilon_r = 1$ or $\sigma = 0$) are not displayed.

Differently from the current case study, in [122] a section of the abdomen in a whole-body coil of radius 35.6 cm has been studied. That situation results in a more sensible discrepancy between the two implementation than the current case study. In addition, that case gives more freedom in the positioning of the body inside the coil, so it has been moved near the shield in an asymmetric configuration. Despite this peripheral position of the body is not representative of a real imaging situation, it stresses the role played by the shield in the scattered field definition, because of the closeness of the equivalent scattering current with the conductive shield. In this extreme case, FEM-CSI still recovers precisely both the electric properties, whereas the errors committed by FFT-CSI grow up so much that the estimated distributions are completely wrong, although the interfaces between tissues are still localised [122]. This fact leads to the same consideration stated in the previous paragraph, namely that modelling the physics of the measurements as much accurately as possible is recommended for a more robust implementation of csiEPT.

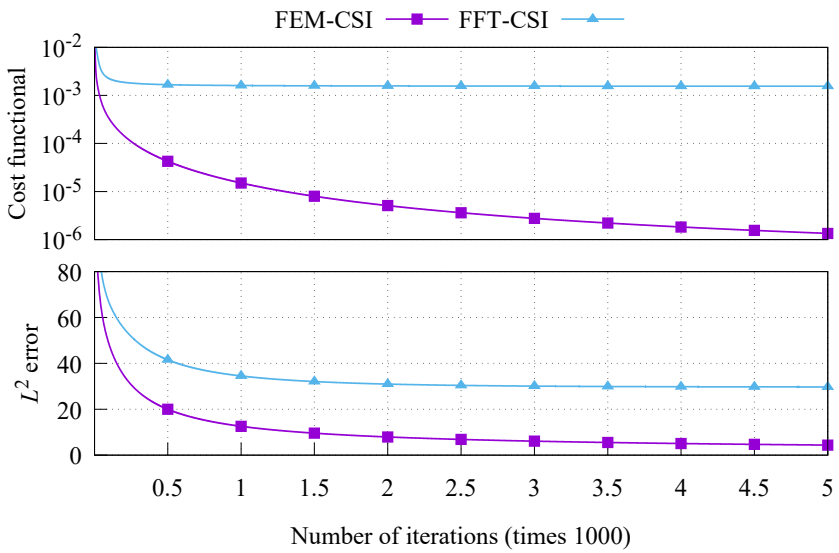

Fig. 3.14 Trends of the cost function $F[\boldsymbol{w},\chi]$ (above) and of the L^2 norm of the error in the contrast χ (below) during the iterative procedures.

A global description of the behaviour of the two implementations is reported in Fig. 3.14, where the cost functional $F[\boldsymbol{w}^n,\chi^n]$ and the integral error $\|\chi^n-\chi\|_{L^2(\Omega)}$, being χ the actual contrast map, are plotted against the number of iterations. The analysis of the cost functional's trends shows that FFT-CSI has converged to a positive optimal cost that is about three orders of magnitude higher than the cost reached after 5000 iterations by FEM-CSI. It is worth noting that FEM-CSI appears to be still decreasing. Analogously, because of the implicit relation that exists between the cost functional and the recovery error, FEM-CSI converges towards a contrast whose integral error tends to zero, whereas the integral error of the contrast estimated by FFT-CSI does not go below a positive minimum value.

Finally, because of the great value that csiEPT has in MRI safety applications, where an online estimation of the local SAR is required (cfr. 3.1), a comparison in the local SAR estimation by FFT-CSI and FEM-CSI is performed. The local SAR recovered by the two implementations and the actual local SAR, computed assuming a constant density $\delta = 1000\,\mathrm{kg\,m^{-3}}$ equal to the density of water, are collected in Fig. 3.15, where only the positive values are displayed. Despite FFT-CSI can estimate the local SAR only inside the brain, because it has been unable to retrieve the electric conductivity outside of it, it locates and quantifies as well as FEM-CSI the peak values, which are slightly overestimated by both the implementations. This fact happens because the local SAR is completely determined by the electric conductivity

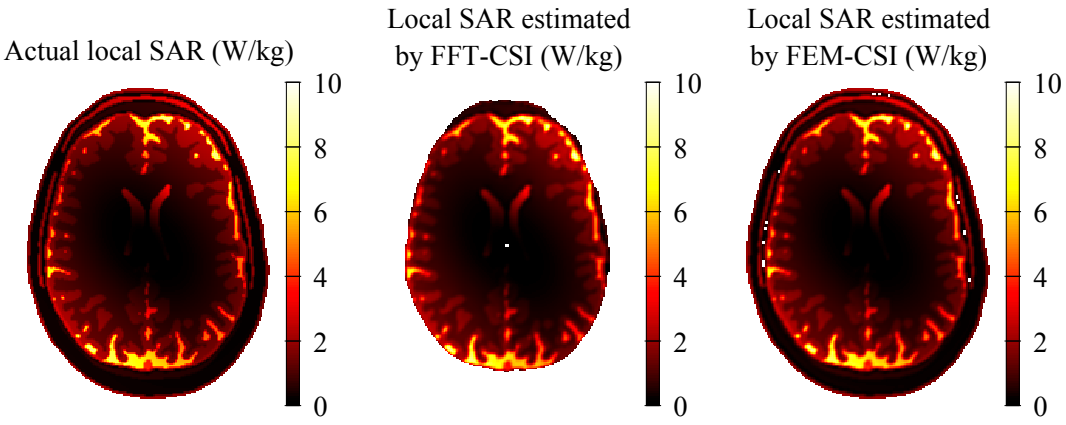

Fig. 3.15 The maps of the actual and estimated non-averaged local SAR due to a 16-legs birdcage coil of radius 14 cm rescaled such that the actual local SAR maximum is equal to $10\,\mathrm{W\,kg^{-1}}$. The results are referred to the two-dimensional model problem with TM assumption of an unshielded birdcage coil.

σ and the contrast source $\boldsymbol{w}$, whose reconstructions are more precise than the one of the relative permittivity ε_r. Clearly, the map of local SAR obtained by FFT-CSI strongly deteriorates in stressed conditions like in proximity of the conductive shield or in presence of coarse computational meshes.

The results achieved in this section show the importance of modelling accurately the physics of the problem in order to obtain a robust model. In addition, because of the higher computational cost of FEM-CSI with respect to FFT-CSI, the results suggest the search for efficient implementations of the involved operators.

3.4 Noise propagation

Since MREPT is a quantitative imaging technique that produces images in which every pixel brings numerical information, it is important to know how the uncertainty propagates from the input to the output. The uncertainty in the input is due to the adoption of a measurement procedure and can arise from thermal noise in addition to random as well as systematic errors. Clearly, to study how the uncertainty associated to the B_1-mapping result propagates through the MREPT method is essential in order to make it reliable for *in vivo* applications. Anyway, up to the best of the author's knowledge, besides the work developed in this thesis and published in [121] relatively to csiEPT, just a few efforts have been done to investigate on this topic

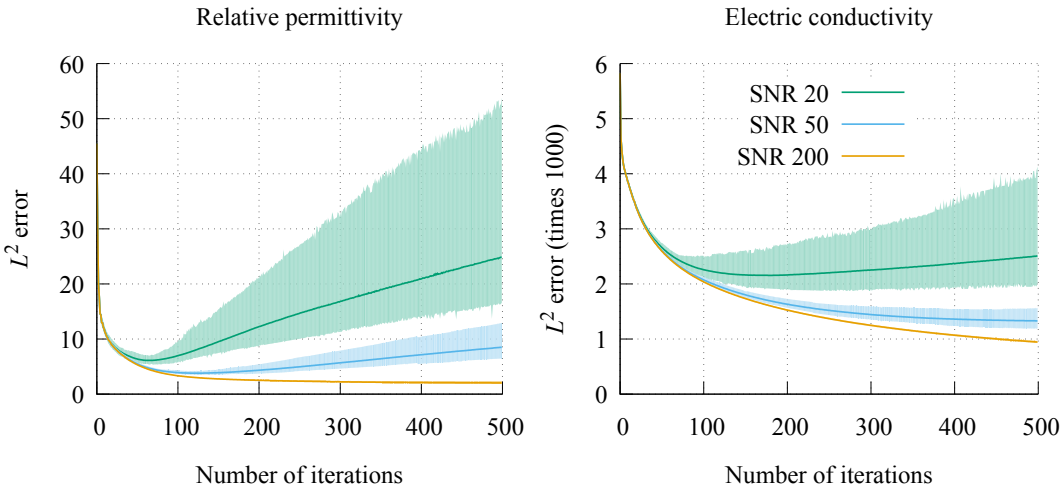

Fig. 3.16 Plots of the medians (solid lines) and shortest 95 % coverage intervals (bands) of the L^2 norm of the errors in relative permittivity ε_r and in electric conductivity σ against the iterative step of csiEPT. For each SNR, the statistics are computed on 1000 random extractions of noisy input obtained simulating a 16-legs birdcage coil loaded with a human head.

relatively to stdEPT [80]. In this section, uncertainty (or noise, these two words are used as synonym in the following) propagation in csiEPT is studied focusing on the electric properties estimation. The uncertainty in the estimated contrast source $\boldsymbol{w}$, and consequently in the estimated electromagnetic fields, is not investigated.

A peculiar difficulty in the uncertainty assessment of MREPT is that, as stated above, it is an ill-posed problem in the sense of Hadamard. Precisely, as a consequence of the compactness of the resolvent operators $\mathscr{S}_e$ and $\mathscr{S}_h$, the dependence of the electric properties distributions on the measured field is not continuous [51]. This kind of ill-posedness translates in ill-conditioning of the discretised MREPT problem, namely the presence of noise in the input data can strongly affect the recovery of the electric properties maps. Since csiEPT solves the inverse problem by minimising a cost functional with the conjugate gradient method, the ill-posedness appears in the property of semi-convergence of the iterative procedure. Precisely, during the iterations, the global error in the estimated properties starts decreasing until it reaches a minimum after a finite number of iterations, then it increases towards an asymptotic value.

The characteristic trend of the global error can be appreciated in the stochastic representation of Fig. 3.16, where the medians and the shortest 95 % coverage intervals of the global errors in the estimated relative permittivity and electric con-

ductivity are plotted with respect to the number of iterations. The model problem that leads to the data represented in Fig. 3.16 is the same considered in Section 3.1.3, an unshielded 16-legs birdcage coil loaded with a human head, with the addition of random noise to the simulated transmit sensitivity such that certain signal-to-noise ratios (SNR) are modelled. The SNR and the extraction procedure are technically described in the following of this section. A couple of valuable observations can be done looking at the stochastic trends of the errors:

i. The property of semi-convergence of csiEPT is more pronounced in the relative permittivity than in the electric conductivity. Indeed, the minimum of the error in ε_r is reached after less iterative steps than the steps needed to reach the minimum in σ. This fact recalls the comparison between FFT-CSI and FEM-CSI, in which the computation of the electric conductivity appears to be more robust than that of the relative permittivity.

ii. The property of semi-convergence is intrinsically related to randomness. In the first iterations, the error is almost independent of the noise in the input, its behaviour can be interpreted as deterministic. On the other hand, the role of the noise becomes more and more important coming closer to the minimum error and going on with the number of iterations, as can be seen from the spreading of the coverage intervals.

In order to reduce the influence of the noise in the recovered maps of the electric properties, and thus deal with the ill-posedness of the inverse problem, a regularisation strategy must be used. Since the contrast source $\boldsymbol{w}$ is already regularised by the state error, which, for this reason, is sometimes referred to as Maxwell's regulariser [163], only the contrast χ needs additional *a priori* information. Many regularisation strategies have been proposed in literature for the inverse scattering techniques in general and for the CSI method in particular, like, for example, the adoption of a special basis with few elements for the description of the contrast [51, 164], or the introduction of additive or multiplicative regularisation terms to the cost functional [165–167]. The multiplicative regularisation has been widely used in association with CSI [48, 120, 160] and it has been applied with good results to the original proposal of csiEPT [74]. Despite its diffusion, in this thesis the multiplicative regularisation has not been used because of its computational burden. Instead, in the following an early stopping criterion based on the data reported in

Fig. 3.16 is used as regularisation strategy. This naïve approach is not so far from using a small basis or from adding a Tikhonov regularisation term to the cost function, but it does not involve any additional computational cost.

3.4.1 Monte Carlo method

Since csiEPT is a non-linear minimisation problem and its linearisation could lead to an inadequate representation, the noise propagation through it is studied with the application of the Monte Carlo method (MCM), as prescribed by the Supplement 1 to GUM (Guide to the expression of Uncertainty in Measurement) [168].

As stated in [168], in the framework of uncertainty assessment the MCM does not simulate a random physical process like in other applications, but provides a numerical representation of the probability distribution of the output of a mathematical model when the input is a known random variable. So, the MCM is used to solve approximately a deterministic problem. In order to achieve the result, the MCM follows a very simple procedure: a given number M of realisations of the input random variable are sampled and for each one the mathematical model provides the output. The sorted collection of the outputs is the searched numerical representation of the propagated probability distribution.

In order to apply the MCM to the noise propagation in csiEPT the direct electromagnetic problem is simulated numerically so that the incident and the total fields, used as input virtual measurements, are known exactly. The measurement uncertainty (or noise) is modelled as an additive Gaussian noise and it is added only to the transmit sensitivity. In this assessment, the incident electric field is assumed noise-free. This assumption, done for sake of simplicity, is justified by the fact that the incident electric field can be estimated, by simulations or by measurements, with a supervised accuracy once and for all before any other measurement, so it is reasonably expected to play a minor role in noise propagation with respect to the transmit sensitivity mapping. Clearly, the results obtained by this investigation can be further improved by using a richer error budget which takes into account the uncertainty in the incident field measurement, in the possible misalignment of the incident field and the measured transmit sensitivity and so on.

Precisely, the noise in the measured transmit sensitivity is modelled as a random vector $\boldsymbol{\Xi} = (\Xi_i)_{i=1}^{N}$ with multivariate complex Gaussian distribution. Each compo-

nent Ξ_i of $\boldsymbol{\Xi}$ represents the random noise that appears in the measurement performed in the i-th measurement node (or voxel), namely if $B_{1,i}^+$ denotes the actual transmit sensitivity in the i-th node (or voxel), then the measured one is a realisation of the random variable $B_{1,i}^+ + \Xi_i$. Despite some spatial correlations between the components of $\boldsymbol{\Xi}$ may exist, for sake of simplicity it is assumed that they are statistically independent. More strictly, it is assumed that $(\mathrm{Re}(\Xi_i), \mathrm{Im}(\Xi_i))_{i=1}^N$ is a set of independent and identically distributed random variables with null mean and standard deviation u.

Since in the imaging community the concept of SNR is more common than that of standard deviation, u is described in terms of SNR. For any random variable f, the SNR is defined as the ratio between the mean value of the magnitude of f and the standard deviation of f [59] and it is denoted as $\mathrm{SNR}[f]$. Thus, the SNR of the i-th measurement is $\mathrm{SNR}[B_{1,i}^+ + \Xi_i] = |B_{1,i}^+|/u$. A typical parameter of the images obtained by MRI examinations is the spatially averaged SNR, that for the transmit sensitivity map is

$$\left\langle \mathrm{SNR}[B_1^+ + \boldsymbol{\Xi}] \right\rangle = \frac{\left\langle |B_1^+| \right\rangle}{u}, \tag{3.73}$$

where u is assumed constant in space and the diamond brackets denote the spatial averages. Given a spatially averaged SNR for the input map, the standard deviation of the noise u is obtained from the latter relation. Clearly, the SNR is used in the comments to the output of the MCM as well as for the input. In the following, the spatial averaged SNR is referred to as global SNR, whereas its evaluation pixel-by-pixel is referred to as local SNR.

For each analysed coil setting and considered global SNR of the transmit sensitivity maps, $M = 1000$ realisations of noise are extracted and used by the MCM. Fewer trials than that prescribed by [168] are used because of the significant computational burden of the minimisation procedure. However, the distributions of the output quantities are approximated reliably in this way, as can be seen looking at the histograms below, especially the ones with a small variance.

3.4.2 Noise propagation from birdcage coil measures

The mid-plane of an unshielded 16-legs birdcage coil loaded with the head of the anatomical human model Duke from the Virtual Family [140, 141], as the model problem considered in Section 3.1.3, is analysed. The legs are positioned on a circle of radius 14 cm. In order to take advantage of csiEPT for multi-channel transmit

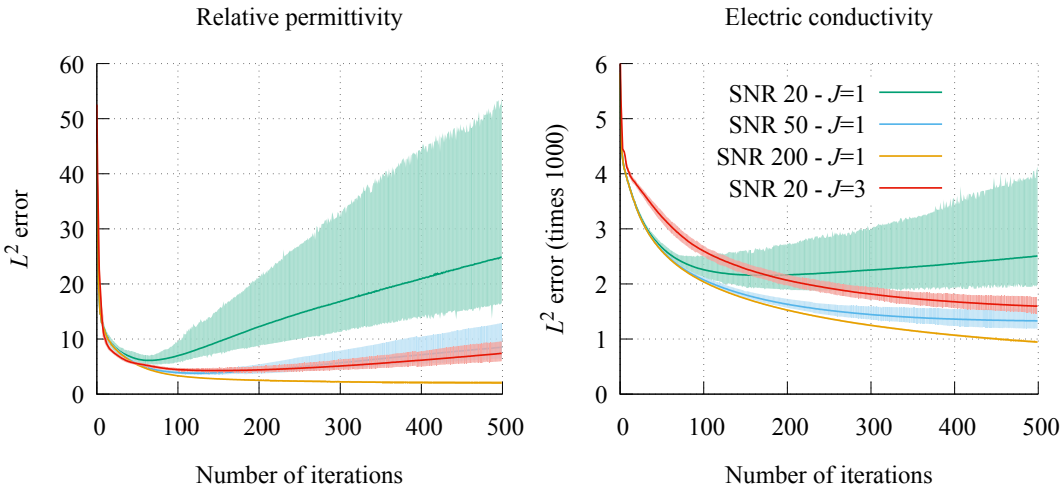

Fig. 3.17 Plots of the medians (solid lines) and shortest 95 % coverage intervals (bands) of the L^2 norm of the errors in relative permittivity ε_r and in electric conductivity σ against the iterative step of csiEPT. For each global SNR, the statistics are computed on 1000 random extractions of noisy input obtained simulating an unshielded 16-legs birdcage coil loaded with a human head. In the cases $J = 1$ the birdcage is excited in quadrature, whereas in the case $J = 3$ two linear and a quadrature excitations are used.

coils, some realistic excitations of birdcage coils are considered. Usual quadrature birdcage coils are double-tuned by two ports located in such a way to form an angle of 90°. The feed of each port leads to a linear excitation, one with a spatial phase shift of 90° with respect to the other. Assuming that the 16 line sources are numbered clockwise with the index $k = 1, \ldots, 16$, the current in the k-th source within the two linear excitations is, respectively,

$$I_k^{\mathrm{l}_1} = I\cos\left(\frac{k\pi}{8}\right), \qquad I_k^{\mathrm{l}_2} = I\cos\left(\frac{k\pi}{8}\right). \tag{3.74}$$

The conventional quadrature excitation (3.6) is obtained by summing up the linear excitations with a time delay of a quarter of period, viz.:

$$I_k^{\mathrm{q}} = I_k^{\mathrm{l}_1} + \mathrm{i} I_k^{\mathrm{l}_2}. \tag{3.75}$$

Thus, it is possible to use csiEPT from the measurement of the transmit sensitivity of a birdcage coil in quadrature (case $J = 1$), or from the measurements of all the sensitivities obtainable by the three excitations (case $J = 3$), where the number of measurements used to describe the cost functional (3.49) is denoted by J. In Fig. 3.16, the stochastic behaviour of the global error, measured as the L^2 norm of

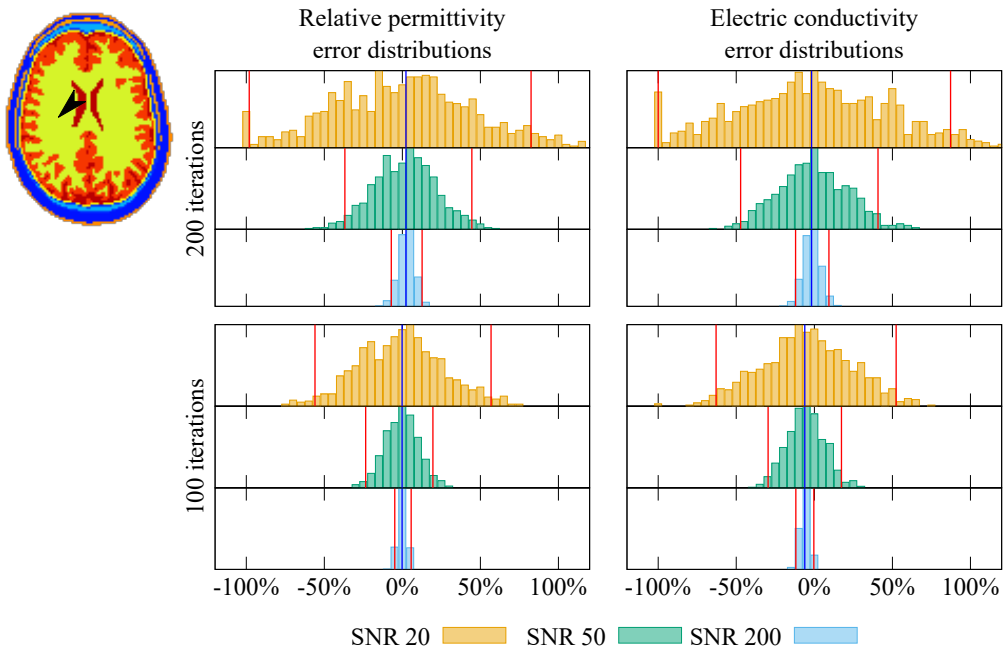

Fig. 3.18 Relative frequency histograms of the relative error of the estimated electric properties in the point of white matter indicated in the inset map. The properties recovered after 100 and 200 iterative steps are considered for different amount of SNR in the transmit sensitivity of a quadrature birdcage coil. The vertical blue lines denote the intrinsic bias, namely the relative error in the estimation in absence of noise. The vertical red lines denote the extremes of the shortest 95 % coverage intervals of the approximated distributions.

the difference between the actual and the estimated values, is reported for different amount of noise (global SNR 20, 50 and 200) in the case $J = 1$. The trend of the error in the case $J = 3$ when the input data have global SNR 20 is compared with the others in Fig. 3.17, which makes clear the advantage of using multiple measurements in csiEPT. Indeed, despite the higher amount of noise, the evolution of the red line (global SNR 20 and $J = 3$) is very close to that of the blue line (global SNR 50 and $J = 1$).

In Fig. 3.18, the relative frequency histograms of the relative error in the estimation of the electric properties after 100 and 200 iterations are reported for different amounts of noise. Reasonably, the uncertainty in the output is higher when it is higher in the input. Moreover, as can be envisaged from the trends of Fig. 3.16, the variance of the output distributions increases with the number of iterations of the minimisation procedure. The distributions are all approximately symmetric, but the one obtained after 200 steps with an input SNR equal to 20. In this case, a localised peak is present at -100 % for both the properties as a consequence of the positivity

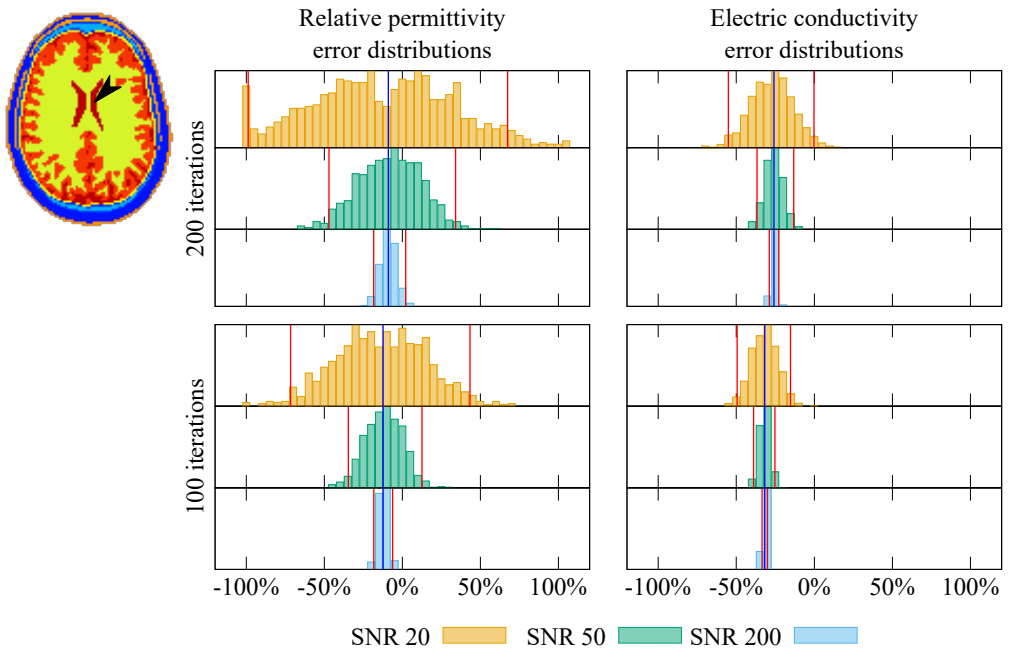

Fig. 3.19 Relative frequency histograms of the relative error of the estimated electric properties in the point of cerebrospinal fluid indicated in the inset map. The properties recovered after 100 and 200 iterative steps are considered for different amount of SNR in the transmit sensitivity of a quadrature birdcage coil. The vertical blue lines denote the intrinsic bias, namely the relative error in the estimation in absence of noise. The vertical red lines denote the extremes of the shortest 95 % coverage intervals of the approximated distributions.

constraint applied to the minimisation problem. It is worth noting that the mean value of the approximated distributions does not coincides exactly with 0 %. Instead, the distributions show a bias that is independent of the input SNR but depends on the number of iterations. Precisely, the intrinsic bias is the relative error committed by csiEPT in absence of noise. Since the point considered in Fig. 3.18 lies in an extended homogeneous region, in this case the intrinsic bias is quite low already after 100 iterations suggesting the convenience in stopping the iterative procedure after 100 steps in order to bound the uncertainty in the estimated properties.

Similarly, the relative frequency histograms for a pixel of a very narrow tissue are shown in Fig. 3.19. Besides the variance of the distributions increases with the number of iterations, the presence of a strong bias cannot be ignored in this situation. Thus, the uncertainty assessment benefits from the root mean square (RMS) statistic, which is defined as the sum of the square of the mean and the variance of the considered distribution. By this way, the error is quantified by taking into account both the deterministic bias and the stochastic variance. The RMS appears to decrease

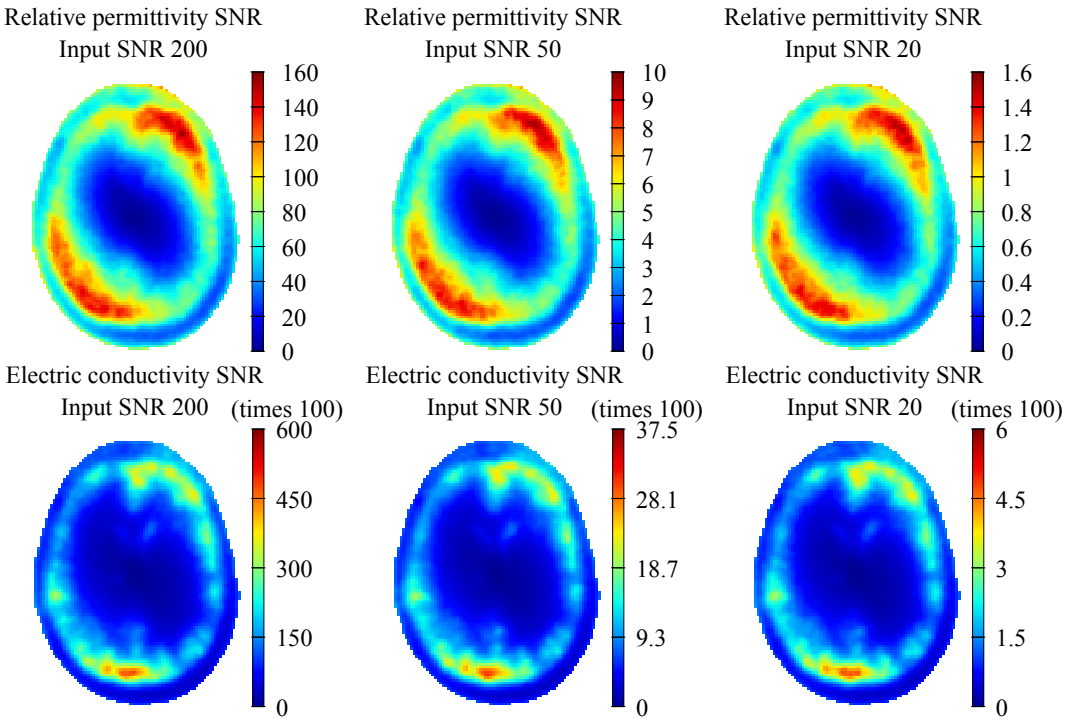

Fig. 3.20 Local SNR for the output properties after 100 iterative steps. Different input global SNR are considered.

when moving from 100 to 200 iterations only for the electric conductivity when the input SNR is the highest (equal to 200). For all the other cases, the reduction of bias is not strong enough to compensate the increase in the variance. Thus, also for this pixel, to stop the iterative procedure after 100 steps seems to be a convenient choice.

The comparison between Fig. 3.18 and Fig. 3.19 suggests a strong dependence of the result with respect to the spatial position. This fact is confirmed by Fig. 3.20, where the maps of the local SNR of the electric properties estimated after 100 iterative steps are collected for different input SNR. It results that the maximum local SNR depends quadratically on the input SNR and that its spatial distribution is independent of the input SNR. Actually, the author has shown in [121] that the spatial distribution of the SNR shows a strong correlation with the intensity of the total electric field. This observation can be seen as the statistical interpretation of the issue in the recovery of the properties by csiEPT in the minimum field intensity region. The quadratic fit holds also for the global SNR, which is equal to 62 for the relative permittivity and 11.8×10^3 for the electric conductivity when the input SNR is equal to 200. It is worth noting that, despite the global SNR in electric conductivity

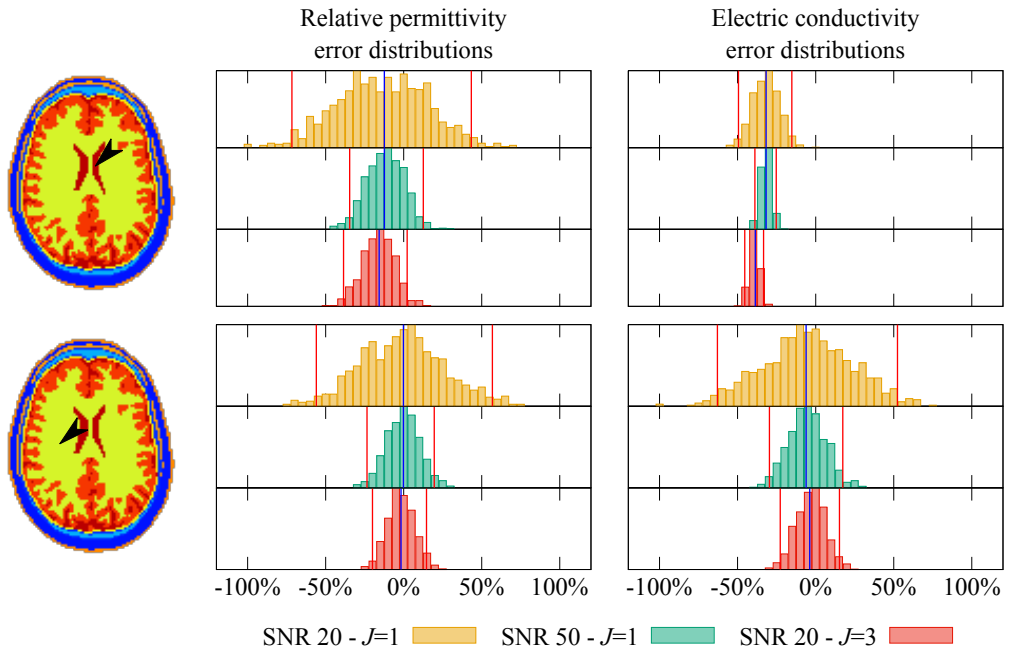

Fig. 3.21 Relative frequency histograms of the relative error of the estimated electric properties in the pixels (cerebrospinal fluid on top and white matter on bottom) indicated in the inset maps on the left. The properties recovered after 100 iterative steps are considered for different amount of SNR in the transmit sensitivity of a quadrature birdcage coil with different excitations. The vertical blue lines denote the intrinsic bias, namely the relative error in the estimation in absence of noise. The vertical red lines denote the extremes of the shortest 95 % coverage intervals of the approximated distributions.

is higher that the input SNR, the uncertainty is kept large by the strong bias, as can be seen in Fig. 3.19.

The adoption of multiple measurements obtained by employing three excitations of the birdcage coil strongly improves the estimation of the properties, as can be deduced from the relative frequency histograms of Fig. 3.21. Indeed, despite the noisy input with global SNR 20, the use of three measurements ($J = 3$) leads to coverage intervals narrower than the ones reached when the input SNR is equal to 50 and just a measurement of the transmit sensitivity is used ($J = 1$). Globally, the SNR is ten times higher than that obtained from $J = 1$ with input global SNR 20. Precisely, it is equal to 6.5 for the relative permittivity and 1.12×10^3 for the electric conductivity, which remains strongly biased in the small tissues.

3.4.3 Noise propagation from TEM coil measures

Since the advantage that has been proven above introduced by the adoption of measurements of multiple transmit sensitivities, the TEM coils, traditional multi-channel transmit coils, are studied in the following. The appearance of a volume TEM coil is very similar to that of a birdcage coil, but instead of using end-rings, each leg is usually joined to the conductive shield which plays the role of returning line [97]. Despite TEM coils are often driven in quadrature like birdcage coils, their design allows that each leg is driven independently from the other ones leading to as many possible excitations as the number of legs in the coil. This coil is modelled in a boundary-free domain by setting a second circle of line sources around an inner one analogous to that described for birdcage coils [121]. Each couple of lines, the inner and the corresponding outer, constitutes an independent system and reflects a possible excitation of the coil. Formally, assuming the presence of J legs numbered clockwise by $k = 1, \ldots, J$, the j-th excitation is assumed to have in the inner circle the currents

$$I_k^{\mathrm{TEM},j} = \delta_{j,k} I \mathrm{e}^{\mathrm{i}2\pi k/J}, \tag{3.76}$$

and in the outer circle the currents $-I_k^{\mathrm{TEM},j}$. In the latter relation, $\delta_{j,k}$ is the Kronecker delta, equal to one when $j = k$ and to zero otherwise. Thus, only one leg at the time is run by current.

TEM coils with inner radius 14 cm and outer radius 16 cm are analysed varying the number of legs J. Precisely, the cases with $J = 8$, 12, 16 and 24 legs are considered. The integral errors of both the electric properties fall very quickly and in a deterministic fashion—with narrow coverage intervals. The plot of the convergence is not reported because the trend of the errors for the four cases are overlaid and cannot be distinguished. Despite the minimum of the median global errors is not reached there, the procedure is stopped after 60 iterative steps because of the computational burden. It is worth noting that after 60 steps, the properties estimated in absence of noise with the 8-legs TEM coil are much more precise than that estimated after 100 steps with a quadrature birdcage coil; indeed, they are comparable with the properties estimated with a quadrature birdcage coil after 300 steps. In addition, the low field intensity issue of csiEPT, which is present also when using the birdcage coil with three excitations, is completely absent when using a TEM coil, probably because of the wide heterogeneity in the transmit sensitivities of the legs.

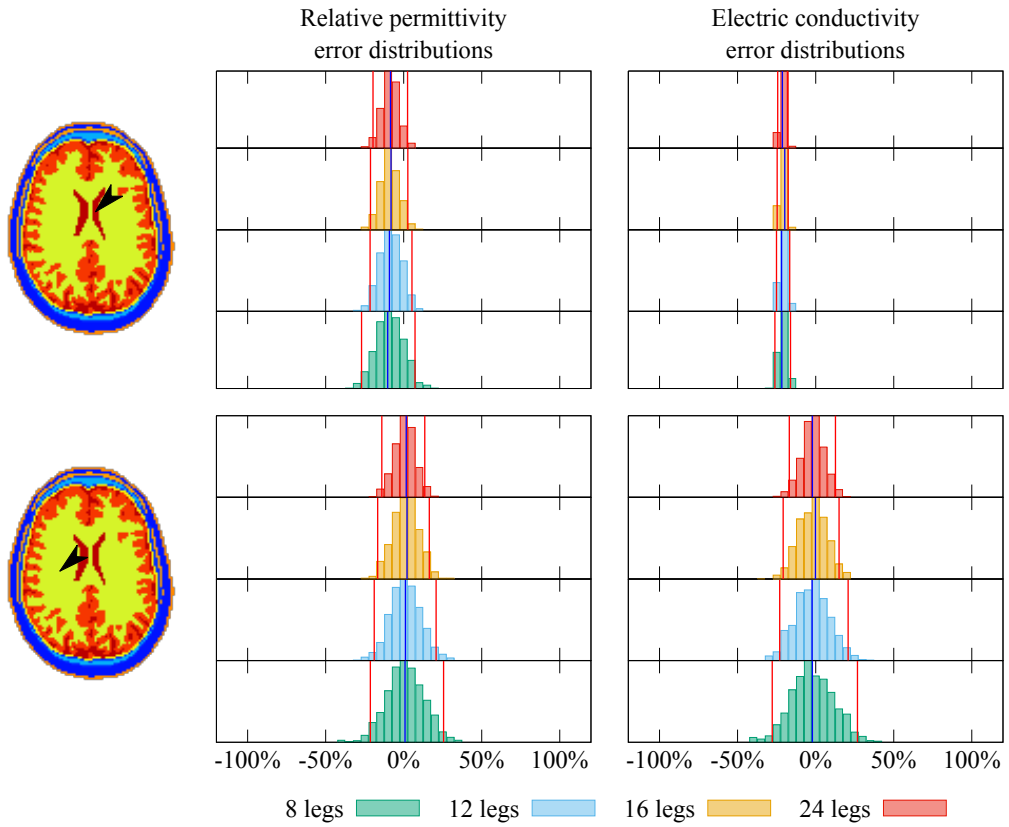

Fig. 3.22 Relative frequency histograms of the relative error of the estimated electric properties in the pixels (cerebrospinal fluid on top and white matter on bottom) indicated in the inset maps on the left. The properties recovered after 60 iterative steps are considered for TEM coils with different number of legs, and so of excitations. The input global SNR is equal to 20. The vertical blue lines denote the intrinsic bias, namely the relative error in the estimation in absence of noise. The vertical red lines denote the extremes of the shortest 95 % coverage intervals of the approximated distributions.

The relative frequency histograms of Fig. 3.22 represents the probability distribution of the relative error of the electric properties estimated in a couple of pixels. As already seen studying the birdcage coil, the error committed in the pixel in the middle of the wide tissue—white matter—has a larger variance than the error in the narrow tissue—cerebrospinal fluid. On the other hand, the error in the cerebrospinal fluid has a larger intrinsic bias than the one in the white matter. The approximated distributions are symmetric and centred around the value that would be estimated by csiEPT in absence of noise. This observation allows a precise estimation of the deterministic bias. As expected, the distributions get narrower with increasing the number of legs and so the corresponding number of input.

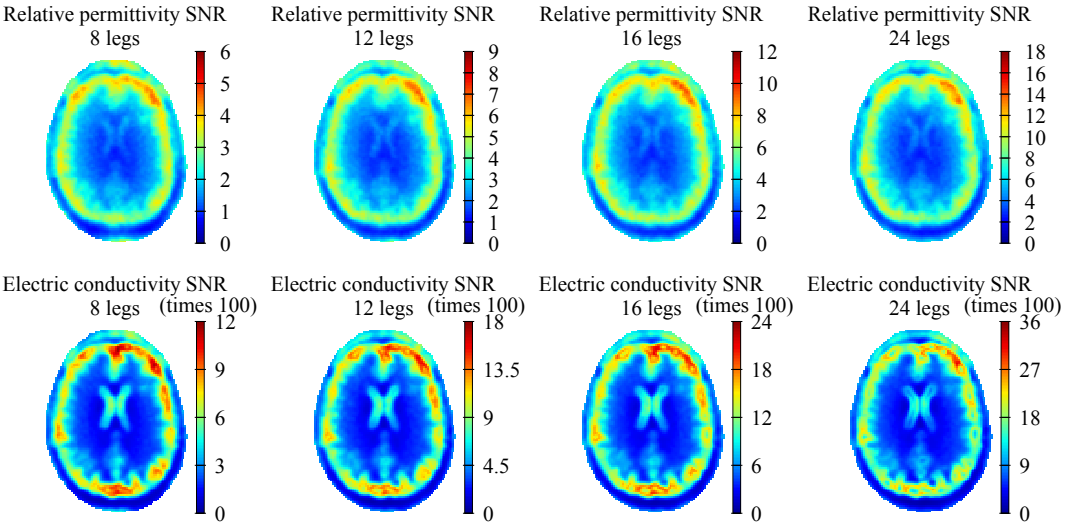

Fig. 3.23 Local SNR for the output properties after 60 iterative steps. The input global SNR is equal to 20. TEM coils with different number of legs are considered.

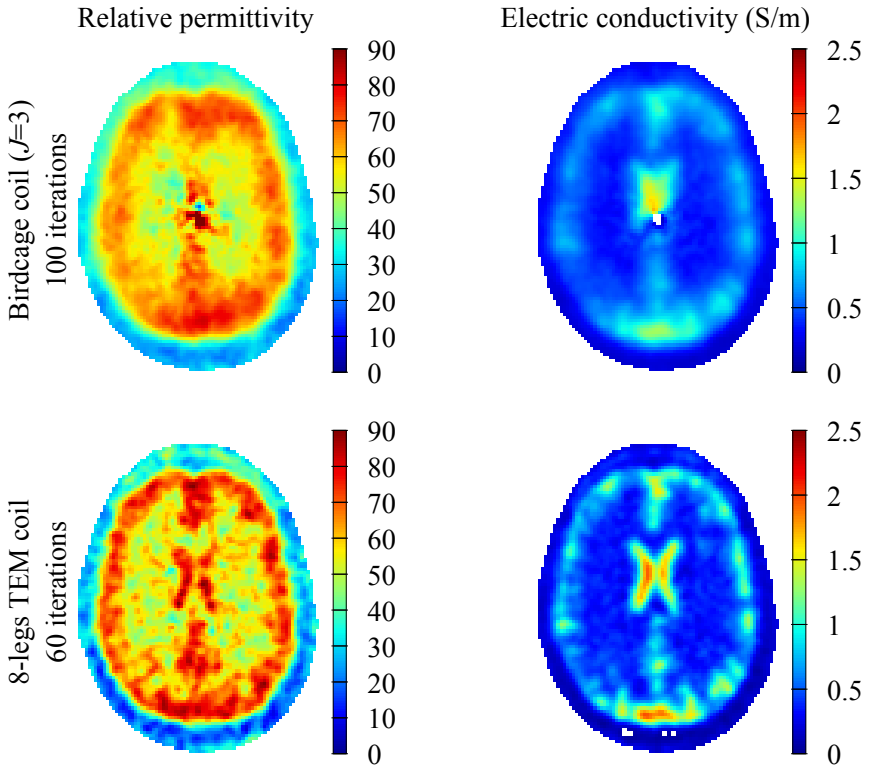

Fig. 3.24 Electric properties maps estimated by csiEPT from noisy virtual measurements of transmit sensitivities generated by a 16-legs birdcage coil with three excitations and an 8-leg TEM coil with 8 excitations. The input global SNR is equal to 20.

Looking at the histograms it appears that TEM coils reduce the width of relative error coverage intervals similarly to using three excitation for the birdcage coil. Actually, the advantage of using TEM coils is greater because of a lower spatial variability of the output SNR than the one achieved from birdcage coil measurements. This fact is clear in Fig. 3.23, where the SNR assumes everywhere a positive value and does not tend to zero in the inner region like happens in Fig. 3.20. The existence of a linear dependence of the output local SNR with respect to the number of legs is made clear by the varying extremes of the chromatic bars in Fig. 3.23. This linear tendency is found also in the global SNR, which in the case of 8 legs is equal to 2 for the relative permittivity and 375 for the electric conductivity. Despite these values are lower than that achieved by a birdcage coil with just three measurements, they are preferable because obtained as average values of more homogeneous maps.

The improvement in accuracy due to the adoption of multi-channel TEM coils can be appreciated more directly in the maps of Fig. 3.24, where the electric properties recovered starting from a couple of realisations of the virtual input measurements are reported. Despite the fewer number of iterative steps, the maps recovered from the transmit sensitivities of an 8-legs TEM coil are more detailed than the ones obtained elaborating the transmit sensitivities of a 16-legs birdcage coil with three excitations. In addition, there are no artefacts in the inner region of the estimations from the TEM coil. Clearly, the use of multiple measurements increases the computational cost of the minimisation procedure linearly with respect to the number of measurements J. However, the additional computational burden can be handled efficiently by code parallelisation, since all the expensive computations—relations (3.49), (3.51), (3.53) and (3.54)—can be parallelised trivially with respect to the setting index j. By this way, on a fully equipped hardware, csiEPT execution would be independent from the number J and the use of multiple measurements would not be a load.

These results show the convenience of applying csiEPT to multi-channel TEM coils because of the low number of required iterative steps, the absence of the minimum field intensity issue and the high SNR of the output, even without the adoption of sophisticated regularisation strategies. Thus, it seems feasible to apply csiEPT to local SAR monitoring during the optimal feed selection in pTX.

Chapter 4

Conclusions and future perspectives

In this thesis, the magnetic resonance-based electric properties tomography (MREPT) has been deeply investigated starting from a thorough review of the plethora of implementation approaches proposed in literature (cf. Chapter 2). In particular, several methods have been coded and applied to a simple two-dimensional model problem in order to illustrate their characteristics. The responsiveness of the very simple standard EPT (stdEPT) is countered by large systematic errors in the estimated electric properties [63]. A higher accuracy is achieved by the dual-excitation algorithm (deEPT) at the cost of more measurements and some requirements about the transmit coil [59]. An interesting trade-off between precision in the estimation and number of needed measurements is obtained by interpreting the electric properties as the solution of a convection-reaction partial differential equation (crEPT), the numerical solution of which is a significant computational burden [111]. A similar compromise is reached by csiEPT, which pursues an optimal control approach based on the contrast source inversion technique [74].

Amongst all the methods, csiEPT has been selected for further studies, reported in Chapter 3, because of the capability of this method to quantitatively estimate, besides the electric properties distributions, the local specific absorption rate (SAR) of the RF coil of the MRI scanner as a by-product [118, 134]. This characteristic opens the possibility to apply csiEPT for safety purposes, which are relevant, for example, in parallel transmission (pTX) or in ultra-high field MRI [135]. Thus, a generalised mathematical framework, based on the functional point of view, has been proposed for csiEPT [122]. Differently from the original proposal of the

method, this generalised framework can be easily adapted in order to apply csiEPT in different contexts. This flexibility has been exploited in the thesis to show the importance in csiEPT of an accurate modelling of the measurement system. In particular, virtual measurements have been produced simulating a RF birdcage coil in presence of a cylindrical conductive shield, usually present in practice, and csiEPT has been applied assuming both the presence and the absence of the shield. Predictably, taking into account the presence of the shield leads to estimations far more accurate by csiEPT [122]. Lastly, noise propagation through the inverse technique has been studied by means of the Monte Carlo method applied to a particular model problem—a section of the human head has been considered. Since MREPT is an ill-posed inverse problem, managing noisy input requires special cares, as described in Chapter 3. Anyway, it appears that csiEPT is highly robust to noise when RF multi-channel transmit coils—a typical instrument for pTX—are used [121]. This result is particularly interesting, because it suggests good performances of csiEPT in a context in which local SAR estimation is very important for safety purposes [135].

The analyses and the results collected in this thesis prove the convenience of further developing MREPT and in particular csiEPT. The next steps in order to make csiEPT ready for *in vivo* applications would be the development of a three-dimensional software implementation of the method, alongside the overcoming of the issues related to transmit sensitivity phase mapping. On the one hand, an efficient three-dimensional code for csiEPT can be achieved by exploiting special hardware, possibly involving accelerators like graphical processing units (GPUs), and parallel programming paradigms. On the other hand, special MRI sequences should be developed to map the transmit sensitivity phase without strong hypotheses—like the present transceive phase assumption. Or alternatively, the possibility of performing csiEPT with a partial knowledge of the transmit phase—or even without it—should be investigated, as was the case for deEPT and local Maxwell tomography (cf. Chapter 2). The proposed development of csiEPT would allow its application in real contexts, leading to the *in vivo* validation of the method as a final fundamental step. Because of the relevance of csiEPT in improving pTX and ultra high field MRI safety by leading to a real-time patient-specific local SAR evaluation, this method would likely have a positive impact on the clinical introduction of these advanced MRI equipments.

Appendix A

Magnetic resonance imaging

Magnetic resonance imaging (MRI) is a non-invasive technique able of producing images of sections of human bodies by measuring, in an effective sense that will be clarified in the following, the density of hydrogen nuclei—*i.e.*, protons—in the different tissues. In order to achieve this result, the patient is exposed to three different magnetic fields, whose task is to excite the hydrogen nuclei's spins and to make them rotate with certain time-varying space-dependent phases, such that the nuclear magnetic resonance (NMR) signal emitted by the body brings a retrievable spatial information [169, 35, 170]. The following is a rough description of the involved magnetic fields and their role in MRI (Fig. A.1):

i. The static field $\boldsymbol{B}_0$ produces a net orientation of the protons' spins and prepares them to rotate around its direction. The static field identifies a longitudinal direction with unit vector $\hat{\boldsymbol{z}}$ such that $\boldsymbol{B}_0 = -B_0\hat{\boldsymbol{z}}$, being B_0 the field magnitude. The induced spins' rotation is called Larmor precession and its frequency—called Larmor frequency—is proportional to B_0 [169]. In order to generate a static field as much as possible homogeneous in the imaging region, particular conductive/superconductive coils are used [171].

ii. The radiofrequency (RF) field $\boldsymbol{B}_1$ is orthogonal to the static field and has almost circular polarisation. Its purpose is to resonate with the Larmor precession in order to provide to the protons' spins the energy necessary to emit the NMR signal. Indeed, the RF field flips the spins from the longitudinal direction of $\boldsymbol{B}_0$ towards the transverse plane $\hat{\boldsymbol{x}} \otimes \hat{\boldsymbol{y}}$, being $\hat{\boldsymbol{x}}$, $\hat{\boldsymbol{y}}$ and $\hat{\boldsymbol{z}}$ the unit vectors of a Cartesian coordinate system. Thus, it actually triggers the Larmor

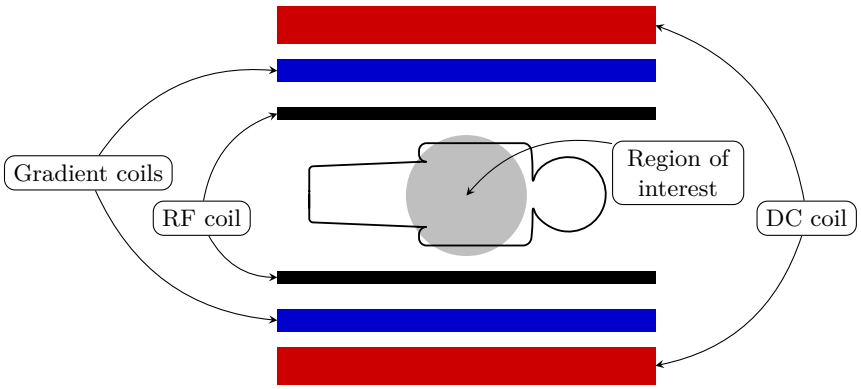

Fig. A.1 Schematic diagram of the coils which generate the three magnetic fields for MRI.

precession [169]. The RF field $\boldsymbol{B}_1$ is produced by special coils designed for MRI [97].

iii. The gradient field $\boldsymbol{B}^{\boldsymbol{G}}$ is directed as the static field, but it is spatially non-homogeneous—indeed, its name derives from its non-null spatial gradient. During a MRI examination, this field is turned on and off according to a certain sequence in order to make the spins rotate at different Larmor frequencies depending on their position in the body. In this way, each point in the body accumulates a different phase and the emitted NMR signal can be elaborated to retrieve this spatial information [169].

The principles of the MRI technology, which have been just outlined above, can be rigorously described relying on the phenomenological Bloch equations [172],

$$\begin{cases} \dot{M}_x = \gamma(M_y B_z - M_z B_y) - M_x/T_2 \\ \dot{M}_y = \gamma(M_z B_x - M_x B_z) - M_y/T_2 \\ \dot{M}_z = \gamma(M_x B_y - M_y B_x) - (M_z - M_0)/T_1 \end{cases} \tag{A.1}$$

which describe the evolution of the macroscopic magnetisation $\boldsymbol{M}$ due to protons' spins with gyromagnetic ratio $\gamma = 267.513 \times 10^6\,\mathrm{rad\,s^{-1}\,T^{-1}}$ when exposed to an external magnetic field $\boldsymbol{B}$, in which the static field $\boldsymbol{B}_0$ is the contribution with highest intensity. The relaxation times T_1 and T_2—called respectively spin-lattice and spin-spin relaxation times because mainly due to the interaction of the spins with the background and with the other spins—and the asymptotic magnetisation M_0 are the phenomenological terms added by Bloch to the macroscopic Larmor precession

equation [172]

$$\dot{\boldsymbol{M}} = \gamma \boldsymbol{M} \times \boldsymbol{B} \,. \tag{A.2}$$

A.1 Larmor equation and image recovery

To understand how the images are generated by the MRI scanners, it is convenient to neglect the relaxation effects and focus on the Larmor equation (A.2), which, in presence of the static field $\boldsymbol{B}_0 = -B_0\hat{\boldsymbol{z}}$ only, becomes

$$\dot{\boldsymbol{M}} = -\gamma B_0 \left(M_y \hat{\boldsymbol{x}} - M_x \hat{\boldsymbol{y}}\right) . \tag{A.3}$$

The transverse component of this vector equation can be treated as a complex scalar one by interpreting the transverse plane $\hat{\boldsymbol{x}} \otimes \hat{\boldsymbol{y}}$ as the complex Argand plane, namely by biunivocally associating the complex number $\underline{M}_\perp = M_x + \mathrm{i} M_y$, being i the imaginary unit such that $\mathrm{i}^2 = -1$, to the transverse vector $\boldsymbol{M}_\perp = M_x \hat{\boldsymbol{x}} + M_y \hat{\boldsymbol{y}}$. In the following, the underlined symbols denote complex numbers that have to be interpreted according to this description of the transverse plane—which is far from the usual definition of phasors! Thus, it is possible to write the evolution of the transverse component of the magnetisation as

$$\dot{\underline{M}}_\perp = \mathrm{i}\omega_0 \underline{M}_\perp \quad \Rightarrow \quad \underline{M}_\perp(t) = \underline{M}_{0,\perp} \mathrm{e}^{\mathrm{i}\omega_0 t} , \tag{A.4}$$

where $\omega_0 = \gamma B_0$ is the Larmor angular frequency and $\underline{M}_{0,\perp}$ is the transverse component of the initial condition. By definition of the complex exponential function, this relation depicts the counterclockwise precession of the magnetisation vector around the z-axis and is the basis of the signal emitted by the body during MRI examination.

Lemma A.1. *Let be* $\boldsymbol{A}(t) = A_x \cos(\omega t + \varphi_x)\hat{\boldsymbol{x}} + A_y \cos(\omega t + \varphi_y)\hat{\boldsymbol{y}}$ *a generic harmonic vector with angular frequency* ω*, and let be*

$$\begin{cases} \hat{\boldsymbol{x}}^+(t) = \quad \cos(\omega t)\hat{\boldsymbol{x}} + \sin(\omega t)\hat{\boldsymbol{y}} \\ \hat{\boldsymbol{y}}^+(t) = -\sin(\omega t)\hat{\boldsymbol{x}} + \cos(\omega t)\hat{\boldsymbol{y}} \end{cases} \qquad \begin{cases} \hat{\boldsymbol{x}}^-(t) = \cos(\omega t)\hat{\boldsymbol{x}} - \sin(\omega t)\hat{\boldsymbol{y}} \\ \hat{\boldsymbol{y}}^-(t) = \sin(\omega t)\hat{\boldsymbol{x}} + \cos(\omega t)\hat{\boldsymbol{y}} \end{cases}$$

two reference frames rotating at the same angular frequency ω *counterclockwise and clockwise, respectively. There exists one and only one description of* $\boldsymbol{A}$ *with respect to the four rotating axis with stationary coefficients.*

Proof. Existence and unicity of the coefficients are proven in a constructive way. Let be A_x^+, A_y^+, A_x^- and A_y^- the four unknown constant coefficients, then

$$\begin{aligned}\boldsymbol{A}(t) = &\left((A_x^+ + A_x^-)\cos(\omega t) + (A_y^- - A_y^+)\sin(\omega t)\right)\hat{\boldsymbol{x}} + \\ &\left((A_x^+ - A_x^-)\sin(\omega t) + (A_y^- + A_y^+)\cos(\omega t)\right)\hat{\boldsymbol{y}}\,.\end{aligned}$$

At the same time,

$$\begin{aligned}\boldsymbol{A}(t) = &\left(A_x\cos(\varphi_x)\cos(\omega t) - A_x\sin(\varphi_x)\sin(\omega t)\right)\hat{\boldsymbol{x}} + \\ &\left(A_y\cos(\varphi_y)\cos(\omega t) - A_y\sin(\varphi_y)\sin(\omega t)\right)\hat{\boldsymbol{y}}\,.\end{aligned}$$

Since $\hat{\boldsymbol{x}}$ and $\hat{\boldsymbol{y}}$ are linearly independent vectors and $\cos(\omega t)$ and $\sin(\omega t)$ are linearly independent functions, the two equalities lead to a non-singular linear system of four equations in four unknowns whose solution is

$$\begin{aligned}A_x^+ &= \left(A_x\cos(\varphi_x) - A_y\sin(\varphi_y)\right)/2\,, & A_y^+ &= \left(A_y\cos(\varphi_y) + A_x\sin(\varphi_x)\right)/2\,,\\ A_x^- &= \left(A_x\cos(\varphi_x) + A_y\sin(\varphi_y)\right)/2\,, & A_y^- &= \left(A_y\cos(\varphi_y) - A_x\sin(\varphi_x)\right)/2\,.\end{aligned}$$

♦

Lemma A.2. *Let $\boldsymbol{A}(t) = A_x^+\hat{\boldsymbol{x}}^+(t) + A_y^+\hat{\boldsymbol{y}}^+(t) + A_x^-\hat{\boldsymbol{x}}^-(t) + A_y^-\hat{\boldsymbol{y}}^-(t)$ be a generic harmonic vector whose components are defined as in lemma A.1, and let $\overline{\boldsymbol{A}} = \overline{A}_x\hat{\boldsymbol{x}} + \overline{A}_y\hat{\boldsymbol{y}}$ be its phasor. The following relations hold,*

$$\underline{A}^+ = \left(\overline{A}_x + \mathrm{i}\overline{A}_y\right)/2\,, \qquad \underline{A}^- = \left(\overline{A}_x - \mathrm{i}\overline{A}_y\right)^*/2\,,$$

where $\underline{A}^+ = A_x^+ + \mathrm{i}A_y^+$ and $\underline{A}^- = A_x^- + \mathrm{i}A_y^-$ are respectively the positively and the negatively rotating components in the rotating Argand planes, and the asterisk denotes the complex conjugation.

Proof. The thesis derives straightforward from the proof of lemma A.1. ♦

As expected, the transverse component of the magnetisation has only the counterclockwise—or positively—rotating component at the Larmor frequency, $\boldsymbol{M}_\perp = \boldsymbol{M}_\perp^+ = M_{\perp,x}^+\hat{\boldsymbol{x}}^+ + M_{\perp,y}^+\hat{\boldsymbol{y}}^+$. Relation (A.4) can also be written in the rotating frame as $\underline{M}_\perp^+ = \underline{M}_{0,\perp} = M_{0,\perp}\mathrm{e}^{\mathrm{i}\varphi_0}$, being $M_{0,\perp}$ the magnitude of the transverse component.

Experimental observations and quantum mechanical considerations—as well as the phenomenological Bloch equations—show that the application of a strong static field induces a net magnetisation $\boldsymbol{M}_0$ directed as the static field itself and proportional

to both the static field $\boldsymbol{B}_0$ and the proton density [169, 170]. Thus no precession happens, because, despite the transverse component of the magnetisation would rotate around $\boldsymbol{B}_0$, initially only the z-component is present. In order to provide a non-null transverse magnetisation, the RF field $\boldsymbol{B}_1$ is introduced. To clearly understand its effect, it is convenient to describe the Larmor precession in the positively rotating reference frame at the Larmor frequency defined by the unit vectors $\hat{\boldsymbol{x}}^+$, $\hat{\boldsymbol{y}}^+$ and $\hat{\boldsymbol{z}}$. In this case

$$\dot{\boldsymbol{M}} = \underbrace{\frac{\partial M_x^+}{\partial t}\hat{\boldsymbol{x}}^+ + \frac{\partial M_y^+}{\partial t}\hat{\boldsymbol{y}}^+ + \frac{\partial M_z}{\partial t}\hat{\boldsymbol{z}}}_{\text{Eulerian derivative}} + \underbrace{M_x^+\frac{\partial \hat{\boldsymbol{x}}^+}{\partial t} + M_y^+\frac{\partial \hat{\boldsymbol{y}}^+}{\partial t}}_{\text{Fictitious transport term}} . \tag{A.5}$$

By computing the time derivatives of the rotating basis vectors, it is easy to show that the fictitious transport term is equal to $\gamma\boldsymbol{M}\times\boldsymbol{B}_0$. Thus, denoting the Eulerian derivative by $(\partial\boldsymbol{M}/\partial t)^+$, the Larmor equation in presence of both the static and the RF fields in the positively rotating frame is

$$\left(\frac{\partial \boldsymbol{M}}{\partial t}\right)^+ = \gamma\boldsymbol{M}\times\boldsymbol{B}_1 . \tag{A.6}$$

The RF coils for MRI are designed to generate $\boldsymbol{B}_1$ in the transverse plane as an almost positively rotating field at the Larmor frequency. Moreover, in equation (A.6) the negatively rotating component of $\boldsymbol{B}_1$ would have an apparent frequency equal to the double of the Larmor frequency—fast enough to be neglected. Thus, it is possible to assume that only $\boldsymbol{B}_1^+$, which is stationary in the rotating frame, plays a role in (A.6) [35]. In the same way as for the precession around the static field, the RF component $\boldsymbol{B}_1^+$ makes the magnetisation vector rotate around its direction at the angular frequency $\omega_1 = \gamma B_1^+$, providing the transverse component $\underline{M}_{0,\perp}$. The magnitude of the RF field is denoted by B_1^+.

Precisely, after an exposure to the RF field of duration τ, the magnetisation vector forms an angle, usually called flip angle, $\alpha = \omega_1\tau$ with its previous direction. Assuming $\boldsymbol{M}(0) = -M_0\hat{\boldsymbol{z}}$ as an initial condition, the transverse component induced by $\underline{B}_1^+ = B_1^+ \mathrm{e}^{\mathrm{i}\vartheta}$ is obtained by simple trigonometric considerations [35],

$$\underline{M}_{0,\perp} = \mathrm{i}M_0 \sin\left(\gamma B_1^+\tau\right)\frac{\underline{B}_1^+}{B_1^+} . \tag{A.7}$$

By rotating the magnetisation towards the transverse plane, the RF field—in particular its positively rotating part—gives to the protons the energy that they need to revolve around $\boldsymbol{B}_0$ and, consequently, to emit a signal. Clearly, the largest transverse magnetisation is reached by the optimum flip angle $\alpha = \pi/2$ and the exposure time τ needs to be carefully set.

Before introducing the gradient field $\boldsymbol{B}^{\boldsymbol{G}}$, it is convenient to see what the measured signal is by exploiting the reciprocity principle [173, 170]. The magnetic field $\boldsymbol{B}^{\boldsymbol{M}}$ due to the magnetisation $\boldsymbol{M}$ can be expressed as the solution of the equation

$$\nabla \times \boldsymbol{B}^{\boldsymbol{M}} = \nabla \times \boldsymbol{M}\,, \tag{A.8}$$

where the conduction and displacement currents have been neglected [173]. The equation is solved by the Biot-Savart formula

$$\begin{aligned} \boldsymbol{B}^{\boldsymbol{M}}(\boldsymbol{x},t) &= \mu_0\, \nabla_{\boldsymbol{x}} \times \int_{\mathbb{R}^3} \nabla_{\boldsymbol{y}} \times \big(\boldsymbol{M}(\boldsymbol{y},t)\big)\, \psi(\boldsymbol{x}-\boldsymbol{y})\, \mathrm{d}V(\boldsymbol{y}) \\ &= \mu_0\, \nabla_{\boldsymbol{x}} \times \int_{\mathbb{R}^3} \nabla_{\boldsymbol{x}} \psi(\boldsymbol{x}-\boldsymbol{y}) \times \boldsymbol{M}(\boldsymbol{y},t)\, \mathrm{d}V(\boldsymbol{y})\,, \end{aligned} \tag{A.9}$$

where $\psi(\boldsymbol{r})$ is the Green's function of the Laplace problem in free space with Sommerfeld radiation conditions. The last equality in (A.9) can be proven applying the Green's identities and noticing that the integral on the boundary is null because $\operatorname{supp}(\boldsymbol{M}(\cdot,t)) = \Omega \subset \mathbb{R}^3$ is bounded at each instant t, being Ω the volume occupied by the examined body. According to Faraday's law, the difference of potential at the terminals of a generic coil ∂A induced by the magnetisation is

$$\begin{aligned} \mathscr{V}(t) &= -\oint_{\partial A} \boldsymbol{E}^{\boldsymbol{M}}(\boldsymbol{x},t) \cdot \mathrm{d}\boldsymbol{l}(\boldsymbol{x}) = \int_A \frac{\partial \boldsymbol{B}^{\boldsymbol{M}}}{\partial t}(\boldsymbol{x},t) \cdot \mathrm{d}\boldsymbol{S}(\boldsymbol{x}) \\ &= \oint_{\partial A} \left(\mu_0 \int_{\mathbb{R}^3} \nabla_{\boldsymbol{x}} \psi(\boldsymbol{x}-\boldsymbol{y}) \times \frac{\partial \boldsymbol{M}}{\partial t}(\boldsymbol{y},t)\, \mathrm{d}V(\boldsymbol{y}) \right) \cdot \mathrm{d}\boldsymbol{l}(\boldsymbol{x})\,, \end{aligned} \tag{A.10}$$

where Stokes' theorem has been exploited in the last step. Finally, by inverting the order of integration, it is possible to write the electromotive force in the coil as

$$\mathscr{V}(t) = \int_{\mathbb{R}^3} \frac{\partial \boldsymbol{M}}{\partial t}(\boldsymbol{y},t) \cdot \tilde{\boldsymbol{B}}(\boldsymbol{y})\, \mathrm{d}V(\boldsymbol{y})\,, \tag{A.11}$$

where $\tilde{\boldsymbol{B}}$ denotes the magnetic field that would be induced by a fictitious unitary current running in ∂A,

$$\tilde{\boldsymbol{B}}(\boldsymbol{y}) = -\mu_0 \oint_{\partial A} \nabla_{\boldsymbol{x}} \psi(\boldsymbol{x}-\boldsymbol{y}) \times \mathrm{d}\boldsymbol{l}(\boldsymbol{x}) \,. \tag{A.12}$$

The relation (A.11), due to David Hoult [174, 175], is a milestone in MRI history and is usually referred to as an example of the reciprocity principle [35, 170]. Exploiting the harmonic dependence of $\boldsymbol{M}$ on time, (A.11) can be derived in a more general framework, where $\tilde{\boldsymbol{B}}$ denotes the ratio between the field generated by the receiver in presence of the examined body and the current which induces it [176]—in this case no approximations are performed. Under the assumption that the magnetisation in each point of the body Ω is given by (A.4), that is equivalent to

$$\boldsymbol{M}(\boldsymbol{y},t) = \mathrm{Re}\left(-(\mathrm{i}\hat{\boldsymbol{x}} + \hat{\boldsymbol{y}})\, \mathrm{i}\underline{M}_{0,\perp}(\boldsymbol{y}) \mathrm{e}^{\mathrm{i}\omega_0 t} \right) , \tag{A.13}$$

the electromotive force in the coil is

$$\mathscr{V}(t) = -\omega_0 \mathrm{Re}\left(\int_{\mathbb{R}^3} \mathrm{i}\underline{M}_{0,\perp}(\boldsymbol{y}) \left(\tilde{B}_x(\boldsymbol{y}) - \mathrm{i}\tilde{B}_y(\boldsymbol{y}) \right) \mathrm{e}^{\mathrm{i}\omega_0 t} \, \mathrm{d}V(\boldsymbol{y}) \right) . \tag{A.14}$$

Interpreting $\tilde{\boldsymbol{B}}$ as the phasor of the magnetic field induced by a unitary harmonic current in the coil as in [176], by lemma A.2 it is possible to recognise $2\underline{\tilde{B}}^{-,*} = \tilde{B}_x - \mathrm{i}\tilde{B}_y$ in (A.14). The electromotive force can be measured and elaborated in a couple of channels—the real and the imaginary one—by means of demodulation and filtering in order to view it from the rotating reference frame at the Larmor frequency [170]. The two channels are combined in the complex signal

$$\mathfrak{s}(t) = \omega_0 \int_{\mathbb{R}^3} M_{0,\perp}(\boldsymbol{y}) \tilde{B}^-(\boldsymbol{y}) \mathrm{e}^{\mathrm{i}(\tilde{\vartheta}^-(\boldsymbol{y}) - \varphi_0(\boldsymbol{y}))} \mathrm{e}^{\mathrm{i}(\omega_0 t - \phi(\boldsymbol{y},t))} \, \mathrm{d}V(\boldsymbol{y}) \,, \tag{A.15}$$

where $\underline{\tilde{B}}^- = \tilde{B}^- \mathrm{e}^{\mathrm{i}\tilde{\vartheta}^-}$ and $\phi(\boldsymbol{y},t)$ is the whole phase accumulated by the transverse component of the magnetisation according to Bloch equations—if only the static field is present, $\phi(\boldsymbol{y},t) = \omega_0 t$. The images generated by MRI scanners are maps of the quantity

$$\mathfrak{m}(\boldsymbol{y}) = \omega_0 M_{0,\perp}(\boldsymbol{y}) \tilde{B}^-(\boldsymbol{y}) \mathrm{e}^{\mathrm{i}\left(\tilde{\vartheta}^-(\boldsymbol{y}) - \varphi_0(\boldsymbol{y})\right)} \,, \tag{A.16}$$

a kind of effective spin density [170]. It is worth noting that the map $\mathfrak{m}(\boldsymbol{y})$ is affected by both the positively rotating component $\underline{B}_1^+$ of the RF field and the clockwise—or

negatively—rotating component $\underline{\tilde{B}}^{-}$ of the normalised field that the receiver coil would generate in presence of a harmonic current. For this reason, they are called transmit and receive sensitivity of the MRI scanner, respectively.

Finally, the gradient field $\boldsymbol{B}^{\boldsymbol{G}}$ is introduced in order to make the phase accumulation $\phi(\boldsymbol{y},t)$ vary in space in such a way to make equation (A.15) invertible with respect to $\mathfrak{m}(\boldsymbol{y})$. It is a time-varying magnetic field parallel to $\boldsymbol{B}_0$ which varies linearly with the position, and so it is completely defined by its gradient $\boldsymbol{G}(t)$

$$\boldsymbol{B}^{\boldsymbol{G}}(\boldsymbol{y},t) = (\boldsymbol{G}(t)\cdot\boldsymbol{r}(\boldsymbol{y}))\,\hat{\boldsymbol{z}}\,, \tag{A.17}$$

where $\boldsymbol{r}(\boldsymbol{y})$ is the vector distance of point $\boldsymbol{y}$ from the isocentre of the MRI scanner. For convenience, in the following the isocentre is assumed to coincide with the origin of the reference system, therefore $\boldsymbol{r}(\boldsymbol{y}) = \boldsymbol{y}$. Usually, the gradient field is turned on after the exposure to the RF field, so the Larmor precession of the magnetisation happens at angular frequency $\omega(\boldsymbol{y},t)$ depending on space and time. The resulting phase accumulation is

$$\phi(\boldsymbol{y},t) = \int_0^t \omega(\boldsymbol{y},t')\,\mathrm{d}t' = \omega_0 t + \gamma\left(\int_0^t \boldsymbol{G}(t')\,\mathrm{d}t'\right)\cdot\boldsymbol{y}\,. \tag{A.18}$$

In the common case of two-dimensional imaging, G_z is switched on simultaneously with the RF field in order to excite a particular slice of the body only. In equation (A.15), the contribution to the angular frequency due to the gradient field has been neglected in the multiplying factor, because the variation in the Larmor frequency induced by the gradient field is very small (at most a few hundred kilohertz) if compared with the carrier frequency of the static field (from 64 MHz for 1.5 T scanners up to 300 MHz for 7 T scanners) [170]. Nonetheless, this variation cannot be neglected in the phase of the signal. Introducing the spatial frequency

$$\boldsymbol{k}(t) = \frac{\gamma}{2\pi}\int_0^t \boldsymbol{G}(t')\,\mathrm{d}t'\,, \tag{A.19}$$

the complex demodulated signal (A.15) can be written as

$$\mathfrak{s}(\boldsymbol{k}(t)) = \int_{\mathbb{R}^3} \mathfrak{m}(\boldsymbol{y})\mathrm{e}^{-\mathrm{i}2\pi\boldsymbol{k}(t)\cdot\boldsymbol{y}}\,\mathrm{d}\boldsymbol{y}\,, \tag{A.20}$$

which describes $\mathfrak{s}(\boldsymbol{k}(t))$ as the Fourier transform of $\mathfrak{m}(\boldsymbol{y})$. Thus, the inverse Fourier transform can be employed to recover the desired image,

$$\mathfrak{m}(\boldsymbol{y}) = \int_{\mathbb{R}^3} \mathfrak{s}(\boldsymbol{k}) \mathrm{e}^{2\pi \boldsymbol{k}\cdot\boldsymbol{y}} \, \mathrm{d}\boldsymbol{k} \,. \tag{A.21}$$

In order to compute the inverse Fourier transform, $\mathfrak{s}(\boldsymbol{k}(t))$ must be sampled in the so-called k-space by turning on and off the three components of the gradient field according to a predefined sequence [169, 35, 170]. Often, the inverse Fourier transform is performed in two dimensions. This is made possible by turning on the z-component of the gradient field during the exposure to the RF field, which in this way resonates with only a slice of the body.

Sequence design is an important field in MRI, since the choice of an optimal path in the k-space can save time and power consumption. Moreover, the sequences must be designed taking into account the relaxations described by the phenomenologically corrected Bloch equations (A.1)—neglected in this description where the easier Larmor equation (A.2) has been used. Despite the many results achieved exploiting Bloch equations, certain cases may require models that are more difficult. For example, in presence of protons diffusion by Brownian motion in a fluid, the Bloch-Torrey equations must be used to describe the magnetisation vector evolution [177].

The elaboration of the complex map $\mathfrak{m}(\boldsymbol{y})$ measured by the MRI scanner can lead to the knowledge of physical quantities inside the human body. Some examples are described in the following.

A.2 Current density imaging

As mentioned in Chapter 1, the quasi-static current density induced in a sample by an external source is obtained by applying Ampère's law to the induced magnetic field $\boldsymbol{H}$, whose longitudinal component H_z can be measured with the MRI. Rotation of the sample in the scanner would lead to the whole knowledge of $\boldsymbol{H}$ [38]. If the current density is induced with a pulse of duration T_c after the RF excitation of the hydrogen nuclei's spin but before the motion in the k-space due to the gradient field, the spins experience an additional dephasing proportional to H_z and the measured

effective spin density reads

$$\mathfrak{m}^+(\boldsymbol{y}) = \omega_0 M_{0,\perp}(\boldsymbol{y})\tilde{B}^-(\boldsymbol{y})\mathrm{e}^{\mathrm{i}\left(\tilde{\vartheta}^-(\boldsymbol{y})-\varphi_0(\boldsymbol{y})-\gamma\mu_0 H_z(\boldsymbol{y})T_\mathrm{c}\right)}. \tag{A.22}$$

Likewise, if the opposite current density is induced, the magnetic field is $-\boldsymbol{H}$ and the measured signal is

$$\mathfrak{m}^-(\boldsymbol{y}) = \omega_0 M_{0,\perp}(\boldsymbol{y})\tilde{B}^-(\boldsymbol{y})\mathrm{e}^{\mathrm{i}\left(\tilde{\vartheta}^-(\boldsymbol{y})-\varphi_0(\boldsymbol{y})+\gamma\mu_0 H_z(\boldsymbol{y})T_\mathrm{c}\right)}. \tag{A.23}$$

Since

$$\frac{\mathfrak{m}^-(\boldsymbol{y})}{\mathfrak{m}^+(\boldsymbol{y})} = \mathrm{e}^{2\gamma\mu_0 H_z(\boldsymbol{y})T_\mathrm{c}}, \tag{A.24}$$

the longitudinal component of the magnetic field can be easily recovered from the difference of the obtained phase maps [38, 37].

A.3 B1-mapping

Many methods have been proposed to measure the magnitude B_1^+ of the RF field [53–57]. The easiest one, although not the most efficient, is the *double-angle method* proposed in [53]. It requires the production of two images of the same object obtained employing first the flip angle $\alpha = \gamma B_1^+ \tau$, then the double flip angle 2α. Since the measured complex map is

$$\mathfrak{m}(\boldsymbol{y},\alpha) = \omega_0 M_{0,\perp}(\boldsymbol{y},\alpha)\tilde{B}^-(\boldsymbol{y})\mathrm{e}^{\mathrm{i}\left(\tilde{\vartheta}^-(\boldsymbol{y})-\varphi_0(\boldsymbol{y},\alpha)\right)}, \tag{A.25}$$

where the dependence on the flip angle has been made explicit, the ratio of the magnitude of the two images is

$$\frac{M_{0,\perp}(\boldsymbol{y},2\alpha)}{M_{0,\perp}(\boldsymbol{y},\alpha)} = \frac{\sin\left(2\gamma B_1^+\tau\right)}{\sin\left(\gamma B_1^+\tau\right)} = 2\cos\left(\gamma B_1^+\tau\right). \tag{A.26}$$

This relation, which is directly obtained from (A.7), can be easily inverted with respect to B_1^+ under the assumption that the flip angle does not exceed $\pi/2$. Other techniques, like Bloch-Siegert shift methods [56, 57], rely on the phase of the complex map instead of its magnitude in order to obtain more accurate estimations.

The phase of $\underline{B}_1^+$ is more difficult to be recovered. Up to now, only few articles have explicitly dealt with this task, which is of fundamental importance in electric properties tomography [60, 61]. The only strategy based on traditional MRI scanners relies on the particular choice of a transmit and receive coil, like the birdcage coil, which allows to switch the polarisation between transmission and reception [58]. In this way, transmit and receive sensitivity would have almost opposite phases and so

$$\mathfrak{m}(\boldsymbol{y}) \cong \omega_0 M_{0,\perp}(\boldsymbol{y})\tilde{B}^-(\boldsymbol{y})\mathrm{e}^{-\mathrm{i}2\phi_0}\,, \tag{A.27}$$

where ϕ_0 is the phase of $\underline{B}_1^+$ as can be deduced from (A.7). The phase of the map $\mathfrak{m}(\boldsymbol{y})$ achieved by the polarisation switching is usually called transceive phase and the hypothesis that it coincides with the double of the transmit phase is called transceive phase assumption [64].

Appendix B

Elements of mathematics

Some basic knowledges of linear algebra, real analysis and topology are necessary in order to benefit from the following. A more detailed description of the topics treated in this appendix can be found, for example, in [154, 178].

B.1 Functional analysis

Definition B.1. A complete normed linear space $\mathbb{U}$, whose norm is denoted by $\|\cdot\|_{\mathbb{U}}$, is said to be a *Banach space*. Iff the norm is induced by a scalar product $(\cdot|\cdot)_{\mathbb{U}}$, then $\mathbb{U}$ is said to be a *Hilbert space*.

Definition B.2. A subset $A \subset \mathbb{U}$ of the Banach space $\mathbb{U}$ is said to be *bounded* iff there exists a positive constant $M > 0$ such that $\|u\|_{\mathbb{U}} < M$ for any $u \in \mathbb{U}$.

Definition B.3. A linear operator $T : \mathbb{U} \to \mathbb{V}$ between the Banach spaces $\mathbb{U}$ and $\mathbb{V}$ is said to be *bounded* iff for any bounded subset $A \subset \mathbb{U}$ its image $T(A) \subset \mathbb{V}$ is bounded.

Definition B.4. A linear operator $T : \mathbb{U} \to \mathbb{V}$ between the Banach spaces $\mathbb{U}$ and $\mathbb{V}$ is said to be *continuous in* $u_0 \in \mathbb{U}$ iff for any positive constant $\varepsilon > 0$ there exists a positive constant $\delta > 0$ such that $\|u - u_0\|_{\mathbb{U}} < \delta \Rightarrow \|Tu - Tu_0\|_{\mathbb{V}} < \varepsilon$.

Theorem B.5. *If the linear operator $T : \mathbb{U} \to \mathbb{V}$ between the Banach spaces $\mathbb{U}$ and $\mathbb{V}$ is continuous in $u_0 \in \mathbb{U}$, then it is continuous everywhere in $\mathbb{U}$.*

Proof. Since T is linear, for any $u, u_1 \in \mathbb{U}$

$$\|Tu - Tu_1\|_{\mathbb{V}} = \|Tu + T(u_0 - u_1) - T(u_0 - u_1) - Tu_1\|_{\mathbb{V}} = \|T(u - u_1 + u_0) - Tu_0\|_{\mathbb{V}}\,.$$

Since T is continuous in u_0, for any positive constant $\varepsilon > 0$ there exists a positive constant $\delta > 0$ such that

$$\|(u-u_1+u_0)-u_0\|_{\mathbb{U}} = \|u-u_1\|_{\mathbb{U}} < \delta \quad \Rightarrow \\ \|T(u-u_1+u_0)-Tu_0\|_{\mathbb{V}} = \|Tu-Tu_1\|_{\mathbb{V}} < \varepsilon\,.$$

♦

Theorem B.6. *For a linear operator $T : \mathbb{U} \to \mathbb{V}$ between the Banach spaces $\mathbb{U}$ and $\mathbb{V}$, the conditions of being bounded and being continuous are equivalent.*

Proof. If T is continuous, then it is continuous in $0 \in \mathbb{U}$, namely for any positive constant $\varepsilon > 0$ there exists a positive constant $\delta > 0$ such that $\|u\|_{\mathbb{U}} < \delta \Rightarrow \|Tu\|_{\mathbb{V}} < \varepsilon$. Let us consider a bounded subset $A \subset \mathbb{U}$ such that $u \in A \Rightarrow \|u\|_{\mathbb{U}} < M$, where $M > 0$ is a positive constant, then

$$u \in A \quad \Rightarrow \quad \left\| \frac{\delta}{M} u \right\|_{\mathbb{U}} < \delta \quad \Rightarrow \quad \|Tu\|_{\mathbb{V}} = \frac{M}{\delta} \left\| T\left(\frac{\delta}{M} u \right) \right\|_{\mathbb{V}} < \frac{M}{\delta} \varepsilon\,,$$

namely $T(A)$ is bounded.

Vice versa, if T is bounded, then for any $u \in \mathbb{U} \setminus \{0\}$

$$\|Tu\|_{\mathbb{V}} = \|u\|_{\mathbb{U}} \left\| T\left(\frac{u}{\|u\|_{\mathbb{U}}} \right) \right\|_{\mathbb{V}} < M \|u\|_{\mathbb{U}}\,,$$

for a positive constant $M > 0$, because $u/\|u\|_{\mathbb{U}} = 1 < 2$ denotes a bounded set. Thus, for any positive constant $\varepsilon > 0$, $\delta = \varepsilon/M > 0$ is such that $\|u\|_{\mathbb{U}} < \delta \Rightarrow \|Tu\|_{\mathbb{V}} < M\|u\|_{\mathbb{U}} < \varepsilon$. ♦

The following concept of adjoint operators could be introduced for operators between Banach spaces. However, for sake of simplicity, here it is described for operators between Hilbert spaces.

Definition B.7. For any linear operator $T : \mathbb{U} \to \mathbb{V}$ between the Hilbert spaces $\mathbb{U}$ and $\mathbb{V}$, the *adjoint operator* $T^\star : \mathbb{V} \to \mathbb{U}$ is defined such that for any $u \in \mathbb{U}$ and $v \in \mathbb{V}$,

$$(v|Tu)_{\mathbb{V}} = (T^\star v|u)_{\mathbb{U}}\,.$$

Theorem B.8. *The following properties hold:*

i. The adjoint operator of the composition of two linear operators $T : \mathbb{U} \to \mathbb{V}$ and $S : \mathbb{V} \to \mathbb{W}$ between Hilbert spaces is the composition of the adjoint operators

$T^\star : \mathbb{V} \to \mathbb{U}$ *and* $S^\star : \mathbb{W} \to \mathbb{V}$ *in reverse order*

$$(ST)^\star = T^\star S^\star .$$

ii. *The adjoint operator of the inverse of a linear operator* $T : \mathbb{U} \to \mathbb{V}$ *between Hilbert spaces is the inverse of the adjoint operator* $T^\star : \mathbb{V} \to \mathbb{U}$

$$\left(T^{-1}\right)^\star = (T^\star)^{-1} .$$

Proof. The properties are proven in order:

i. From the definition of adjoint operator it derives that for any $u \in \mathbb{U}$ and $w \in \mathbb{W}$

$$(w|STu)_{\mathbb{W}} = (S^\star w|Tu)_{\mathbb{V}} = (T^\star S^\star w|u)_{\mathbb{U}} .$$

ii. Since the composition $T^{-1}T = I$ is the identity operator and $(T^{-1}T)^\star = T^\star (T^{-1})^\star$, then for any $u_1, u_2 \in \mathbb{U}$

$$(u_1|u_2)_{\mathbb{U}} = \left(u_1|T^{-1}Tu_2\right)_{\mathbb{U}} = \left(T^\star \left(T^{-1}\right)^\star u_1|u_2\right)_{\mathbb{U}} .$$

Given the generality of $u_2 \in \mathbb{U}$, it follows that for any $u_1 \in \mathbb{U}$

$$T^\star \left(T^{-1}\right)^\star u_1 = u_1 ,$$

or equivalently $T^\star \left(T^{-1}\right)^\star = I$.

♦

Definition B.9. A subset $A \subset \mathbb{U}$ of the Banach space $\mathbb{U}$ is said to be *(sequentially) compact* iff any sequence $a_i \in A$ has a convergent subsequence which converges to a point $a \in A$.

Theorem B.10. *Any compact subset* $A \subset \mathbb{U}$ *of the Banach space* $\mathbb{U}$ *is bounded.*

Proof. *Ab absurdo*, if A is not bounded, then there exists a divergent sequence in A. ♦

Definition B.11. A subset $A \subset \mathbb{U}$ of the Banach space $\mathbb{U}$ is said to be *precompact* iff its closure in $\mathbb{U}$ is compact.

Remark B.12. Despite, by virtue of the Heine–Borel theorem, in finite-dimensional spaces the definition of boundedness and precompactness are equivalent, this is not true in infinite-dimensional spaces.

Definition B.13. A linear operator $T : \mathbb{U} \to \mathbb{V}$ between the Banach spaces $\mathbb{U}$ and $\mathbb{V}$ is said to be *compact* iff for any bounded subset $A \subset \mathbb{U}$ its image $T(A) \subset \mathbb{V}$ is precompact.

Theorem B.14. *If $T : \mathbb{U} \to \mathbb{V}$ is a linear and compact operator and $S : \mathbb{V} \to \mathbb{W}$ and $R : \mathbb{W} \to \mathbb{U}$ are linear and bounded operators between the Banach spaces $\mathbb{U}$, $\mathbb{V}$ and $\mathbb{W}$, then the compositions TR and ST are compact operators.*

Proof. If $A \subset \mathbb{W}$ is bounded, then $R(A) \subset \mathbb{U}$ is bounded, and so $T(R(A)) \subset \mathbb{V}$ is precompact. Vice versa, if $A \subset \mathbb{U}$ is bounded, then $T(A) \subset \mathbb{V}$ is precompact, and so, because of the continuity of S, $S(T(A)) \subset \mathbb{W}$ is precompact. ♦

Corollary B.15. *In infinite-dimensional spaces, the inverse of a compact operator is not continuous.*

Proof. Ab absurdo, being T a compact operator, if T^{-1} is continuous, then the identity operator $I = TT^{-1}$ is compact, which is false because of remark B.12. ♦

Remark B.16. Because of the latter corollary, when the solution to a direct problem is obtained by a compact operator, then the corresponding inverse problem is ill-posed in the sense of Hadamard. Based on that, the following example shows that derivation is an ill-posed inverse problem.

Lemma B.17. *The linear operator $A : L^2(0,1) \to L^2(0,1)$ such that*

$$(Au)(x) = \int_0^1 K(x,y)u(y)\,\mathrm{d}y\,,$$

with kernel $K(x,y)$ square summable, is a compact operator. Such an operator is called Hilbert–Schmidt integral operator.

Example B.18. Let us consider the operator A defined like in lemma B.17 with kernel

$$K(x,y) = \begin{cases} 1, & \text{if } x \geq y \\ 0, & \text{elsewhere} \end{cases}$$

Clearly, the kernel is square summable ($\|K\|_{L^2}^2 = 1/2 < +\infty$), so A is compact. The considered Hilbert–Schmidt integral operator reads

$$(Au)(x) = \int_0^x u(y)\,\mathrm{d}y\,,$$

which is the well-known inverse of the derivative operator as it appears in the fundamental theorem of calculus. As a consequence, the derivative operator,

$$\left(A^{-1}u\right)(x) = u'(x)\,,$$

is not continuous. The same conclusion can be achieved in a more straightforward way by using a counterexample to the continuity of A^{-1}. Let us consider the convergent sequence of functions

$$u_n(x) = x + n^{-1/2}\sin(nx) \to u(x) = x\,, \quad \text{in } L^2(0,1)\,.$$

Ab absurdo, if A^{-1} is continuous, then $A^{-1}u_n \to u$, but

$$\left(A^{-1}u_n\right)(x) = u_n'(x) = 1 + n^{1/2}\cos(nx)$$

is a divergent sequence.

B.2 Derivatives of a phase

The gradient of a phase $\varphi : \mathbb{R}^d \to [0, 2\pi)$ can be computed by noting that

$$\nabla \mathrm{e}^{\mathrm{i}\varphi} = \mathrm{e}^{\mathrm{i}\varphi}\mathrm{i}\nabla\varphi \quad \Rightarrow \quad \nabla\varphi = -\mathrm{i}\frac{\nabla \mathrm{e}^{\mathrm{i}\varphi}}{\mathrm{e}^{\mathrm{i}\varphi}}\,. \tag{B.1}$$

By this way, the discontinuities induced by the wrap mechanism of the real map in the interval $[0, 2\pi)$ are ignored and, actually, the derivative of the so-called unwrapped phase is computed. The Laplacian of φ can be computed similarly,

$$\nabla^2\varphi = -\mathrm{i}\left(\frac{\nabla^2 \mathrm{e}^{\mathrm{i}\varphi}}{\mathrm{e}^{\mathrm{i}\varphi}} + \nabla\left(\frac{1}{\mathrm{e}^{\mathrm{i}\varphi}}\right)\cdot\nabla \mathrm{e}^{\mathrm{i}\varphi}\right) = -\mathrm{i}\left(\frac{\nabla^2 \mathrm{e}^{\mathrm{i}\varphi}}{\mathrm{e}^{\mathrm{i}\varphi}} - \frac{|\nabla \mathrm{e}^{\mathrm{i}\varphi}|^2}{\mathrm{e}^{\mathrm{i}2\varphi}}\right)\,. \tag{B.2}$$

References

[1] European Society of Radiology (ESR). ESR statement on the stepwise development of imaging biomarkers. *Insights into Imaging*, 4(2):147–152, 2013.

[2] D.C. Sullivan, N.A. Obuchowski, L.G. Kessler, D.L. Raunig, C. Gatsonis, E.P. Huang, M. Kondratovich, L.M. McShane, A.P. Reeves, D.P. Barboriak, A.R. Guimaraes, and R.L. Wahl. Metrology standards for quantitative imaging biomarkers. *Radiology*, 277(3):813–825, 2015.

[3] S.K. Venkatesh, M. Yin, and R.L. Ehman. Magnetic resonance elastography of liver: Technique, analysis, and clinical applications. *Journal of Magnetic Resonance Imaging*, 37(3):544–555, 2013.

[4] L.V. Hiscox, C.L. Johnson, E. Barnhill, M.D.J. McGarry, J. Huston, E.J.R. Van Beek, J.M. Starr, and N. Roberts. Magnetic resonance elastography (MRE) of the human brain: Technique, findings and clinical applications. *Physics in Medicine and Biology*, 61(24):R401–R437, 2016.

[5] European Society of Radiology (ESR). Magnetic resonance fingerprinting - a promising new approach to obtain standardized imaging biomarkers from MRI. *Insights into Imaging*, 6(2):163–165, 2015.

[6] D. Ma, V. Gulani, N. Seiberlich, K. Liu, J.L. Sunshine, J.L. Duerk, and M.A. Griswold. Magnetic resonance fingerprinting. *Nature*, 495(7440):187–192, 2013.

[7] L. Sha, E.R. Ward, and B. Stroy. A review of dielectric properties of normal and malignant breast tissue. *Conference Proceedings - IEEE SOUTHEASTCON*, pages 457–462, 2002.

[8] M. Lazebnik, D. Popovic, L. McCartney, C.B. Watkins, M.J. Lindstrom, J. Harter, S. Sewall, T. Ogilvie, A. Magliocco, T.M. Breslin, W. Temple, D. Mew, J.H. Booske, M. Okoniewski, and S.C. Hagness. A large-scale study of the ultrawideband microwave dielectric properties of normal, benign and malignant breast tissues obtained from cancer surgeries. *Physics in Medicine and Biology*, 52(20):6093–6115, 2007.

[9] J. Shin, M.J. Kim, J. Lee, Y. Nam, M.-O. Kim, N. Choi, S. Kim, and D.-H. Kim. Initial study on in vivo conductivity mapping of breast cancer using MRI. *Journal of Magnetic Resonance Imaging*, 42(2):371–378, 2015.

[10] S.-Y. Kim, J. Shin, D.-H. Kim, M.J. Kim, E.-K. Kim, H.J. Moon, and J.H. Yoon. Correlation between conductivity and prognostic factors in invasive breast cancer using magnetic resonance electric properties tomography (MREPT). *European Radiology*, 26(7):2317–2326, 2016.

[11] Z. Li, G. Deng, Z. Li, S.X. Xin, S. Duan, M. Lan, S. Zhang, Y. Gao, J. He, S. Zhang, H. Tang, W. Wang, S. Han, Q.X. Yang, L. Zhuang, J. Hu, and F. Liu. A large-scale measurement of dielectric properties of normal and malignant colorectal tissues obtained from cancer surgeries at Larmor frequencies. *Medical Physics*, 43(11):5991–5997, 2016.

[12] N.R. Datta, S.G. Ordóñez, U.S. Gaipl, M.M. Paulides, H. Crezee, J. Gellermann, D. Marder, E. Puric, and S. Bodis. Local hyperthermia combined with radiotherapy and-/or chemotherapy: Recent advances and promises for the future. *Cancer Treatment Reviews*, 41(9):742–753, 2015.

[13] W.B. Coley. The treatment of malignant tumors by repeated inoculations of erysipelas: with a report of ten original cases. *The American Journal of the Medical Sciences*, 105:487–511, 1893.

[14] J. van der Zee, Z. Vujaskovic, M. Kondo, and T. Sugahara. The Kadota Fund International Forum 2004 - clinical group consensus. *International Journal of Hyperthermia*, 24(2):111–122, 2008.

[15] J. Overgaard. The heat is (still) on - the past and future of hyperthermic radiation oncology. *Radiotherapy and Oncology*, 109(2):185–187, 2013.

[16] T. Kobayashi. Cancer hyperthermia using magnetic nanoparticles. *Biotechnology Journal*, 6(11):1342–1347, 2011.

[17] W.J. Stark. Nanoparticles in biological systems. *Angewandte Chemie - International Edition*, 50(6):1242–1258, 2011.

[18] T. Kotnik, W. Frey, M. Sack, S. Haberl Meglič, M. Peterka, and D. Miklavčič. Electroporation-based applications in biotechnology. *Trends in Biotechnology*, 33(8):480–488, 2015.

[19] M.L. Yarmush, A. Golberg, G. Serša, T. Kotnik, and D. Miklavčič. Electroporation-based technologies for medicine: Principles, applications, and challenges. *Annual Review of Biomedical Engineering*, 16:295–320, 2014.

[20] S. Corovic, I. Lackovic, P. Sustaric, T. Sustar, T. Rodic, and D. Miklavcic. Modeling of electric field distribution in tissues during electroporation. *BioMedical Engineering Online*, 12(1), 2013. Art. no. 16.

[21] K. Varani, F. Vincenzi, A. Ravani, S. Pasquini, S. Merighi, S. Gessi, S. Setti, M. Cadossi, P.A. Borea, and R. Cadossi. Adenosine receptors as a biological pathway for the anti-inflammatory and beneficial effects of low frequency low energy pulsed electromagnetic fields. *Mediators of Inflammation*, 2017, 2017. Art. no. 2740963.

[22] F. Vincenzi, M. Targa, C. Corciulo, S. Gessi, S. Merighi, S. Setti, R. Cadossi, M.B. Goldring, P.A. Borea, and K. Varani. Pulsed electromagnetic fields increased the anti-inflammatory effect of A2A and A3 adenosine receptors in human T/C-28a2 chondrocytes and hFOB 1.19 osteoblasts. *PLoS ONE*, 8(5), 2013. Art. no. e65561.

[23] F. Vincenzi, M. Targa, C. Corciulo, S. Gessi, S. Merighi, S. Setti, R. Cadossi, P.A. Borea, and K. Varani. The anti-tumor effect of A3 adenosine receptors is potentiated by pulsed electromagnetic fields in cultured neural cancer cells. *PLoS ONE*, 7(6), 2012. Art. no. e39317.

[24] A. Paffi, F. Camera, E. Lucano, F. Apollonio, and M. Liberti. Time resolved dosimetry of human brain exposed to low frequency pulsed magnetic fields. *Physics in Medicine and Biology*, 61(12):4452–4465, 2016.

[25] A.T. Barker, R. Jalinous, and I.L. Freeston. Non-invasive magnetic stimulation of human motor cortex. *The Lancet*, 325(8437):1106–1107, 1985.

[26] J.-P. Lefaucheur, N. André-Obadia, A. Antal, S.S. Ayache, C. Baeken, D.H. Benninger, R.M. Cantello, M. Cincotta, M. de Carvalho, D. De Ridder, H. Devanne, V. Di Lazzaro, S.R. Filipović, F.C. Hummel, S.K. Jääskeläinen, V.K. Kimiskidis, G. Koch, B. Langguth, T. Nyffeler, A. Oliviero, F. Padberg, E. Poulet, S. Rossi, P.M. Rossini, J.C. Rothwell, C. Schönfeldt-Lecuona, H.R. Siebner, C.W. Slotema, C.J. Stagg, J. Valls-Sole, U. Ziemann, W. Paulus, and L. Garcia-Larrea. Evidence-based guidelines on the therapeutic use of repetitive transcranial magnetic stimulation (rTMS). *Clinical Neurophysiology*, 125(11):2150–2206, 2014.

[27] O. Bottauscio, M. Chiampi, L. Zilberti, and M. Zucca. Evaluation of electromagnetic phenomena induced by transcranial magnetic stimulation. *IEEE Transactions on Magnetics*, 50(2), 2014. Art. no. 6749157.

[28] C. Gabriel, S. Gabriel, and E. Corthout. The dielectric properties of biological tissues: I. Literature survey. *Physics in Medicine and Biology*, 41(11):2231–2249, 1996.

[29] S. Gabriel, R.W. Lau, and C. Gabriel. The dielectric properties of biological tissues: II. Measurements in the frequency range 10 hz to 20 ghz. *Physics in Medicine and Biology*, 41(11):2251–2269, 1996.

[30] S. Gabriel, R.W. Lau, and C. Gabriel. The dielectric properties of biological tissues: III. Parametric models for the dielectric spectrum of tissues. *Physics in Medicine and Biology*, 41(11):2271–2293, 1996.

[31] L. Borcea. Electrical impedance tomography. *Inverse Problems*, 18(6):R99–R136, 2002.

[32] A. Bossavit. *Computational electromagnetism*, volume 2 of *Electromagnetism*. Academic Press, San Diego (US-CA), 1998.

[33] G. Uhlmann. Electrical impedance tomography and Calderón's problem. *Inverse Problems*, 25(12), 2009. Art. no. 123011.

[34] Y. Song, E. Lee, E.J. Woo, and J.K. Seo. Optimal geometry toward uniform current density electrodes. *Inverse Problems*, 27(7), 2011. Art. no. 075004.

[35] J.K. Seo, E.J. Woo, U. Katscher, and Y. Wang. *Electro-magnetic tissue properties MRI*, volume 1 of *Modelling and simulation in medical imaging*. Imperial College Press, London (GB), 2014.

[36] A.P. Calderón. On an inverse boundary value problem. *Computational & Applied Mathematics*, 25:133–138, 2006.

[37] E.J. Woo and J.K. Seo. Magnetic resonance electrical impedance tomography (MREIT) for high-resolution conductivity imaging. *Physiological Measurement*, 29(10):R1–R26, 2008.

[38] M. Joy, G. Scott, and M. Henkelman. In vivo detection of applied electric currents by magnetic resonance imaging. *Magnetic Resonance Imaging*, 7(1):89–94, 1989.

[39] J.K. Seo, J.-R. Yoon, E.J. Woo, and O. Kwon. Reconstruction of conductivity and current density images using only one component of magnetic field measurements. *IEEE Transactions on Biomedical Engineering*, 50(9):1121–1124, 2003.

[40] C. Liu, W. Li, and I. Argyridis. Imaging electric conductivity and conductivity anisotropy via eddy currents induced by pulsed field gradients. In *Proceedings of the 22nd Annual Meeting of ISMRM*, page 0638, Milan (IT), 2014.

[41] E. Gibbs and C. Liu. Feasibility of imaging tissue electrical conductivity by switching field gradients with MRI. *Tomography*, 1(2):125–135, 2015.

[42] O.F. Oran and Y.Z. Ider. Feasibility of conductivity imaging using subject eddy currents induced by switching of MRI gradients. *Magnetic Resonance in Medicine*. In press. doi:10.1002/MRM.26283.

[43] D. Colton and R. Kress. *Inverse acoustic and electromagnetic scattering theory*, volume 93 of *Applied mathematical sciences*. Springer-Verlang, New York (US-NY), third edition, 2013.

[44] S. Caorsi, G.L. Gragnani, and M. Pastorino. Two-dimensional microwave imaging by a numerical inverse scattering solution. *IEEE Transactions on Microwave Theory and Techniques*, 38(8):981–989, 1990.

[45] T. Habashy and M. Oristaglio. Simultaneous nonlinear reconstruction of two-dimensional permittivity and conductivity. *Radio Science*, 29(4):1101–1118, 1994.

[46] T. Isernia, V. Pascazio, and R. Pierri. A nonlinear estimation method in tomographic imaging. *IEEE Transactions on Geoscience and Remote Sensing*, 35(4):910–923, 1997.

[47] P.M. Van Den Berg and R.E. Kleinman. A contrast source inversion method. *Inverse Problems*, 13(6):1607–1620, 1997.

[48] A. Abubakar, P.M. Van Den Berg, and J.J. Mallorqui. Imaging of biomedical data using a multiplicative regularized contrast source inversion method. *IEEE Transactions on Microwave Theory and Techniques*, 50(7):1761–1771, 2002.

[49] A. Zakaria, I. Jeffrey, and J. LoVetri. Full-vectorial parallel finite-element contrast source inversion method. *Progress in Electromagnetics Research*, 142:463–483, 2013.

[50] E.A. Attardo, G. Vecchi, and L. Crocco. Contrast source extended born inversion in noncanonical scenarios via FEM modeling. *IEEE Transactions on Antennas and Propagation*, 62(9):4674–4685, 2014.

[51] O.M. Bucci and T. Isernia. Electromagnetic inverse scattering: Retrievable information and measurement strategies. *Radio Science*, 32(6):2123–2137, 1997.

[52] T. Isernia, V. Pascazio, and R. Pierri. On the local minima in a tomographic imaging technique. *IEEE Transactions on Geoscience and Remote Sensing*, 39(7):1596–1607, 2001.

[53] R. Stollberger and P. Wach. Imaging of the active B1 field in vivo. *Magnetic Resonance in Medicine*, 35(2):245–251, 1996.

[54] C.H. Cunningham, J.M. Pauly, and K.S. Nayak. Saturated double-angle method for rapid B1+ mapping. *Magnetic Resonance in Medicine*, 55(6):1326–1333, 2006.

[55] V.L. Yarnykh. Actual flip-angle imaging in the pulsed steady state: A method for rapid three-dimensional mapping of the transmitted radiofrequency field. *Magnetic Resonance in Medicine*, 57(1):192–200, 2007.

[56] L.I. Sacolick, F. Wiesinger, I. Hancu, and M.W. Vogel. B1 mapping by Bloch-Siegert shift. *Magnetic Resonance in Medicine*, 63(5):1315–1322, 2010.

[57] D.J. Park, N.K. Bangerter, A. Javed, J. Kaggie, M.M. Khalighi, and G.R. Morrell. A statistical analysis of the Bloch-Siegert B1 mapping technique. *Physics in Medicine and Biology*, 58(16):5673–5691, 2013.

[58] U. Katscher, C. Findeklee, P. Vernickel, K. Nehrke, T. Voigt, and O. Dössel. Determination of electric conductivity and local SAR via B1 mapping. *IEEE Transactions on Medical Imaging*, 28(9):1365–1374, 2009.

[59] X. Zhang, S. Zhu, and B. He. Imaging electric properties of biological tissues by RF field mapping in MRI. *IEEE Transactions on Medical Imaging*, 29(2):474–481, 2010. Art. no. 5405651.

[60] A.L.H.M.W. Van Lier, D.O. Brunner, K.P. Pruessmann, D.W.J. Klomp, P.R. Luijten, J.J.W. Lagendijk, and C.A.T. Van Den Berg. B1+ phase mapping at 7 T and its application for in vivo electrical conductivity mapping. *Magnetic Resonance in Medicine*, 67(2):552–561, 2012.

[61] X. Zhang, P.-F. Van de Moortele, S. Schmitter, and B. He. Complex B1 mapping and electrical properties imaging of the human brain using a 16-channel transceiver coil at 7 T. *Magnetic Resonance in Medicine*, 69(5):1285–1296, 2013.

[62] E.M. Haacke, L.S. Petropoulos, E.W. Nilges, and D.H. Wu. Extraction of conductivity and permittivity using magnetic resonance imaging. *Physics in Medicine and Biology*, 36(6):723–734, 1991. Art. no. 002.

[63] H. Wen. Non-invasive quantitative mapping of conductivity and dielectric distributions using the RF wave propagation effects in high field MRI. *Proceedings of SPIE - The International Society for Optical Engineering*, 5030 I:471–477, 2003.

[64] U. Katscher, D.-H. Kim, and J.K. Seo. Recent progress and future challenges in MR electric properties tomography. *Computational and Mathematical Methods in Medicine*, 2013. Art. no. 546562.

[65] G. Duensing, C. Saylor, and F. Huang. Method and apparatus for noise tomography, August 28 2003. US Patent App. 10/323,135.

[66] F. Huang, S. Reza, C. Saylor, S. Vijayakumara, G.R. Duensing, and M.K. Limkeman. Outline of the reconstruction method for MR-NT. In *Proceedings of the 13th Annual Meeting ISMRM*, page 683, Miami (US-FL), 2005.

[67] S. Reza, F. Huang, G. Bosman, G.R. Duensing, M.K. Limkeman, and C. Saylor. MR-noise tomography: extracting information from noise. In *Proceedings of the 13th Annual Meeting ISMRM*, page 955, Miami (US-FL), 2005.

[68] U. Katscher, M. Hanft, P. Vernickel, and C. Findeklee. Experimental verification of electric properties tomography (EPT). In *Proceedings of the 14th Annual Meeting ISMRM*, page 3035, Seattle (US-WA), 2006.

[69] U. Katscher, M. Hanft, P. Vernickel, and C. Findeklee. Electric properties tomography (EPT) via MRI. In *Proceedings of the 14th Annual Meeting ISMRM*, page 3037, Seattle (US-WA), 2006.

[70] T. Voigt, U. Katscher, and O. Doessel. Quantitative conductivity and permittivity imaging of the human brain using electric properties tomography. *Magnetic Resonance in Medicine*, 66(2):456–466, 2011.

[71] D.K. Sodickson, L. Alon, C.M. Deniz, R. Brown, B. Zhang, G.C. Wiggins, G.Y. Cho, N.B. Eliezer, D.S. Novikov, R. Lattanzi, Q. Duan, L.A. Sodickson, and Y. Zhu. Local Maxwell tomography using transmit-receive coil arrays for contact-free mapping of tissue electric properties and determination of absolute RF phase. In *Proceedings of the 20th Annual Meeting ISMRM*, page 387, Melbourne (AU-VIC), 2012.

[72] F.S. Hafalir, O.F. Oran, N. Gurler, and Y.Z. Ider. Convection-reaction equation based magnetic resonance electrical properties tomography (cr-MREPT). *IEEE Transactions on Medical Imaging*, 33(3):777–793, 2014. Art. no. 6697855.

[73] H. Ammari, H. Kwon, Y. Lee, K. Kang, and J.K. Seo. Magnetic resonance-based reconstruction method of conductivity and permittivity distributions at the Larmor frequency. *Inverse Problems*, 31(10), 2015. Art. no. 105001.

[74] E. Balidemaj, C.A.T. Van Den Berg, J. Trinks, A.L.H.M.W. Van Lier, A.J. Nederveen, L.J.A. Stalpers, H. Crezee, and R.F. Remis. CSI-EPT: A contrast source inversion approach for improved MRI-based electric properties tomography. *IEEE Transactions on Medical Imaging*, 34(9):1788–1796, 2015. Art. no. 7046353.

[75] S.-K. Lee, S. Bulumulla, F. Wiesinger, L. Sacolick, W. Sun, and I. Hancu. Tissue electrical property mapping from zero echo-time magnetic resonance imaging. *IEEE Transactions on Medical Imaging*, 34(2):541–550, 2015. Art. no. 6918510.

[76] A. Borsic, I. Perreard, A. Mahara, and R.J. Halter. An inverse problems approach to MR-EPT image reconstruction. *IEEE Transactions on Medical Imaging*, 35(1):244–256, 2016. Art. no. 7214288.

[77] V. Palamodov. An analytic method for the inverse problem of MREPT. *Inverse Problems*, 32(3), 2016. Art. no. 035003.

[78] R. Schmidt and A. Webb. A new approach for electrical properties estimation using a global integral equation and improvements using high permittivity materials. *Journal of Magnetic Resonance*, 262:8–14, 2016.

[79] J.K. Seo, M.-O. Kim, J. Lee, N. Choi, E.J. Woo, H.J. Kim, O.I. Kwon, and D.-H. Kim. Error analysis of nonconstant admittivity for MR-based electric property imaging. *IEEE Transactions on Medical Imaging*, 31(2):430–437, 2012. Art. no. 6036177.

[80] S.-K. Lee, S. Bulumulla, and I. Hancu. Theoretical investigation of random noise-limited signal-to-noise ratio in MR-based electrical properties tomography. *IEEE Transactions on Medical Imaging*, 34(11):2220–2232, 2015. Art. no. 7100918.

[81] C.M. Collins, B. Yang, Q.X. Yang, and M.B. Smith. Numerical calculations of the static magnetic field in three-dimensional multi-tissue models of the human head. *Magnetic Resonance Imaging*, 20(5):413–424, 2002.

[82] A. Nachman, D. Wang, W. Ma, and M. Joy. A local formula for inhomogeneous complex conductivity as a function of the RF magnetic field. In *Proceedings of the Joint Annual Meeting ISMRM-ESMRMB*, Berlin (DE), 2007. [Online]. Available: http://cds.ismrm.org/protected/Unsolved_Problems/U05/.

[83] A.L.H.M.W. Van Lier, A. Raaijmakers, T. Voigt, J.J.W. Lagendijk, P.R. Luijten, U. Katscher, and C.A.T. Van Den Berg. Electrical properties tomography in the human brain at 1.5, 3, and 7T: A comparison study. *Magnetic Resonance in Medicine*, 71(1):354–363, 2014.

[84] J. Lee, J. Shin, and D.-H. Kim. Mr-based conductivity imaging using multiple receiver coils. *Magnetic Resonance in Medicine*, 76(2):530–539, 2016.

[85] U. Katscher, K. Djamshidi, T. Voigt, M. Ivancevic, H. Abe, G. Newstead, and J. Keupp. Estimation of breast tumor conductivity using parabolic phase fitting. In *Proceedings of the 20th Annual Meeting ISMRM*, page 2335, Melbourne (AU-VIC), 2012.

[86] E. Balidemaj, A.L.H.M.W. Van Lier, H. Crezee, A.J. Nederveen, L.J.A. Stalpers, and C.A.T. Van Den Berg. Feasibility of electric property tomography of pelvic tumors at 3t. *Magnetic Resonance in Medicine*, 73(4):1505–1513, 2015.

[87] J. Hamilton, D. Franson, and N. Seiberlich. Recent advances in parallel imaging for MRI. *Progress in Nuclear Magnetic Resonance Spectroscopy*, 101:71–95, 2017.

[88] J.P. Marques, D.K. Sodickson, O. Ipek, C.M. Collins, and R. Gruetter. Single acquisition electrical property mapping based on relative coil sensitivities: A proof-of-concept demonstration. *Magnetic Resonance in Medicine*, 74(1):185–195, 2015.

[89] D.-H. Kim, N. Choi, S.-M. Gho, J. Shin, and C. Liu. Simultaneous imaging of in vivo conductivity and susceptibility. *Magnetic Resonance in Medicine*, 71(3):1144–1150, 2014.

[90] E. Michel, D. Hernandez, M.H. Cho, and S.Y. Lee. Denoising of B_1^+ field maps for noise-robust image reconstruction in electrical properties tomography. *Medical Physics*, 41(10), 2014. Art. no. 102304.

[91] A. Savitzky and M.J.E. Golay. Smoothing and differentiation of data by simplified least squares procedures. *Analytical Chemistry*, 36(8):1627–1639, 1964.

[92] J. Steinier, Y. Termonia, and J. Deltour. Comments on smoothing and differentiation of data by simplified least square procedure. *Analytical Chemistry*, 44(11):1906–1909, 1972.

[93] L. Huang, F. Schweser, K.-H. Herrmann, M. Kr amer, A. Deistung, and J.R. Reichenbach. A Monte Carlo method for overcoming the edge artifacts in MRI-based electrical conductivity mapping. In *Proceedings of the 22nd Annual Meeting ISMRM*, page 3190, Milan (IT), 2014.

[94] T.H. Cormen, C.E. Leiserson, R.L. Rivest, and C. Stein. *Introduction to Algorithms*. The MIT Press, second edition, 2001.

[95] X. Zhang, J. Liu, and B. He. Magnetic-resonance-based electrical properties tomography: A review. *IEEE Reviews in Biomedical Engineering*, 7:87–96, 2014.

[96] J.T. Vaughan, G. Adriany, C.J. Snyder, J. Tian, T. Thiel, L. Bolinger, H. Liu, L. DelaBarre, and K. Ugurbil. Efficient high-frequency body coil for high-field mri. *Magnetic Resonance in Medicine*, 52(4):851–859, 2004.

[97] J.T. Vaughan and J.R. Griffiths, editors. *RF coils for MRI*. Encyclopedia of Magnetic Resonance Hanbooks. John Wiley & Sons, Chichester (GB), 2012.

[98] X. Zhang, S. Schmitter, P.-F. Van De Moortele, J. Liu, and B. He. From complex B1 mapping to local SAR estimation for human brain MR imaging using multi-channel transceiver coil at 7 T. *IEEE Transactions on Medical Imaging*, 32(6):1058–1067, 2013. Art. no. 6477144.

[99] J. Liu, X. Zhang, S. Schmitter, P.-F. Van De Moortele, and B. He. Gradient-based electrical properties tomography (gEPT): A robust method for mapping electrical properties of biological tissues in vivo using magnetic resonance imaging. *Magnetic Resonance in Medicine*, 74(3):634–646, 2015.

[100] A. Hoyos-Idrobo, P. Weiss, A. Massire, A. Amadon, and N. Boulant. On variant strategies to solve the magnitude least squares optimization problem in parallel transmission pulse design and under strict SAR and power constraints. *IEEE Transactions on Medical Imaging*, 33(3):739–748, 2014.

[101] U. Katscher, C. Findeklee, and T. Voigt. B1-based specific energy absorption rate determination for nonquadrature radiofrequency excitation. *Magnetic Resonance in Medicine*, 68(6):1911–1918, 2012.

[102] J. Liu, X. Zhang, P.-F. Van De Moortele, S. Schmitter, and B. He. Determining electrical properties based on B1 fields measured in an MR scanner using a multi-channel transmit/receive coil: A general approach. *Physics in Medicine and Biology*, 58(13):4395–4408, 2013.

[103] J. Liu, P.-F. Van De Moortele, X. Zhang, Y. Wang, and B. He. Simultaneous quantitative imaging of electrical properties and proton density from B1 maps using MRI. *IEEE Transactions on Medical Imaging*, 35(9):2064–2073, 2016. Art. no. 7442843.

[104] J. Liu, X. Zhang, P.-F. Van de Moortele, S. Schmitter, and B. He. Simultaneous determination of electrical properties and proton density in a generalized gradient-based electrical properties tomography. In *Proceedings of the 22nd Annual Meeting of ISMRM*, page 3194, Milan (IT), 2014.

[105] D.K. Sodickson, L. Alon, C.M. Deniz, N.B. Eliezer, M. Cloos, L.A. Sodickson, C.M. Collins, G.C. Wiggins, and D.S. Novikov. Generalized local Maxwell tomography for mapping of electrical property gradients and tensors. In *Proceedings of the 21st Annual Meeting ISMRM*, page 4175, Salt Lake City (US-UT), 2013.

[106] J. Liu, X. Zhang, Y. Wang, P.-F. Van de Moortele, and B. He. Local electric properties tomography with global regularization by gradient. In *Proceedings of the 23rd Annual Meeting ISMRM*, page 3297, Toronto (CA-ON), 2015.

[107] J. Liu, Q. Shao, Y. Wang, G. Adriany, J. Bischof, P.-F. Van de Moortele, and B. He. In vivo imaging of electrical properties of an animal tumor model with an 8-channel transceiver array at 7T using electrical properties tomography. *Magnetic Resonance in Medicine*. In press. doi:10.1002/MRM.26609.

[108] J. Shin, M.-O. Kim, S. Cho, and D.-H. Kim. Fast spin echo imaging based EPT with k-space weighting via T_2 relaxation (rEPT). *IEEE Transactions on medical imaging*. In press. doi:10.1109/TMI.2017.2684194.

[109] P.E.Z. Larson, M. Han, R. Krug, A. Jakary, S.J. Nelson, D.B. Vigneron, R.G. Henry, G. McKinnon, and D.A.C. Kelley. Ultrashort echo time and zero echo time MRI at 7T. *Magnetic Resonance Materials in Physics, Biology and Medicine*, 29(3):359–370, 2016.

[110] N. Gurler and Y.Z. Ider. Gradient-based electrical conductivity imaging using MR phase. *Magnetic Resonance in Medicine*, 77(1):137–150, 2017.

[111] N. Gurler, O.F. Oran, and Y.Z. Ider. CR-MREPT using multichannel receive coil. In *Proceedings of the 22nd Annual Meeting ISMRM*, page 3247, Milan (IT), 2014.

[112] IT'IS Foundation. Database for thermal and electromagnetic parameters of biological tissues, 2017. [Online]. Available: http://www.itis.ethz.ch/database.

[113] A. Quarteroni. *Modellistica numerica per problemi differenziali*, volume 63 of *UNITEXT - La matematica per il 3+2*. Springer-Verlang Italia, Milan (IT), fifth edition, 2012.

[114] R.J. LeVeque. *Finite-volume methods for hyperbolic problems*. Cambridge texts in applied mathematics. Cambridge university press, Cambridge (GB), 2004.

[115] Y. Song and J.K. Seo. Conductivity and permittivity image reconstruction at the Larmor frequency using MRI. *SIAM Journal on Applied Mathematics*, 73(6):2262–2280, 2013.

[116] K.M. Ropella and D.C. Noll. A regularized, model-based approach to phase-based conductivity mapping using MRI. *Magnetic Resonance in Medicine*, 2016.

[117] E. Balidemaj, J. Trinks, C.A.T. Van Den Berg, A.J. Nederveen, A.L. Van Lier, L.J.A. Stalpers, J. Crezee, and R.F. Remis. CSI-EPT: A novel contrast source approach to MRI based electric properties tomography and patient-specific SAR. In *Proceedings of the 2013 International Conference on Electromagnetics in Advanced Applications, ICEAA 2013*, pages 668–671, Turin (IT), 2013. Art. no. 6632328.

[118] **A. Arduino**, M. Chiampi, L. Zilberti, and O. Bottauscio. Alternative approaches to magnetic resonance-based electric properties tomography and local specific absorption rate estimation. *IEEE Transactions on Magnetics*, 53(2), 2017. Art. no. 7707370.

[119] R.S. Elliott. *Electromagnetics: History, Theory, and Applications*. Electromagnetic Wave Theory. Wiley-IEEE Press, New York (US-NY), 1993.

[120] P.M. van den Berg and A. Abubakar. Contrast source inversion method: State of art. *Progress in Electromagnetics Research*, 34:189–218, 2001.

[121] **A. Arduino**, M. Chiampi, F. Pennecchi, L. Zilberti, and O. Bottauscio. Monte Carlo method for uncertainty propagation in magnetic resonance-based electric properties tomography. *IEEE Transactions on Magnetics*. In press. doi:10.1109/TMAG.2017.2713984.

[122] **A. Arduino**, L. Zilberti, M. Chiampi, and O. Bottauscio. CSI-EPT in presence of RF-shield for MR-coils. *IEEE Transactions on medical imaging*, 36(7), 2017.

[123] P. Farace, R. Pontalti, L. Cristoforetti, R. Antolini, and M. Scarpa. An automated method for mapping human tissue permittivities by MRI in hyperthermia treatment planning. *Physics in Medicine and Biology*, 42(11):2159–2174, 1997.

[124] E. Michel, D. Hernandez, and S.Y. Lee. Electrical conductivity and permittivity maps of brain tissues derived from water content based on T1-weighted acquisition. *Magnetic Resonance in Medicine*, 77(3):1094–1103, 2017.

[125] T. Nara, T. Furuichi, and M. Fushimi. An explicit reconstruction method for magnetic resonance electrical property tomography based on the generalized Cauchy formula. *Inverse problems*. In press. doi:10.1088/1361-6420/AA8414.

[126] J.E.C. Serrallés, L. Daniel, J.K. White, D.K. Sodickson, R. Lattanzi, and A.G. Polimeridis. Global Maxwell tomography: A novel technique for electrical properties mapping based on MR measurements and volume integral equation formulations. *2016 IEEE Antennas and Propagation Society International*

Symposium, APSURSI 2016 - Proceedings, pages 1395–1396, 2016. Art. no. 7696404.

[127] A. Borsic, I. Perreard, and R.J. Halter. An inverse approach to MR-EPT reconstruction. In *Proceedings of the 22nd Annual Meeting ISMRM*, page 3191, Milan (IT), 2014.

[128] H.P. Schwan. Electrical properties of tissue and cell suspensions. *Advances in biological and medical physics*, 5:147–209, 1957.

[129] B.G. Konopelchenko. On dbar-problem and integrable equations, 2000. [Online]. Available: https://arxiv.org/abs/nlin/0002049v1.

[130] G. Pelekanos, A. Abubakar, and P.M. Van den Berg. Contrast source inversion methods in elastodynamics. *Journal of the Acoustical Society of America*, 114(5):2825–2834, 2003.

[131] A. Abubakar, G. Pan, M. Li, L. Zhang, T.M. Habashy, and P.M. Van Den Berg. Three-dimensional seismic full-waveform inversion using the finite-difference contrast source inversion method. *Geophysical Prospecting*, 59(5):874–888, 2011.

[132] A. Abubakar, W. Hu, P.M. Van Den Berg, and T.M. Habashy. A finite-difference contrast source inversion method. *Inverse Problems*, 24(6), 2008. Art. no. 065004.

[133] M. Pastorino, A. Randazzo, A. Fedeli, A. Salvadè, S. Poretti, M. Maffongelli, R. Monleone, and M. Lanini. A microwave tomographic system for wood characterization in the forest products industry. *Wood Material Science and Engineering*, 10(1):75–85, 2015.

[134] E. Balidemaj, C.A.T. van den Berg, A.L.H.M.W. van Lier, A.J. Nederveen, L.J.A. Stalpers, H. Crezee, and R.F. Remis. B1-based SAR reconstruction using contrast source inversion–electric properties tomography (CSI-EPT). *Medical and Biological Engineering and Computing*, 55(2):225–233, 2017.

[135] F. Seifert, G. Wübbeler, S. Junge, B. Ittermann, and H. Rinneberg. Patient safety concept for multichannel transmit coils. *Journal of Magnetic Resonance Imaging*, 26(5):1315–1321, 2007.

[136] H.H. Pennes. Analysis of tissue and arterial blood temperatures in the resting human forearm. *Journal of applied physiology*, 1(2):93–122, 1948.

[137] International Electrotechnical Commission (IEC). Medical electrical equipment - Part 2-33: Particular requirements for the basic safety and essential performance of magnetic resonance equipment for medical diagnosis, 2010. IEC 60601-2-33 Ed. 3.0.

[138] A. Ahlbom, U. Bergqvist, J.H. Bernhardt, J.P. Cesarini, M. Grandolfo, M. Hietanen, A.F. McKinlay, M.H. Repacholi, D.H. Sliney, J.A.J. Stolwijk, M.L. Swicord, L.D. Szabo, M. Taki, T.S. Tenforde, H.P. Jammet, and R. Matthes. Guidelines for limiting exposure to time-varying electric, magnetic, and electromagnetic fields (up to 300 GHz). *Health physics*, 74(4):494–521, 1998.

[139] National Institutes of Health, U.S. National Library of Medicine. A complete, anatomically detailed, three-dimensional representations of the normal male and female human bodies, 2015. [Online]. Available: https://www.nlm.nih.gov/research/visible/visible_human.html.

[140] A. Christ, W. Kainz, E.G. Hahn, K. Honegger, M. Zefferer, E. Neufeld, W. Rascher, R. Janka, W. Bautz, J. Chen, B. Kiefer, P. Schmitt, H.-P. Hollenbach, J. Shen, M. Oberle, D. Szczerba, A. Kam, J.W. Guag, and N. Kuster. The virtual family - development of surface-based anatomical models of two adults and two children for dosimetric simulations. *Physics in Medicine and Biology*, 55(2):N23–N38, 2010.

[141] M.-C. Gosselin, E. Neufeld, H. Moser, E. Huber, S. Farcito, L. Gerber, M. Jedensjo, I. Hilber, F.D. Gennaro, B. Lloyd, E. Cherubini, D. Szczerba, W. Kainz, and N. Kuster. Development of a new generation of high-resolution anatomical models for medical device evaluation: The Virtual Population 3.0. *Physics in Medicine and Biology*, 59(18):5287–5303, 2014.

[142] G. Tiberi, N. Fontana, M. Costagli, R. Stara, L. Biagi, M.R. Symms, A. Monorchio, A. Retico, M. Cosottini, and M. Tosetti. Investigation of maximum local specific absorption rate in 7 T magnetic resonance with respect to load size by use of electromagnetic simulations. *Bioelectromagnetics*, 36(5):358–366, 2015.

[143] H. Homann, P. Börnert, H. Eggers, K. Nehrke, O. Dössel, and I. Graesslin. Toward individualized SAR models and in vivo validation. *Magnetic Resonance in Medicine*, 66(6):1767–1776, 2011.

[144] G. Tiberi, M. Costagli, L. Biagi, A.D. Ciantis, N. Fontana, R. Stara, M.R. Symms, M. Cosottini, R. Guerrini, and M. Tosetti. SAR prediction in adults and children by combining measured B1+ maps and simulations at 7.0 tesla. *Journal of Magnetic Resonance Imaging*, 44(4):1048–1055, 2016.

[145] T. Voigt, H. Homann, U. Katscher, and O. Doessel. Patient-individual local SAR determination: In vivo measurements and numerical validation. *Magnetic Resonance in Medicine*, 68(4):1117–1126, 2012.

[146] X. Zhang, P.-F. Van De Moortele, J. Liu, S. Schmitter, and B. He. Quantitative prediction of radio frequency induced local heating derived from measured magnetic field maps in magnetic resonance imaging: A phantom validation at 7 T. *Applied Physics Letters*, 105(24), 2014.

[147] U. Katscher and K. Djamshidi. Improving B1-based SAR determination via iterative determination of missing field components. In *Proceedings of the 21st Annual Meeting ISMRM*, page 4410, Salt Lake City (US-UT), 2013.

[148] M. Krzywinski and N. Altman. Visualizing samples with box plots. *Nature Methods*, 11(2):119–120, 2014.

[149] F. Plastria and E. Weiszfeld. On the point for which the sum of the distances to n given points is minimum. *Annals of Operations Research*, 167(1):7–41, 2009.

[150] P.-A. Barrière, J. Idier, Y. Goussard, and J.-J. Laurin. On algorithms based on joint estimation of currents and contrast in microwave tomography, 2009. [Online]. Available: https://arxiv.org/abs/0901.4723v1.

[151] E. Polak and G. Ribière. Note sur la convergence de méthodes de directions conjuguées. *Revue française d'informatique et de recherche opérationnelle. Série rouge*, 3(16):35–43, 1969.

[152] A. Zakaria, C. Gilmore, and J. LoVetri. Finite-element contrast source inversion method for microwave imaging. *Inverse Problems*, 26(11), 2010. Art. no. 115010.

[153] M. Li, O. Semerci, and A. Abubakar. A contrast source inversion method in the wavelet domain. *Inverse Problems*, 29(2), 2013. Art. no. 025015.

[154] A.N. Kolmogorov and S.V. Fomin. *Elements of the theory of functions and functional analysis*. Dover publications, Mineola (US-NY), 1999.

[155] D. Vandevoorde and N.M. Josuttis. *C++ templates: the complete guide*. Addison Wesley, Boston (US-MA), 2003.

[156] R.D. Ryne. On FFT-based convolutions and correlations, with application to solving Poisson's equation in an open rectangular pipe, 2011. [Online]. Available: https://arxiv.org/abs/1111.4971v1.

[157] S. Mirhadi, M. Soleimani, and A. Abdolali. An FFT-based approach in acceleration of discrete Green's function method for antenna analysis. *Progress In Electromagnetics Research M*, 29:17–28, 2013.

[158] M. Frigo and S.G. Johnson. The design and implementation of FFTW3. *Proceedings of the IEEE*, 93(2):216–231, 2005.

[159] G. Guennebaud et al. Eigen v3, accessed on 2017, 2010. [Online]. Available: http://eigen.tuxfamily.org/.

[160] A. Zakaria and J. LoVetri. Application of multiplicative regularization to the finite-element contrast source inversion method. *IEEE Transactions on Antennas and Propagation*, 59(9):3495–3498, 2011. Art. no. 5948360.

[161] J.R. Shewchuk. Triangle: Engineering a 2D quality mesh generator and Delaunay triangulator. *Lecture Notes in Computer Science (including subseries Lecture Notes in Artificial Intelligence and Lecture Notes in Bioinformatics)*, 1148:203–222, 1996.

[162] J.R. Shewchuk. Delaunay refinement algorithms for triangular mesh generation. *Computational Geometry: Theory and Applications*, 22(1-3):21–74, 2002.

[163] A. Abubakar and P.M. van den Berg. Iterative forward and inverse algorithms based on domain integral equations for three-dimensional electric and magnetic objects. *Journal of Computational Physics*, 195(1):236–262, 2004.

[164] T. Isernia, L. Crocco, and M. D'Urso. New tools and series for forward and inverse scattering problems in lossy media. *IEEE Geoscience and Remote Sensing Letters*, 1(4):327–331, 2004.

[165] P.-A. Barrière, J. Idier, J.-J. Laurin, and Y. Goussard. Contrast source inversion method applied to relatively high contrast objects. *Inverse Problems*, 27(7), 2011. Art. no. 075012.

[166] P.M. Van Den Berg, A.L. Van Broekhoven, and A. Abubakar. Extended contrast source inversion. *Inverse Problems*, 15(5):1325–1344, 1999.

[167] P.M. Van Den Berg, A. Abubakar, and J.T. Fokkema. Multiplicative regularization for contrast profile inversion. *Radio Science*, 38(2):VIC23/1–VIC23/10, 2003.

[168] Joint committee for guides in metrology. JGCM 101:2008. Evaluation of measurement data – Supplement 1 to the "Guide to the expression of uncertainty in measurement" – Propagation of distributions using a Monte Carlo method, 2008. [Online]. Available: https://www.bipm.org/en/publications/guides/gum.html.

[169] Y. Gossuin, A. Hocq, P. Gillis, and V. Quoc Lam. Physics of magnetic resonance imaging: From spin to pixel. *Journal of Physics D: Applied Physics*, 43(21), 2010. Art. no. 213001.

[170] R.W. Brown, Y.-C.N. Cheng, E.M. Haacke, M.R. Thompson, and R. Venkatesan. *Magnetic Resonance Imaging: Physical Principles and Sequence Design: Second Edition*. John Wiley & Sons, Hoboken (US-NJ), second edition, 2014.

[171] G. Wang, H. Xie, S. Hou, W. Chen, and X. Yang. Development of high-field permanent magnetic circuits for NMRI/MRI and imaging on mice. *BioMed Research International*, 2016, 2016. Art. no. 8659298.

[172] F. Bloch. Nuclear induction. *Physical Review*, 70(7-8):460–474, 1946.

[173] D.I. Hoult. The principle of reciprocity in signal strength calculations - a mathematical guide. *Concepts in Magnetic Resonance*, 12(4):173–187, 2000.

[174] D.I. Hoult and R.E. Richards. The signal-to-noise ratio of the nuclear magnetic resonance experiment. *Journal of Magnetic Resonance (1969)*, 24(1):71–85, 1976.

[175] D.I. Hoult. The principle of reciprocity. *Journal of Magnetic Resonance*, 213(2):344–346, 2011.

[176] T.S. Ibrahim. Analytical approach to the mr signal. *Magnetic Resonance in Medicine*, 54(3):677–682, 2005.

[177] H.C. Torrey. Bloch equations with diffusion terms. *Physical Review*, 104(3):563–565, 1956.

[178] H. Brezis. *Analyse fonctionnelle. Théorie et applications.* Masson, Paris (FR), 1987.